
# Fano resonances in metal /dielectric composites and growth mechanism and ferromagnetism in ZnO nanostructures

By

Leta Tesfaye

A THESIS SUBMITTED IN PARTIAL FULFILLMENT OF THE
REQUIREMENTS FOR THE DEGREE OF
DOCTOR OF PHILOSOPHY
AT
ADDIS ABBABA UNIVERSITY
ADDIS ABABA, ETHIOPIA
JUNE 6, 2017

ADDIS ABBABA UNIVERSITY
DEPARTMENT OF
PHYSICS

The undersigned hereby certify that they have read and recommend to the College of Graduate Studies for acceptance a thesis entitled "**Fano resonances in metal /dielectric composites and growth mechanism and ferromagnetism in ZnO nanostructures**" by **Leta Tesfaye** in partial fulfillment of the requirements for the degree of **Doctor of Philosophy**.

Dated: June 6, 2017

External Examiner: _____
Dr. Genene Tessema

Research Supervisors: _____
Dr. Teshome Senbeta and Dr. Belayneh Mesfin

Examing Committee: _____
Dr. Genene Tessema

_____
Dr. Cherinet Amente, Dr. Lemi Demeyu

ADDIS ABBABA UNIVERSITY

Date: **June 6, 2017**

Author: **Leta Tesfaye**

Title: **Fano resonances in metal /dielectric composites and growth mechanism and ferromagnetism in ZnO nanostructures**

Department: **Physics**

Degree: **Ph.D.** Convocation: **June** Year: **2017**

*To my family*

# Table of Contents

# List of Figures

# Abstract

In this dissertation, we studied on the origin and physical mechanisms leading to Fano resonances and scattering of light in metal /dielectric composites. The properties of composite materials can be tuned by dielectric permittivity of host matrix, volume fraction, geometry of the inclusion and distribution type. The theoretical model consists of non-magnetic spherical and cylindrical nanoinclusions which are embedded in non-absorbing host medium illuminated by plane waves having uniform electric fields. The method employed treats the arrays of particles within the framework of the conventional Rayleigh approximation. The electric potential distribution of the composites having dielectric core, metal shell and host matrices are systematically calculated. As such metal/dielectric nanocomposites with careful arrangement can also support Fano like resonances, the underlying mechanisms including their origin are discussed. We find that Fano-like resonances can occur at the same input volume fraction of the metal coated ($p$) provided the dielectric function of active host medium ($\varepsilon_h''$) has negative values. Such Fano-like resonance are induced by interaction between dipolar modes of the inner core, and multipolar plasmon modes of the coated shell. This provides potential application in high performance surface-enhanced spectroscopy, electromagnetic induced transparency, biosensing, plasmon line shaping, lasing and nonlinear switching. In addition, the experimental section of the study in the thesis presents the growth mechanism of ZnO with different morphologies. The effect of dopant concentration on the optical and magnetic properties has been studied. The role of precursor, reaction temperature and the origin of ferromagnetism in Al doped ZnO has been reported. ZnO nanostructures prepared using sol-gel and chemical bath deposition are analyzed using different techniques. The final product was analyzed using such techniques as scanning electron microscopy (SEM), photoluminescence (PL) spectroscopy (steady and temperature dependent), Ultra-violet visible (UV-Vis) spectroscopy, Fourier transform infrared spectroscopy (FTIR), Electron paramagnetic resonance (EPR), X-ray diffraction (XRD) and Raman spectroscopy.

# Acknowledgements

I express my profound sense of reverence to my late Professor Vadim Mal'nev, his continuous guidance from the early studies (MSc study) to my PhD courses was unforgettable. His guidance, support, motivation and untiring help during the course of my PhD until he was departed was amazing. I have been amazingly fortunate to have a professor who gave me a full freedom to explore on my own way and at the same time the guidance to recover when my steps faltered. I hope that one day I would become as good an advisor to my students as Prof has been to me. Let your soul rest in peace. My co-supervisors, Dr. Teshome Senbeta and Dr. Belayneh Mesfin, are always been there to listen, guide and mentor on my work and give some brotherly advice. I am deeply grateful to them for the crucial discussions that helped me sort out the chemistry aspect of my work. I am also thankful to Dr. Tesgera and Dr. Lemi for their support and advice during my PhD courses and seminars.

It is my pleasure to acknowledge all my current and previous colleagues at AAU Physics department, secretary Ms. Tsilat who handle non-scientific related jobs such as finance and documentation. I will always be grateful to them for helping me to develop the scientific approach and attitude. Dr. Zelalem Nigussa from NMMU, I am very thankful for your encouragement, for numerous discussions on related topics that helped me improve my knowledge in the area and support during the entire course of my studies you are the man in need and indeed. Prof. F.B. Dejene, Prof J.R. Botha, Prof. K. Allam, Dr. K. T. Roro from South Africa are also owed my thanks and acknowledgments.

It would not have been possible to carry out this research without the financial support from Graduate program AAU and Wolkite University for the study leave.

Finally, and most importantly, I would like to thank my wife Lelise. Your support, encouragement, patience and unwavering love were undeniably and I owe you love and respect than I can say with this little space. I would like to thank my lovely daughter Milki for that wonderful smile and playful time that you were always able to create. I thank my parents, brothers and sisters, for their faith in me and allowing me to be as ambitious as I wanted. It was under their watchful eye that I gained so much drive and an ability to tackle challenges head on.

# Chapter 1

# Introduction

## 1.1 Light scattering theory

Scattering of light from bulk materials are caused by the deflection of light rays in random directions due to the presence of inhomogeneities which result in the change in the refractive index of the material. When the frequency of the incoming EM wave is equal to the natural frequency of free vibration of the particles in the material, one observes resonant absorption. However, scattering in matter, occurs at frequencies that doesn't correspond to the natural frequency of the particles. As the EM fields oscillate in the wave, the electrons in the material oscillate at the same frequency and thus radiate their own EM wave (emission) that is at the same frequency, but usually with a phase delay. The earlier work on light scattering by small particles is mainly from Lorenz, Thomson and Clebsh [1]. The exact solution has been obtained by Clebsh in 1861 in his paper "Concerning reflection on a spherical surface" published in 1863, a year before Maxwell's work about electromagnetic theory of light. The breakthrough in understanding light scattering by spherical structures came from the work of Mie in 1908 [2]. He obtained a general rigorous solution, on basis of the electromagnetic theory, for the optical scattering by a homogeneous sphere. The phenomenon of scattering processes are classified into three broad categories, on the basis of the wavelength ($\lambda$) of light and the size (d) of the particles. These are Rayleigh Scattering ($d \ll \lambda$), Mie Scattering $d \gg \lambda$ and resonance domain or Critical phenomena ($\lambda \sim d$). Rayleigh scattering is the elastic scattering of light or other electromagnetic

radiation, by particles much smaller than the wavelength of the light ($d \ll \lambda$) [3]. It can occur when light travels in transparent solids and liquids, but is most prominently seen in gases. For the case of particles with diameters much larger than the wavelength of light, the Mie scattering approximation is used, the limiting case of which is geometric optics. In the case of light scattering by small plasmonic particles, the dipole Rayleigh scattering plays a role of a broad spectral radiation and the surface plasmon resonance (e.g., quadrupole or higher-order resonance) plays a role of a narrow spectral line interacting with the broad radiation. In the framework of the well-known Mie theory [4, 5], such a Fano resonance manifests itself in the differential scattering efficiency cross-sections. The traditional Lorenz-Mie theory describes the scattering by a spherical homogeneous dielectric particles illuminated by an incident plane wave [6, 7]. The present thesis considers only the case of Fano resonance which are induced because of dipole interaction formed in the inclusions ignoring the higher order resonances. In the resonance domain, sizes of the particles (the structural variations) inside the material are comparable to the wavelength of light. Elastic light scattering in the resonance domain is still an active area of interest. In this case, the wavelength-sized particles scatter light very efficiently [8]. The field of metal-nanoparticle optics has come a long way from the spectral tuning of dipolar resonances via simple changes in particle shape. The exploitation of so-called dark modes via Fano resonances enables us to create nanostructures exhibiting a sharp spectral response and minimum scattering, while the novel tool of transformation optics provides a paradigm for the design of new classes of nanoscale optical cavities suitable for broadband light harvesting [9, 10].

### 1.1.1 Resonances and its effects

Metal nanoparticles with sizes smaller than the wavelength of visible light show strong resonances for light scattering and absorption, due to the excitation of localized surface plasmons [11]. At resonance, light resonantly drives collective

oscillation of the conduction electrons of the metal nanoparticle, which therefore acts as a radiating dipole. Its resonance frequency is strongly dependent on particle shape and dielectric environment, which enables tuning of its color throughout the visible and into the near-infrared regime of the spectrum, while keeping particle size well below 100 nm. The most prominent application of this effect has been all around us during history, in the form of colored glass, incorporating metal nanoparticle dopants. More modern applications, increasingly at a single-nanoparticle level, lie in the tagging of biomolecules, enhancement of light emission from nanoscale photon sources, and biomolecular sensing. All of these exploit the fact that at their dipolar resonance frequencies, metal nanoparticles enable nano-concentration of light below the diffraction limit around the particle surface, and feature resonantly enhanced absorption and scattering cross-sections. Controlled nanofabrication, and particularly electron-beam lithography, now enables us to create metallic nanostructures consisting of multiple metallic elements with controlled relative placements down to distances on the order of 10 nm. This provides a simple yet compelling way to not only tune the resonance frequencies of the system, but also the interaction strength with radiation, via exploitation of near-field coupling between neighboring units.

### 1.1.2 Bright and Dark Modes: Mechanism Underlying Fano Resonances

The physical mechanism underlying Fano resonances is the interference between broad continuum-like modes and narrow localized modes. While the original work on Fano interference concerned the quantum mechanical description of autoionizing electronic states of atoms, it has since then been demonstrated that Fano interference is a quite common phenomenon occurring in a wide range of systems. More elaborate models based on coupled mode theory also provide a general and physically intuitive approach for describing Fano resonances. The simplest case of two interacting dipoles are interesting to describe bright and dark modes. Depending on whether their dipole moments are aligned parallel or anti-parallel with

each other, the respective coupled modes will either show a stronger or weaker interaction with far-field radiation. The normal modes of a dimer system consists of a spectrally broad bright or superradiant mode, and of a spectrally narrow dark or subradiant mode. With the concept of bright and dark modes, the balance between absorption and scattering of plasmonic nanocavities can be controlled. In essence, metal nanoparticles can be understood as classical harmonic-oscillator systems at the nanoscale, and many features of collective resonances in simple geometrical arrangements can be conceptually modeled as masses on springs. Interactions between localized plasmons in more complex geometries can be elegantly understood within the concept of plasmon hybridization.

Fano resonances arises in appropriately designed systems where a spectrally narrow resonance of a dark mode overlaps with a spectrally broad bright mode: in analogy to quantum systems of a localized state interacting with a continuum. At these resonances, linear destructive interference between two excitation pathways of the bright mode directly, or via coupling with the dark state lead to quenching of scattering, and hence an increase in transmission in a spectrally sharp window. These effects were experimentally demonstrated in a number of plasmonic nanosystems at the single-particle level, such as dolmen-type structures or disk/ring cavities [5]. The optical properties of plasmonic nanoparticles result from the interaction between multiple plasmon modes of the same nanostructure such as nanodimers. In the core-shell geometry of a nanoshell, for example, plasmon resonance frequencies are determined by the interaction between the two primitive plasmons supported by the structure, namely, the sphere and cavity plasmon modes [5]. Most spectacularly, a stacked arrangement of three metallic bars has been shown to quench scattering completely due to a Fano effect, leading to a nanostructure which only absorbs light, but does not scatter. Fano resonances have now been shown in an increasing number of plasmonic nanostructures, and also in metamaterials, promising exploitations in highly sensitive biological sensors, dispersive elements for slow-light metamaterials waveguides, and nanoscale

light sources. The origin of Fano resonances in such systems are suggested by different groups, for instance symmetry breaking of nanostructures which introduce a coupling between subradiant and super-radiant modes and enable Fano interference. On the other hand, Fano interference in plasmonic structures can result from the intrinsic interference of absorption channels such as excitation of conduction electrons and interband transitions. However, in this thesis we will focus on Fano resonances observation in composites having metal/dielectric core-shell caused by interference between two modes.

### 1.1.3 Light scattering by spherical nanoparticles

Scattering of electromagnetic waves are widely used to gain information about the microstructures of systems. For example, x-ray diffraction and scattering are widely used as a means to gain statistical information about the arrangement of crystal lattice and particle size in a given samples. In addition, visible light scattering is an important experimental tool for determining the distribution of particle sizes. Propagating light also changes its course due to scattering by spherical particles [11, 12, 13, 14]. The directionality of the outgoing flow of energy is determined by the direction of the incident light, the material properties, and the length scales involved in the interaction between the light and the scattering particle. Conventional approaches to control light at the nanoscale is based on the engineering the electric responses of nanostructures, due to the fact that most materials have only dominant electric responses, especially in the optical regime. The most widely employed response is the electric dipole (ED) resonance, the scattering pattern of which exhibits two typical features: (1) light is scattered equally to the backward and forward directions, and (2) orientation of the excited ED is decided by the polarization of the incident wave, resulting in asymmetric azimuthal scattering patterns. For various applications based on the particle scattering such as nanoantennas, sensing, and photovoltaic devices, the scattering

patterns that are significantly different from that of a typical ED are usually required. One outstanding example is the requirement of the scattering pattern with suppressed backward scattering (reflection) and enhance forward scattering [15]. The existing techniques usually rely on external additional coupled items, such as an extra reflector, an extended substrate, Fabry-Perot resonator like structures, and/or other complicatedly engineered nanostructures, which could significantly hinder possible practical applications. As most materials have only dominant electric responses, conventional approaches to shape effectively the scattering patterns are mostly based on the engineering of the electric responses of various structures. For particle size less than the wavelength of light the phase is constant. When homogeneous field of incident light shone on the particle, it produces polarization that results in scattering.

## 1.2 Fabrication and Ferromagnetism of ZnO Nanostructures

### 1.2.1 Overview of ZnO Nanostructures

The interest in wide band gap semiconductors has been significantly increasing because of its excellent properties as a semiconductor material. ZnO is a wide-band gap (3.37 eV at 300 K ) and large exciton binding energy (60 meV) semiconductor currently of interest for possible electronic and optical applications. It crystallizes preferentially in the hexagonal wurtzite type crystal structure. In addition, ZnO doped with transition metals shows great promise for spintronic applications. It has also been suggested that ZnO exhibits sensitivity to various gas species, namely ethanol ($C_2H_5OH$), acetylene ($C_2H_2$), and carbon monoxide ($CO$), which makes it suitable for sensing applications. Moreover, its piezoelectric property (originating from its non-centrosymmetric structure) makes it suitable for electromechanical sensor or actuator applications. Also, ZnO is biocompatible which makes it suitable for biomedical applications. Moreover, ZnO is a chemically stable and environmentally friendly material as the result, there is considerable

interest in studying ZnO in the form of powders, single crystals, thin films, or nanostructures.

Easiness of growing it in the nanostructure form by many different methods make ZnO suitable for wide range of applications. The knowledge of the properties of intrinsic defects, i.e., vacancies and interstitials, is important because they provide various diffusion mechanisms involved in device production and their degradation. Optical, structural, electrical, and magnetic properties of ZnO strongly depend on the impurities and defects in this material. On the other hand the role of precursor, reaction temperature, PH of concentration and growth environment has also been great impact on the properties of ZnO nanostructures. There are several perfect reviews devoted to general properties of ZnO by Ozgur et al. [16] and Klingshirn et al. [17], on the methods of crystal growth, properties of intrinsic defects, donor and acceptor impurities, transition metal (TM) impurities, and magnetic properties. Obtaining controllable, reliable, reproducible and high conductive p-type doping in ZnO has been very difficult task [18], due to the low formation energies for intrinsic donor defects such as zinc interstitials ($Zn_i$) and oxygen vacancies ($V_O$) which can compensate the accepters. The current research on ZnO includes growth technology much simpler and available at low cost likely achieved at low temperature. There are various growth method of ZnO among which are, chemical bath deposition, sol-gel, chemical-vapor transport, vapor-phase growth, hydrothermal growth. ZnO nanostructure morphologies such as nanorods, flower-like and nanobelts are produced by the sol-gel and chemical bath methods are the subject of much interest, in view of the simplicity, low cost, reliability, repeatability and relatively mild conditions of synthesis, which are such as to enable the surface modification of zinc oxide with selected organic compounds [19]. In addition, room temperature ferromagnetic properties of ZnO when doped with transition metals (Co, Mn, Fe, etc) and non-magnetic ions or materials also attracts considerable attention of scientific community for development of spintronics technology. In this study, we have demonstrated the effect of

precursor and reaction temperature on the morphologies of ZnO nanostructures, in particular ZnO nanorods, flower-like and core-shell structures.

### 1.2.2 Ferromagnetism in ZnO nanostructures

Transition-metal (TM) impurities have been found to alter optical, magnetic, and other physical properties of the host semiconductor significantly, leading to intense interest in diluted magnetic semiconductors (DMS). Oxide based on DMSs such as ZnO, $TiO_2$ and $SnO_2$ plays significant role in spintronics applications for novel memory and optical devices [17]. The interest in simultaneous control of both charge and spin has driven the study of TM ion doping in semiconductor materials to realize room-temperature ferromagnetism (RTFM). Recent theoretical and experimental studies in DMS materials revealed RTFM for wide band gap materials such as GaN and ZnO for TM doping. These metals have partially filled $3d$ states and contain unpaired electrons, which are thus responsible for the magnetic behavior in DMSs. Basically, when a TM ion substitutes for the cation of a semiconductor host lattice, the resultant electronic structure is strongly influenced by the hybridization between the $3d$ orbitals of the magnetic ion and the $p$ orbitals of neighboring anions. This hybridization can lead to magnetic interaction between the localized $3d$ electrons and the carriers in the valence band of the host lattice [18, 19]. In DMS materials, magnetic transition ions substitute a small percentage of cation sites of the host semiconductor and are coupled with free carriers to yield ferromagnetism via indirect interaction.

Under an external magnetic field, the electron's magnetic moment aligns itself either parallel or antiparallel to the field. The splitting of the energy levels between the lower and the upper state is directly proportional to the magnetic field strength. An unpaired electron can move between the two energy levels by either absorbing or emitting a photon of energy $h\nu$ once the resonance condition is obeyed. Experimentally, a great majority of electro paramagnetic resonance measurements are conducted with microwaves at a fixed frequency. By increasing

an external magnetic field, energy separation between the two states is widened until it matches the energy of the microwaves. ZnO based dilute magnetic semiconductors have been extensively studied due to the predication of ferromagnetism above room temperature. Subsequently, ZnO $d^0$ ferromagnetism has been found to exist in undoped ZnO or in ZnO doped with non-magnetic ions, such as H, Li, C, and N. Based on both theoretical and experimental considerations, many groups have proposed that the ferromagnetism in nominally undoped ZnO arises from intrinsic defects such as oxygen vacancy, oxygen interstitial, zinc vacancy, zinc interstitial and H interstitial. There are also another proposed approaches to understand the origin of ferromagnetism in such oxides, which are based on the general mean-field theory, implicitly assumes that the dilute magnetic semiconductor is a more or less random alloy, e.g., Zn, TM O, in which TM substitutes for one of the lattice constituents. The ferromagnetism occurs through interactions between the local moments of the TM atoms, which are mediated by free carriers in the material. The spin spin coupling is also assumed to be a long-range interaction, allowing use of a mean-field approximation. In addition, the strain and charge transfer also suggested as the origin of ferromagnetism in ZnO related materials. However, until now, the mechanism involved in ferromagnetism is complex, the origin is debatable and the reproducibility of ferromagnetic behavior is still a challenging problem. In this thesis, we have made considerable effort to understand the mechanism and origin of ferromagnetism in undoped ZnO and Al doped ZnO nanostructures.

## 1.3 Motivation and Outline

Nanotechnology enables us the fabrication of different devices like sensor, optoelectronic probe, chips, fibres etc. The devices create new opportunities and alternative use in telecommunication, medicines, research areas, in computer technologies and more. The effectiveness of these devises are basically based on basic principles of physical phenomena such as transport processes of wave excitations

and resonance effects. The scattering waves due to the interaction of light and electrons result in different phase coherence. If the scattered waves travel short distances, they make phase coherent process that are important in describing the resonance phenomena. Most of the scattering of waves involves propagation that differ in paths. The difference in paths result in interference phenomena that may be constructive or destructive. The constructive interference corresponds to resonant enhancement and the destructive interference to resonant suppression of the transmission. The current experimental and theoretical research works show this kind of interference at different physical settings.

This thesis contains two parts: Theoretical and experimental. The theoretical part demonstrates the concept of Fano resonance in composites having metal/dielectric core-shell nanoinclusions. It is well known that Fano resonance is characterized by its asymmetric line profile. The asymmetry originates from a close coexistence of resonant transmission and resonant reflection, and can be reduced to the interaction of a discrete (localized) state with a continuum of propagation modes.

The first part (theoretical part) of the thesis demonstrates the origin and the appearance of Fano like resonances in the composites. Moreover, the origin of the resonance in metal/dielectric composites has been discussed from point of plasmon hybridization model with the introduction of active host matrix.

The second part (experimental part) of the work describes about the synthesis of ZnO nanoparticles with different morphologies which includes; nanorods, core-shell and flower-like structures. The role of precursor and reaction temperature on the optical and morphologies of ZnO nanostructures are also discussed. In addition, the ferromagnetic properties undoped ZnO and Al doped ZnO nanostructures are studied in detail.

The thesis is organized as follows:

- Chapter 2: In this Chapter we present electromagnetic wave interactions with metal/dielectric composites and the optical response. We will use

two different models for describing optical properties of metals: the Lorentz model and the Drude model. Both models approximately describe the optical properties of metallic structures and the plasmonic properties that arise when the structures have dimensions of nanometers. The Chapter will conclude with a brief description of methods to study scattering of light by existing theories.

- Chapter 3: This Chapter includes the discussion of the Fano resonances and it's manifestation in different geometries and its origin. In the first section of the Chapter we will try to compare the Lorentzian resonance which corresponds to a fundamental symmetric line-shape with Fano resonance that is characterized by an asymmetric line-shape, with a Fano dip and a Fano peak. The Fano resonance can be viewed as a hybrid state coming from the interference of a discrete state with the continuum or a broad state. Moreover, Classical and quantum analogy of Fano resonance are also discussed. Models and theories applicable to the present study will be presented in detail under this section.

- Chapter 4: The details about the experimental part of the study are described under this chapter. The techniques used to synthesize the samples, specifically sol-gel and chemical bath deposition of ZnO nanoparticles are elaborated. Finally, the methods used for characterizing the samples and the equipments used during measurements are explained.

- Chapter 5: In this Chapter we investigate light scattering by core-shell consisting of metal/dielectric composites considering spherical and cylindrical nanoinclusions, within the framework of the conventional Rayleigh approximation. By writing the electric potential distribution of the dielectric core, metal shell and host matrices in the core-shell composites, we have derived an analytical expression for the polarization of individual metal shell spherical and cylindrical inclusions. Moreover, we demonstrated that modeling

the dielectric function of the dispersive core for both frequency dependent (the scattering cross-section) and frequency independent dielectric function of the core, one can tune Fano regions in the core-shell(metal/dielectric) composites.

- Chapter 6: Experiment on electron paramagnetic resonance (EPR) signals of Al-doped ZnO with different concentration of Al and its ferromagnetic properties are presented under this Chapter. The sample of Al-doped ZnO (AZO) nanopowders are prepared by facile sol-gel method. The analysis of electron paramagnetic resonance were carried out in details. In addition, the chapter is devoted to the discussion of ZnO nanostructures with various geometries (flower-like and nanorods(core-shell) structures) which were produced by the chemical bath deposition method using zinc acetate as precursor. The morphology of ZnO in both structures are more controlled by the precursor concentration and reaction temperature. ZnO nanorods were grown on pre-coated Si substrate from an aqueous solution of zinc nitrate hexahydrate followed by sulphidation process to form ZnO/ZnS nanorod core-shell. Temperature dependent photoluminescence properties of ZnO nanorods have been investigated and underlying mechanism are discussed under this section.

- Chapter 7: Conclusions and future work of the study are summarized under this Chapter.

# Chapter 2

# Modeling the optical response of metal/dielectric nanocomposites

## 2.1 Introduction

Interaction of light with nanocomposites show new optical property with out changing the properties of the materials. The linear and nonlinear optical response of metal nanoparticles is specified by oscillations of the surface electrons in the Coulomb potential formed by the positively charged ionic core. This type of excitation is called the Surface Plasmon (SP) [20]. In 1908 Mie proposed a solution of Maxwells equations for spherical particles interacting with plane electromagnetic waves, which explains the origin of surface plasmon resonance (SPR) in the extinction spectra and colouration of metal colloids [21]. It is almost more than a century that optical properties of metals studied. These studies showed that metal dielectric composites exhibits Fano-like resonance when illuminated by plane waves. Since the optical properties of metal nanoparticles are governed by SPR, they are strongly dependent on the nanoparticles size, shape, concentration and spatial distribution as well as on the properties of the surrounding matrix (host matrix). Control over these parameters enables such metal-dielectric nanocomposites to become promising media for development of novel non-linear materials, nanodevices and optical elements [22, 23, 24].

An electromagnetic wave propagating through different media is affected by interactions with each medium as it traverses across the boundary between one

medium and another. The two main interactions between incident light and a discrete particle are absorption and scattering. Scattering can be inelastic, where the wavelength of the scattered radiation is different from the incident wavelength, or elastic, where the scattered radiation has the same wavelength as the incident light. Examples of elastic scattering are Rayleigh scattering from small, dielectric (nonabsorbing) spherical particles and Mie scattering from spherical particles with no limitations on size or dielectric properties. The discussion on electromagnetic waves has been limited to the propagation of waves and interactions with simple structures composed of arbitrary media. In the following section, two different models for describing metals will be discussed: the Lorentz model and the Drude model. Both models approximately describe the optical properties of metallic structures and the plasmonic properties that arise when the structures have dimensions on the order of nanometers. Specifically, the manifestation of surface plasmons in bulk metals, discrete particles, and metal/dielectric will be discussed. The Chapter will conclude with a brief description of different models and theories of light scattering and absorption from metal dielectric composite arrays.

## 2.2 Models describing metals and dielectrics

### 2.2.1 Lorentz Model

The optical properties of metals due to the motion of conduction electrons through a fixed, ionic background can be fully described with the help of plasma model. The Plasma model was developed by H. A. Lorentz as a classical approach to describe optical properties of materials by assuming that electrons and ions of a medium are simple harmonic oscillators and neglecting material properties such as the lattice potential and electron-electron interactions. It is more convenient to use the oscillator model to describe optical excitations. The oscillation response to an applied local electric field, $E_{local}$, for an electron with an effective mass, m, and a charge, e, is given by [23]

$$m\frac{d^2x}{dt^2} + m\gamma\frac{dx}{dt} + Kx = eE_{loc}, \tag{2.2.1}$$

where $x$ is the distance displaced from equilibrium, $Kx$ is the restoring force for an electron with a spring constant, K. The oscillation of electrons is damped as a result of collisions, which adds a damping term to the equation, $m\gamma$, where the collision frequency, $\gamma = \frac{1}{\tau}$, and $\tau$ is the relaxation time for a free electron plasma which at room temperature is typically on the order of $10^{-14}$s making $\tau = 100THz$. Since the electric field has a harmonic time dependence,

$$E(t) = E_0 e^{-i\omega t}, \tag{2.2.2}$$

with a driving frequency $\omega$, and time, t, the solution to the equation for an electron becomes

$$x(t) = x_0 e^{-i\omega t}. \tag{2.2.3}$$

The phase shifts between the driving force of the electric field and the electron response is contained in the complex amplitude, $x_0$. The oscillatory solution to Eq. 2.2.1 becomes:

$$x(t) = E(t)\frac{e}{m(\omega_0^2 - \omega^2 - i\gamma\omega)}, \tag{2.2.4}$$

with the oscillator natural frequency $(\omega_0)$, $\omega_0^2 = \frac{K}{m}$. A schematic of a Lorentz harmonic is shown in Fig. 2.1.

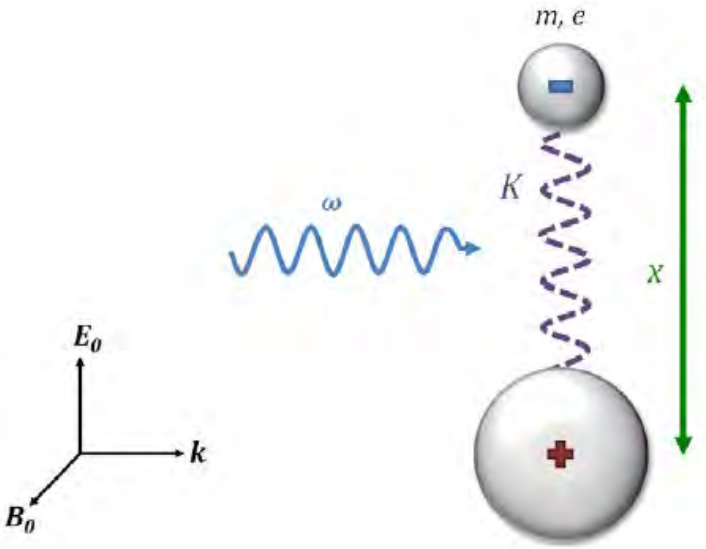


**Figure 2.1:** Lorentz harmonic oscillator.

In most systems, there is a certain degree of collisions that occur which means $\gamma \neq 0$ and the phase of the driving field and oscillating electrons have a displacement, (D) $D = |x|e^{(i\theta)}$,

$$D = Ae^{(i\theta)}(\frac{eE}{m}), \tag{2.2.5}$$

with phase angle, $\theta$ ,

$$\theta = \tan^{-1}[\frac{\omega\gamma}{\omega_0^2 - \omega^2}], \tag{2.2.6}$$

and amplitude, A,

$$A = [\frac{1}{[(\omega_0^2 - \omega^2)^2 + \omega^2\gamma^2]^{\frac{1}{2}}}], \tag{2.2.7}$$

The consequence of the phase difference results in the maximum amplitude occurring when the frequencies $\omega_0 \cong \omega$. If $\gamma \ll \omega_0$, the height of the maximum amplitude is inversely proportional to $\gamma$ and the full width at half maximum (FWHM) is proportional to $\gamma$. Fig. 2.2 shows a plot for the amplitude and phase relation for a hypothetical oscillator. At low frequencies, the oscillator response is in phase with the driving force where $\theta \cong 0$ and $\omega \ll \omega_0$ as shown in Fig.2.2 (a). For a single oscillator, the induced dipole moment is $p = ex$. For a large number

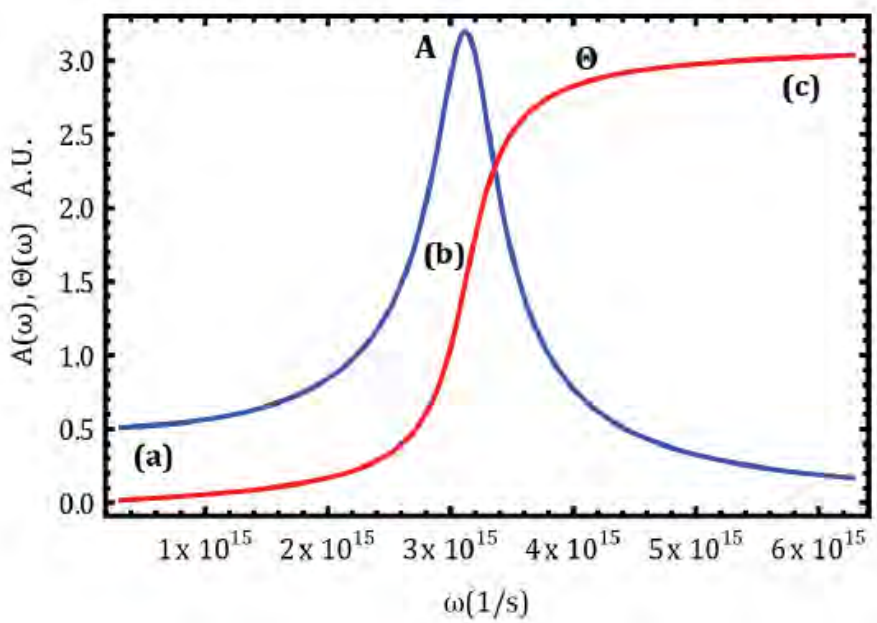


**Figure 2.2:** Hypothetical oscillator response to a driving force at (a) low frequencies, (b) resonance frequency, $\omega_0$, and (c) high frequencies [22].

of oscillators, n, the dipole moment per unit volume becomes,

$$P = -nex, \tag{2.2.8}$$

and when combined with Eq.2.2.4 becomes

$$P = \frac{\omega_p^2}{\omega_0^2 - \omega^2 - i\omega\gamma} E\varepsilon_0, \tag{2.2.9}$$

where the plasma frequency, is given by

$$\omega_p^2 = \frac{ne^2}{\varepsilon_0 m}, \tag{2.2.10}$$

The optical constants for the collection of oscillators can then be derived out, where the dielectric function for the bulk material is given by

$$\varepsilon(\omega) = 1 + \chi = 1 + \frac{\omega_p^2}{\omega_0^2 - \omega^2 - i\omega\gamma}, \tag{2.2.11}$$

which can be decomposed into the real, $\varepsilon_1$, and imaginary, $\varepsilon_2$, components of the complex dielectric function, $\varepsilon(\omega) = \varepsilon_1(\omega) + i\varepsilon_2(\omega)$ as

$$\varepsilon_1(\omega) = 1 + \chi' = 1 + \frac{\omega_p^2(\omega_0^2 - \omega^2)}{(\omega_0^2 - \omega^2)^2 + \omega^2\gamma^2}, \tag{2.2.12}$$

$$\varepsilon_2(\omega) = \chi'' = \frac{\omega_p^2\omega\gamma}{(\omega_0^2 - \omega^2)^2 + \omega^2\gamma^2}, \tag{2.2.13}$$

At the plasma frequency, $\omega_0$, the imaginary part of the dielectric constant is at a maximum as shown in Fig. 2.3 for silver

### 2.2.2 Drude Model

In metals, the conduction and valence band overlap allowing for electrons near the Fermi level to be excited to different energy and momentum states by the absorption of photons with very little energy. These intraband transitions give rise to free electrons which can be taken into account by modification of the Lorentz model. When the spring constant in Eq.2.2.1 is set to zero, it essentially clips the springs of the harmonic oscillators with K = 0 and $\omega_0 = 0$ to transform Eq.2.2.4 into

$$x(t) = -E(t)\frac{e}{m(\omega^2 + i\gamma\omega)}, \tag{2.2.14}$$

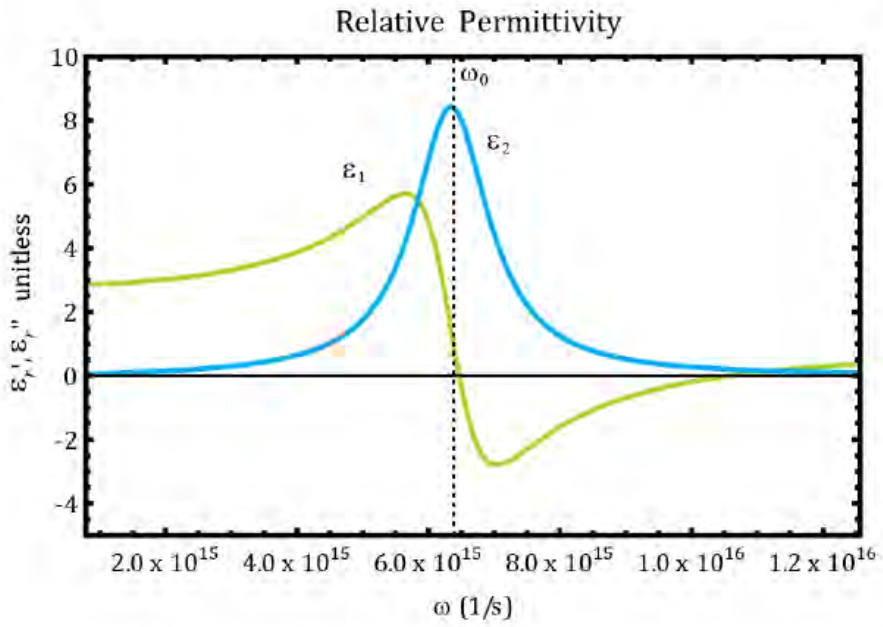


**Figure 2.3:** Frequency dependence of the real and imaginary parts of the dielectric constant of silver [22].

When the polarization in Eq.2.2.8 is combined with equation Eq.2.2.14, it becomes

$$P = -n\frac{e^2}{m(\omega^2 + i\gamma\omega)}E, \tag{2.2.15}$$

gives the relation between D and E in terms of frequency and electric permittivity as

$$D = \varepsilon_0(1 - \frac{\omega_p^2}{\omega^2 + i\gamma\omega})E, \tag{2.2.16}$$

The new dielectric function for the free electrons becomes

$$\varepsilon(\omega) = 1 - \frac{\omega_p^2}{\omega^2 + i\gamma\omega}, \tag{2.2.17}$$

which can be decomposed into the real, $\varepsilon_1$, and imaginary, $\varepsilon_2$ of the complex dielectric function as

$$\varepsilon_1(\omega) = 1 - \frac{\omega_p^2\tau^2}{1 + \omega^2\tau^2}, \tag{2.2.18}$$

$$\varepsilon_2(\omega) = \frac{\omega_p^2\tau^2}{\omega(1 + \omega^2\tau^2)}. \tag{2.2.19}$$

Eq. 2.2.17 demonstrates that the dielectric constant can become zero near the plasma frequency where the material can support collective modes of oscillating electrons in phase with each other. By tuning the geometry of the structure, the oscillation can occur at negative values of the dielectric constant.

## 2.3 Effective-medium approximation for linear media

The effective-medium approximation (EMA) is a method of treating a macroscopically inhomogeneous medium, i.e., a medium in which quantities such as the conductivity, dielectric function, or elastic modulus vary in space [24, 25, 26]. Many materials fall into this broad category. One example is a metaldielectric composite, consisting of a collection of metallic and dielectric grains arranged in some ordered or random fashion. Another example is a porous rock. If that rock is filled with salt water, then it is also a composite of an electrical insulator (the rock matrix) and an electrical conductor (the salt water). Yet a third example is a polycrystalline sample of an anisotropic material. Each grain in that polycrystal is, in essence, a different material, since it has a different conductivity or dielectric tensor. (Of course, the tensors in the different grains are generally related by a similarity transformation). A polycrystalline elastic material is a more complicated version of the same problem, since each grain has a different fourth-rank tensor. Quantitative models for the properties of heterogeneous materials have been discussed since the early $19^{th}$ century [27]. This long-standing attention has led to the presentation of numerous effective medium formulations, being either purely phenomenological or based on more or less sound theories, as treated in several reviews. During the last few years, the interest in the optical properties of metal-dielectric mixtures has soared owing to their importance for efficient photothermal conversion of solar energy.

Two effective medium theories have become particularly popular; these are usually ascribed to Garnett (known as the Maxwell Garnett theory) and to Bruggeman. The differences between the mathematical structures of the two theories have been known for some years, but a more intuitive physical understanding for the circumstances under which the two formulations apply is only presently emerging. All these EMA calculations are particularly appropriate for composites and polycrystals in which the grains of the various components are randomly and

symmetrically distributed, so that none of the components is identifiable as a host in which the others are preferentially embedded.

### 2.3.1 Maxwell Garnett theory

The Maxwell Garnett(MG) approximation, also known as the Clausius-Mossotti approximation, is one of the most widely used methods for calculating the bulk dielectric properties of inhomogeneous materials. It is useful when one of the components can be considered as a host in which inclusions of the other components are embedded. It involves an exact calculation of the field induced in the uniform host by a single spherical or ellipsoidal inclusion and an approximate treatment of its distortion by the electrostatic interaction between the different inclusions. This distortion is caused by the charge dipoles and higher multipoles induced in the other inclusions. The induced dipole moments cause the longest range distortions and their average effect is included in the MG approximation which results in a uniform field inside all the inclusions. This approach has been extensively used for studying the properties of two-component mixtures in which both the host and the inclusions are isotropic materials with scalar dielectric coefficients [28, 29, 30]. It has also been applied in the study of the Hall effect in inhomogeneous materials, where the components have tensor electrical conductivities under applied magnetic field. There are many possible locally anisotropic inhomogeneous materials in which the local dielectric coefficient is a tensor. Of these, the most commonly studied are polycrystalline aggregates of a single anisotropic component. In these materials the inhomogeneity is provided by the random variation of the crystal orientation throughout the system. Many of these studies use the effective-medium approximation. This approximation is based on a self-consistent procedure in which a grain of one of the components is assumed to have a convenient shape (usually spherical or ellipsoidal) and to be embedded in an effective medium whose properties are determined self-consistently.

Consider a random medium composed of core-shell dielectric cylinders of infinite length, shown in Fig. 2.4, embedded in a background medium with a dielectric constant of $\varepsilon_m$. The volume fraction occupied by the inclusions is f and the structure of the core-shell cylinders is shown in the inset of Fig. 2.4. As known, when the incident wavelength $\lambda$ is much larger than the size of the inclusions, the electromagnetic response of the inclusion can be regarded as a point dipole $\overrightarrow{P}$, and the summation over the total responses of the inclusions within a unit space gives the electric polarization of the random medium.

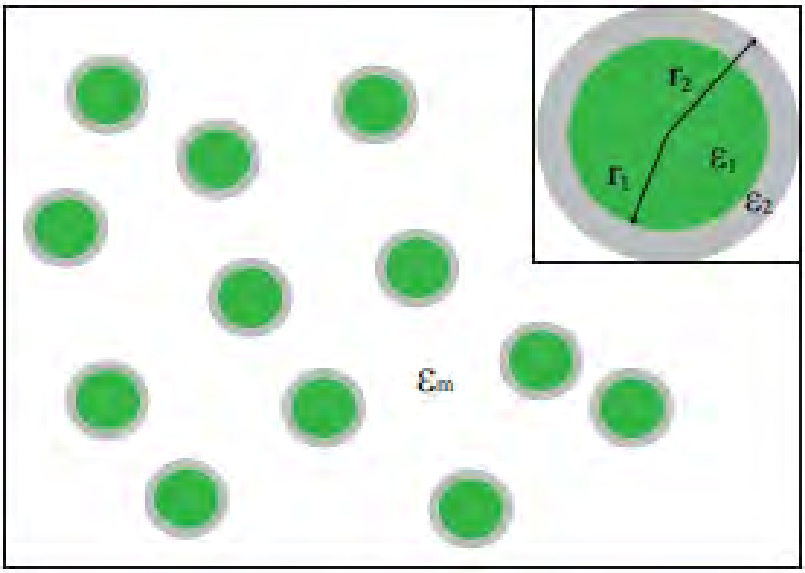


**Figure 2.4:** Schematic view of a random medium composed of core-shell cylinders of infinite length. The positions of the cylinders are random. The inset is the core-shell dielectric cylinders embedded in the background with a dielectric constant of $\varepsilon_m$.

$$\overrightarrow{P} = \frac{\sum \overrightarrow{P_i}}{\Delta V}, \tag{2.3.1}$$

According to the relation between electric displacement $\overrightarrow{D}$ and electric field $\overrightarrow{E}$, i.e.

$$\overrightarrow{D} = \varepsilon_0 \overrightarrow{E} + \overrightarrow{P}, \tag{2.3.2}$$

the effective dielectric constant to describe the macroscopic effects of the electromagnetic responses of the inclusions can be defined via

$$\overrightarrow{D} = \varepsilon_{eff}\overrightarrow{E}, \tag{2.3.3}$$

Moreover, the average electric displacement and electric field can be given by the weighted average determined by the corresponding values distributed within the respective layers

$$\overrightarrow{D} = f[\eta\varepsilon_1\overrightarrow{E}_1 + (1-\eta)\varepsilon_2\overrightarrow{E}_2] + (1-f)\varepsilon_m\overrightarrow{E}_e, \tag{2.3.4}$$

$$\overrightarrow{E} = f[\eta\overrightarrow{E}_1 + (1-\eta)\overrightarrow{E}_2] + (1-f)\overrightarrow{E}_e, \tag{2.3.5}$$

where f is the volume fraction occupied by core-shell cylinders, $\eta = \frac{r_1^2}{r_2^2}$, $\overrightarrow{E}_1$, $\overrightarrow{E}_2$ and $\overrightarrow{E}_e$ are the electric field distributed within the core-shell, layer of the cylinder,and the background medium, respectively. According to Eqs. 2.3.3, 2.3.4 and 2.3.5 and the formulae for the electric field $E_i(i = 1, 2)$ within the core-shell cylinders, generally, the formulae for the effective dielectric constant $\varepsilon_{eff}$ for a random medium composed of core-shell cylinders of infinite length is approximately given by

$$\varepsilon_{eff} = \frac{\varepsilon_m + f[\eta\varepsilon_1 a_1 + (1-\eta)\varepsilon_2 a_2 - \varepsilon_m]}{1 + f[\eta a_1 + (1-\eta)a_2 - 1}, \tag{2.3.6}$$

where the parameters $a_1$ and $a_2$ are defined as the ratios between $\frac{\overrightarrow{E_i}}{\overrightarrow{E_e}}$ (i=1,2). The Eq. 2.3.6 is also known as the Maxwell-Garnett formula. Considering the boundary conditions,the electric fields within the multilayered cylinder for S-mode waves are continuous, i.e. $\overrightarrow{E_1} = \overrightarrow{E_2} = \overrightarrow{E_e}$, therefore, $a_1 = a_2 = 1$ Thus, according to Eq. 2.3.6, the effective dielectric constant $\varepsilon_{eff}$ for S-mode waves can be written directly by

$$\varepsilon_{eff} = (1-f)\varepsilon_m + f[\eta\varepsilon_1 + (1-\eta)\varepsilon_2]. \tag{2.3.7}$$

However,the case for P-mode waves is more complicated,and herein,the field distribution of the electric fields within the coreshell cylinders for P mode is derived and $a_1$ and $a_2$ are respectively given by

$$a_1 = \frac{4\varepsilon_m\varepsilon_2}{(\varepsilon_1+\varepsilon_2)(\varepsilon_2+\varepsilon_m) - \eta(\varepsilon_2-\varepsilon_1)(\varepsilon_2-\varepsilon_m)}, \tag{2.3.8}$$

$$a_2 = \frac{2\varepsilon_m(\varepsilon_1+\varepsilon_2)}{(\varepsilon_1+\varepsilon_2)(\varepsilon_2+\varepsilon_m)-\eta(\varepsilon_2-\varepsilon_1)(\varepsilon_2-\varepsilon_m)}. \tag{2.3.9}$$

Therefore, the final solution of $\varepsilon_{eff}$ for P-mode waves can be obtained subsequently.

### 2.3.2 Coated coherent potential approximation method

The coated coherent potential approximation (CCPA) method is conducted as well to calculate the effective index of the random system composed of core-shell dielectric cylinders of infinite length. The mechanism of the CCPA method is based on the physical idea that the distribution of the electromagnetic energy within a random medium should be homogeneous after being configurationally averaged over the correlation length of the random media. Therefore, the averaged forward-scattering amplitude of a cylindrical region within the random medium should be approximately equal to zero. In addition, in order to take into account the effects of the structural factor for the multiple scatterings occurring within the random medium, a coated layer is involved to the real cylinder, which is embedded in the effective medium as an effective scattering unit. The radius of the coated layer is given by $r_c = r_2 f^{-1/2}$. The schematic view of the CCPA method is shown in Fig. 2.5. It has been shown by Busch et al. that the effective medium obtained by the CCPA method for random media composed of dielectric spheres are in reasonable agreement with experiments [31, 32, 33]. According to

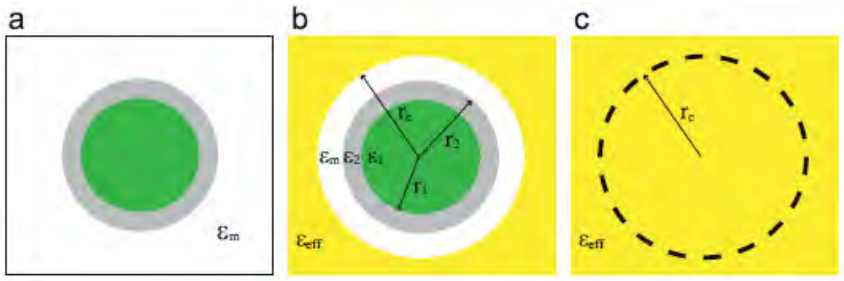


**Figure 2.5:** Schematic view of the CCPA method for random media composed of coreshell dielectric cylinders, illustrated in (a). The coated layer to the actual coreshell cylinders in (b) has the size of $r_c$ and the dielectric constant equal to $\varepsilon_m$. (c) The dashed region indicates the effective scattering unit described in the CCPA method.

the CCPA theory which gives that the coated scattering unit illuminated by a plane wave has a scattering pattern similar to that of its averaged counterpart, thus, the electromagnetic energy contained in the coated cylinder in Fig. 2.5(b) should be equal to that contained in the dashed volume in Fig. 2.5 (c), which subsequently gives the main equation for the CCPA method as follows:

$$\int_0^{r_c} d^3\overrightarrow{r}\rho_E^{(1)}(\overrightarrow{r}) = \int_0^{r_c} d^3\overrightarrow{r}\rho_E^{(2)}(\overrightarrow{r}), \tag{2.3.10}$$

where $\rho_E^{(1)}$ and $\rho_E^{(2)}$ represent the electromagnetic energy density within the three-layered cylinder in Fig. 2.5 (b) and that of the averaged volume with an effective $\varepsilon_{eff}$ in Fig. 2.5 (c), respectively. In addition, as known, the energy density for an electromagnetic vectorial field is given by

$$\rho_E(\overrightarrow{r}) = \frac{1}{2}[\varepsilon(\overrightarrow{r})|\overrightarrow{E}(\overrightarrow{r})|^2 + \mu(\overrightarrow{r})|\overrightarrow{H}(\overrightarrow{r}|)^2], \tag{2.3.11}$$

here we only deal with non-magnetic materials, so $\frac{\mu}{\mu_0} = 1$. The self-consistent equation, i.e. Eq. 2.3.10, can be solved by an iterative procedure.

### 2.3.3 Discrete Dipole Approximation

The Discrete Dipole Approximation (DDA) is developed by Purcell and Pennypacker, it is numerical technique for computing electromagnetic scattering and absorption by targets of arbitrary shape [34, 35, 36], where the continuum target is approximated by a finite point array. In response to the local electric field each point acquires a dipole moment and the scattering problem can then be solved in a self-consistent way. Thus, in principle this method is completely flexible regarding the geometry of the target, the only limitation is given by the need to use an inter dipole separation that is small compared to any structural lengths in the target and to the wavelength. For a finite array of point dipoles the scattering problem may be solved exactly, so the only approximation that is present in the DDA is the replacement of the continuum target by an array of N-point dipoles. The basic idea of the DDA was already known in 1964, but it was limited to structures that were small compared to the wavelength. This limitation disappeared, when

Purcell and Pennypacker introduced the DDA to study interstellar dust grains in 1973 [35]. The DDA the problem of electromagnetic scattering of an incident light wave can then be cast to the following simple matrix equation as

$$\overline{AP} = \overline{E_{inc}}, \tag{2.3.12}$$

where $\overline{E_{inc}}$ is a 3N-dimensional (complex) vector of the incident electric field at the N lattice sites, $\overline{P}$ is a 3N-dimensional (complex) vector of the (unknown) dipole polarizations, and $\overline{A}$ is a 3Nx3N complex matrix.

Assuming a point lattice with N occupied sites and an index j = 1, . . . , N running over these elements. Each dipole j is characterized by a polarizability tensor $\alpha_j$ , which is diagonal with equal components if the material is isotropic (i.e., $\alpha_j$ may be treated as a scalar quantity in this case) where all individual dipole polarizability tensors can be simultaneously diagonalized, although it is straightforward to generalize the problem to non diagonal tensors. Let $P_j$ be the instantaneous complex dipole moment of dipole j, and $E_{ext}, j$ the instantaneous complex electric field at position j due to the incident radiation plus the other N-1 oscillating dipoles. Then we get

$$P_j = \alpha_j E_{ext,j}, \tag{2.3.13}$$

$$P_j = \alpha_j (E_{inc,j} - \sum A_{jk} P_k), \tag{2.3.14}$$

in this case $j \neq k$ where $E_{inc}, j$ corresponds to the electric field of the incident plane wave at position j.

$$E_{inc}, j = E_0 e^{(ik.r_j - i\omega t)} \alpha_j, \tag{2.3.15}$$

and $\sum A_{jk} P_k$ is the contribution to the electric field at position j due to the dipole at position k.

## 2.4 Spherical particles: The quasi-static approximation

Rayleigh theory, presumes the particles to respond to the applied, time-varying electric field of the radiation as an oscillating dipole which radiates scattered fields

in all directions. The induced dipole moment of the particle is a vector quantity proportional to the applied electric field through the polarizability tensor, which can be determined analytically. The polarizability of a material is often isotropic, in which case it can be treated as a scalar. The theory used in our study considers the assumption of scattering and absorption of electromagnetic radiation by metal-dielectric nanocomposite having $d \ll \lambda$. The simplest scenario to consider consists of a non-magnetic ($\mu_0 = \mu$) spherical and cylindrical inclusions embedded in a homogeneous, linear and isotropic medium that is non-absorbing. It is assumed that the particle initially experiences a uniformly polarized field throughout the entire volume of the sphere. Phase shifts that would exist in a non-uniform field are neglected, thus multipolar resonances predicted by Mie theory are restricted to the dipole mode. For small size dielectric particles, the scattering cross-section will increase with increasing refractive index. This result follows from the Rayleigh theory and is indicative of the important role of dipole scattering. The mode is induced by the movement of the electrons relative to the positively charged ion cores of the atomic nuclei under the influence of the externally applied electric field. Provided the permittivities of the sphere and the external medium are different a charge is developed at the surface resulting in a polarization field within the particle. The external field is modified by the electromagnetic field generated by the polarization charge. Standard methods in electrostatics can be applied to derive expressions for the electric fields inside ($E_1$) and outside ($E_2$) the sphere from the scalar potentials $\varphi_1(r, \theta)$ and $\varphi_2(r, \theta)$ using

$$E_i = -\nabla\varphi_i, i = 1, 2, \tag{2.4.1}$$

and the Laplace equation

$$\nabla\varphi_i = 0, \tag{2.4.2}$$

The boundary conditions at the interface (r = a) between the sphere and the medium necessitate that the potential is continuous $\varphi_1 = \varphi_2$ and that their radial

derivatives satisfy

$$\varepsilon_1 \frac{\partial \varphi_1}{\partial r} = \varepsilon_2 \frac{\partial \varphi_2}{\partial r}, \tag{2.4.3}$$

where $\varepsilon_1$ is the complex permittivity of the particle and $\varepsilon_2$ is the permittivity of the external medium. A further condition is that far from the particle the field is unperturbed by the particle:

$$E_2 = E_0 (r \to \infty), \tag{2.4.4}$$

$$\varphi_2 = -E_0 z = -E_0 r \cos(\theta), \tag{2.4.5}$$

and is equal to the incident field now defined as $E_0 = E_0 z$. Solving Eq. 2.4.2 and applying the boundary conditions yields the following expressions for the potential inside $\varphi_1$ and outside $\varphi_2$ the sphere,

$$\varphi_1 = \frac{3\varepsilon_2}{\varepsilon_1 + 2\varepsilon_2} E_0 r \cos(\theta), \tag{2.4.6}$$

$$\varphi_2 = -E_0 r \cos(\theta) + a^3 E_0 \frac{\varepsilon_1 - \varepsilon_2}{\varepsilon_1 + 2\varepsilon_2} \frac{\cos(\theta)}{r^2}, \tag{2.4.7}$$

Instantly one can see by comparison with Eq. 2.4.5 that the field outside of the sphere is a superposition of the incident field and the field generated by the particle. By comparison with the equation for the potential due to an ideal dipole

$$\varphi = \frac{p.r}{4\Pi\varepsilon_2 r^3} = \frac{p}{4\Pi\varepsilon_2} \frac{\cos(\theta)}{r^2}, \tag{2.4.8}$$

where p is the dipole moment, the second term in Eq. 2.4.7 is identified as being that of an ideal dipole with moment

$$P = 4\Pi a^3 \frac{\varepsilon_1 - \varepsilon_2}{\varepsilon_1 + 2\varepsilon_2} \varepsilon_2 E_0, \tag{2.4.9}$$

and polarizability $\alpha$,

$$\alpha = 4\Pi a^3 \frac{\varepsilon_1 - \varepsilon_2}{\varepsilon_1 + 2\varepsilon_2}. \tag{2.4.10}$$

The derivation above has required a spatially constant electric field and has neglected the application of a time-varying electric field. An electromagnetic wave incident on a sphere as defined above naturally has a time-varying electric field and therefore when applying electrostatic theory to these situations is often referred to

as the quasi-static approximation. This acknowledges that although spatially invariant at an instant in time, the particle experiences a field with a time dependent phase. The polarizability is related to the absorption and scattering cross-sections by

$$C_{sca} = \frac{k^4}{6\Pi}|\alpha^2|, \tag{2.4.11}$$

$$C_{abs} = kIm\{\alpha\}, \tag{2.4.12}$$

yielding, upon substitution of the polarisability in equation 2.5.14

$$C_{sca} = \Pi a^2 \frac{8}{3} x^4 |\frac{\varepsilon_1 - \varepsilon_2}{\varepsilon_1 + 2\varepsilon_2}|^2, \tag{2.4.13}$$

$$C_{abs} = \Pi a^2 4x Im\{\frac{\varepsilon_1 - \varepsilon_2}{\varepsilon_1 + 2\varepsilon_2}\}. \tag{2.4.14}$$

where $x = ka = \frac{2\Pi a n_2}{\lambda}$ is the size parameter. From these relations it is clear how the absorption, scattering and extinction from a particle small compared to the wavelength depend on the size, wavelength and relative permittivities of the particle and the external medium. For a small particle consisting of a material with a dielectric function only weakly dependent on the frequency of the incident radiation and satisfying the conditions above the absorption is proportional to $\frac{1}{\lambda}$ and the scattering intensity proportional to $\frac{1}{\lambda^4}$. This is known as Rayleigh scattering after Lord Rayleigh who used the relationship to explain the color of a clear blue sky in 1871.

## 2.5 Mie theory

The most widely used rigorous scattering theory for particles has been Mie theory (Mie 1908) [2], providing a general framework enabling exact solutions to the problem of light scattering by an arbitrary sphere. In his original work Mie solved Maxwells equations using appropriate boundary conditions with the system expressed in spherical polar coordinates. The Mie theory extends the Rayleigh theory of light scattering to objects of size of the order and bigger than the wavelength. The use of scattering techniques to characterize structures is most effective when

there is strong coupling between the features in a structure and the probe radiation. The theory describes the scattering of electromagnetic radiation of arbitrary wavelength by an isolated, optically isotropic sphere of arbitrary diameter. The advantage of Mie theory is that it is easily implemented computationally where the disadvantage of Mie theory is limited to a spherical particle and is not applicable to the systems in which the scattering features are irregularly shaped and/or optically anisotropic [7]. The incoming electromagnetic field was represented as multipole expansions of a transverse electric (magnetic) wave and transverse magnetic (electric) wave. Magnetic and electric scalar potentials were introduced to describe the components of the incident, scattered and internal fields each being a solution to the scalar wave equation. A more general approach is to expand the incident, scattered and internal fields in terms of spherical vector wave harmonics as detailed by Bohren and Huffman (1983) [3] and Van de Hulst (1957) [6]. A reduced description follows detailing the main points. To begin Maxwells equations are expressed in the complex representation given in ref. [37]:

$$\nabla.E = 0, \tag{2.5.1}$$

$$\nabla.H = 0, \tag{2.5.2}$$

$$\nabla \times E = i\omega\mu H, \tag{2.5.3}$$

$$\nabla \times H = -i\omega\varepsilon E, \tag{2.5.4}$$

From these equations it is possible to show that the time-harmonic vector fields E and H in a linear, isotropic, homogeneous medium are solutions of the vector wave equations

$$\nabla^2 E + k^2 E = 0, \tag{2.5.5}$$

$$\nabla^2 H + k^2 H = 0, \tag{2.5.6}$$

where $k^2 = \omega^2\varepsilon\mu$. The vector functions

$$M = \nabla \times a\psi, N = \frac{1}{k}\nabla \times M, \tag{2.5.7}$$

where $\psi$ is a scalar function, k is the wave vector and a is an arbitrary constant vector are defined in such a way that they satisfy the equation

$$\nabla^2 C + k^2 C = \nabla \times [a(\nabla^2 \psi + k^2 \psi)], \tag{2.5.8}$$

where C represents either of the two vector functions. From this it is seen that subject to $\psi$ satisfying the scalar wave equation

$$\nabla^2 \psi + k^2 \psi = 0, \tag{2.5.9}$$

M and N are both solutions to the vector wave equation. Moreover, the particular solutions of Eq. 2.5.9 that are finite, continuous and single-valued form a discrete set with each separate solution denoted as $\psi_n$. Associated with the $\psi_n$ are the discrete vector functions $M_n$ and $N_n$ that linearly combined can be used to represent any arbitrary wave function. These are the spherical vector wave harmonics. It is seen from Eq. 2.5.7 that the divergence of the vectors M and N vanish and furthermore that M can be expressed as a function of N. Therefore the following three conditions supplement the definitions of M and N in Eq. 2.5.7 :

$$\nabla . M = 0, \nabla . N = 0, M = \frac{1}{k} \nabla \times N, \tag{2.5.10}$$

The vectors M and N have all the properties of an electromagnetic field in that they are each proportional to the curl of the other and are divergence-free. Therefore the fields E and H may be represented by a linear combination of the vectors M and N

$$E = -\sum_n A_n M_n + B_n N_n, H = i\omega\varepsilon k \sum_n A_n N_n + B_n M_n, \tag{2.5.11}$$

Using this approach finding solutions to the electromagnetic field equations has been reduced to finding solutions to the scalar wave equation. Until this point the choice of the scalar function $\psi$ (called the generating function) and vector a (called the pilot vector) has been arbitrary. The pilot vector is chosen to be the radius vector r as this ensures M is a solution to the vector wave equation in spherical polar coordinates. The form of $\psi$ is governed by the symmetry of the problem and

is in this case most suitably expressed in terms of a spherical coordinate system with even and odd separable solutions to the scalar wave equation given by

$$\psi_{emn}(r,\theta,\varphi) = R(r)\Theta(\theta)\phi(\varphi) = \cos(m\varphi)P_n^m(\cos\theta)Z_n(kr), \tag{2.5.12}$$

$$\psi_{omn} = \sin(m\varphi)P_n^m(\cos\theta)Z_n(kr), \tag{2.5.13}$$

where $z_n(kr)$ represents spherical Bessel functions of the first, second and third kind and the $P_n^m(\cos\theta)$ are associated Legendre polynomials. By substituting Eq. 2.5.12 and Eq. 2.5.13 into the equations for M and N the vector spherical harmonics appropriate for the representation of the electromagnetic fields E and H are derived. In terms of the spherical harmonics the expansion of the plane wave is given for an arbitrary polarization by

$$E_i = \sum_{m=0}^{\infty}\sum_{n=m}^{\infty}(B_{emn}M_{emn} + A_{emn}N_{emn} + B_{omn}M_{omn} + A_{omn}N_{omn}), \tag{2.5.14}$$

The coefficients A and B are determined by considering the orthogonality of the spherical harmonics and applying the restriction that the wave is polarized in the x-direction. The coefficients $A_{omn} = B_{emn} = 0$ for all m and n and all coefficients vanish for $m \neq 1$ leading to

$$E_i = E_0\sum_{n=1}^{\infty} i^n\frac{2n+1}{n(n+1)}(M_{o1n}^{(1)} - iN_{e1n}^{(1)}), \tag{2.5.15}$$

where the superscript (1) denotes the incorporation of the Bessel function of the first kind, $j_n(kr)$ into the generating functions $\psi_{o1n}$. This choice is based on the requirement that the field is finite at the origin. Taking the curl of Eq. 2.5.15 provides the corresponding incident magnetic field,

$$H_i = -\frac{k_2}{\omega\mu_2}E_0\sum_{n=1}^{\infty} i^n\frac{2n+1}{n(n+1)}(M_{e1n}^{(1)} + iN_{o1n}^{(1)}), \tag{2.5.16}$$

The incident field expansions used in conjunction with the boundary conditions for E and H at the boundary of the particle

$$(E_i + E_s - E_1)\times\hat{e_r} = 0, \tag{2.5.17}$$

$$(H_i + H_s - H_1)\times\hat{e_r} = 0, \tag{2.5.18}$$

generate the following expressions for the scattered fields $(E_s, H_s)$ and the internal fields $(E_1, H_1)$:

$$E_1 = \sum_{n=1}^{\infty} E_n(c_n(M_{o1n}^{(1)} - id_n N_{e1n}^{(1)})), \tag{2.5.19}$$

$$H_1 = -\frac{k_1}{\omega\mu_1} \sum_{n=1}^{\infty} E_n(d_n(M_{e1n}^{(1)} + ic_n N_{o1n}^{(1)})), \tag{2.5.20}$$

$$E_s = \sum_{n=1}^{\infty} E_n(ia_n(N_{e1n}^{(3)} - b_n M_{o1n}^{(3)})), \tag{2.5.21}$$

$$H_s = -\frac{k_2}{\omega\mu_2} \sum_{n=1}^{\infty} E_n(ib_n(N_{o1n}^{(3)} + a_n M_{o1n}^{(3)})), \tag{2.5.22}$$

where

$$E_n = i^n E_0 \frac{2n+1}{n(n+1)}, \tag{2.5.23}$$

$a_n$ and $b_n$ are the scattered field coefficients and $c_n$ and $d_n$ are the internal field coefficients. The superscript (3) in the scattered field equations represents the incorporation of Bessel functions of the third kind. These are linear combinations of the first and second order Bessel functions and are often referred to as Hankel functions [37]. The coefficients $a_n$ and $b_n$ are derived from these functions and are given by

$$a_n = \frac{m\psi_n(mx)\psi\prime_n(x) - \psi_n(x)\psi\prime_n(mx)}{m\psi_n(mx)\xi\prime_n(x) - \xi_n(x)\psi\prime_n(mx)}, \tag{2.5.24}$$

$$b_n = \frac{\psi_n(mx)\psi\prime_n(x) - m\psi_n(x)\psi\prime_n(mx)}{\psi_n(mx)\xi\prime_n(x) - m\xi_n(x)\psi\prime_n(mx)}, \tag{2.5.25}$$

where $m = n_1/n_2$ is the relative refractive index ($n_1$ is the complex refractive index of the particle, $n_2$ is the refractive index of the surrounding medium), $x = \frac{2\Pi n_2 a}{\lambda}$ (a is the radius of the sphere and $\lambda$ is the wavelength in vacuum), $\psi_n$ and $\xi_n$ are the Riccati-Bessel functions and the permeabilities $\mu_1 = \mu_2 = 1$. With the scattering coefficients $a_n$ and $b_n$ the extinction and scattering cross-sections for a spherical particle are derived by substituting Eqn. 2.5.26 into 2.5.27

$$S_{inc} = \frac{1}{2}Re\{E_{inc}\times H_{inc}^*\}, S_{sca} = \frac{1}{2}Re\{E_{sca}\times H_{sca}^*\}, S_{exs} = \frac{1}{2}Re\{E_{ins}\times H_{sca}^* + E_{sca}\times H_{inc}^*\} \tag{2.5.26}$$

into

$$W_{inc} = -\int_A S_{inc}.\hat{e}_r dA, W_{sca} = \int_A S_{sca}.\hat{e}_r dA, W_{ext} = -\int_A S_{ext}.\hat{e}_r dA, \quad (2.5.27)$$

where $S_{inc}$ is the Poynting vector of the incident wave, $S_{sca}$ is the pointing vector of the scattered wave, $S_{ext}$ is the Poynting vector associated with some interaction between the incident and scattered waves, and $S = S_{inc} + S_{sca} + S_{ext}$ with $W_{abs} = W_{inc} - W_{sca} + W_{ext}$ The rate at which energy is scattered across the surface of the reference sphere is $W_{sca}$, and for a non-absorbing medium the energy flow of the incident beam $W_{inc}$ vanishes when integrated over a closed surface. Therefore $W_{ext}$ is, by conservation of energy, simply the addition of the scattering term and the absorption term $W_{ext} = W_{sca} + W_{abs}$ For convenience the extinction, scattering and absorption are often referred to by their respective cross-sections. This means that the total energy scattered in all directions is equal to the energy from the incident wave falling upon an area equal to the scattering cross-section $C_{sca}$. Similarly the absorption cross-section Cabs is defined as the equivalent area upon which energy from the incident wave is absorbed, and the extinction cross-section $C_{ext}$ is defined as the sum of the scattering and absorption cross-sections. Therefore, the net energy scattered through an arbitrary spherical surface centered at the origin and the net extinction will be given by [38]:

$$W_{sca} = \frac{1}{2}\int_0^{2\Pi}\int_0^{\Pi}(E_{s\theta}H^*_{s\varphi} - E_{s\varphi}H^*_{s\theta})r^2\sin(\theta)d\theta d\varphi, \quad (2.5.28)$$

$$W_{ext} = \frac{1}{2}\int_0^{2\Pi}\int_0^{\Pi}(E_{i\varphi}H^*_{s\theta} - E_{i\theta}H^*_{s\varphi} - E_{s\theta}H^*_{i\varphi} + E_{s\varphi}H^*_{i\theta})r^2\sin(\theta)d\theta d\varphi, \quad (2.5.29)$$

The next step is to use the calculated electric and magnetic fields to find explicit expressions for the scattering and extinction cross-sections. Evaluating the integrals yields:

$$C_{sca} = \frac{2\Pi}{k^2}\sum_{n=1}^{\infty}(2n+1)(|a_n|^2 + |b_n|^2), \quad (2.5.30)$$

$$C_{ext} = \frac{2\Pi}{k^2}\sum_{n=1}^{\infty}(2n+1)Re\{|a_n| + |b_n|\}, \quad (2.5.31)$$

where k is the wave vector of the incident plane wave. These expressions can be solved computationally or in certain limiting cases simplified to produce approximate solutions that may provide some insight into the physical behavior of the particles. One such case is when the particle is small compared to the wavelength of the incident light, $x \ll 1$. Expanding the spherical Bessel functions as a power series and considering only those terms of the order $x^6$ and below results in the following approximations for the scattering and absorption efficiencies,

$$Q_{sca} = \frac{8}{3}x^4|\frac{m^2-1}{m^2+2}|^2, \tag{2.5.32}$$

$$Q_{abs} = 4xIm\{\frac{m^2-1}{m^2+2}\}. \tag{2.5.33}$$

The coefficients $a_1, a_2$ and $b_1$ all contain terms up to the order $x^6$, however Eq. 2.5.32 and Eq. 2.5.33 stem from the coefficient $a_1$, the other terms neglected as they become negligible as $x \to 0$. These results are directly comparable with those derived for the absorption and scattering cross-sections using the quasistatic approximation [39, 40]. This illustrates that in the limit of $a \to 0$ the scattering problem of Mie theory reduces to that of electrostatic theory. At this point it is worth emphasizing the limitations imposed given that the particles studied in this thesis are different to those to which the theory applies. Non-spherical particles exhibit very different optical spectra compared to those modelled in Mie theory [41, 42]. In addition the interactions between particles that are often present in samples are completely neglected. However, by using Mie theory it is possible to gain insight into many features in the optical spectra obtained from arbitrarily shaped particles [43, 44].

# Chapter 3

# Fano resonances in composite nanoparticles

## 3.1 Introduction

### 3.1.1 Overview of Fano resonances

The resonance phenomenon is typically considered to be an enhancement of the response of some system to an external excitation at a specific frequency. Many physical systems exhibit such phenomenon. It was first acknowledged by Galileo Galilei in 1602 while working on musical strings. Latter, it was established that mechanical, acoustic and electromagnetic resonances are a universal feature of many kinds of classical and quantum system [9]. These resonances were explained by the symmetrical Lorentzian formula, which was considered to be a fundamental line shape of a resonance for many years. Ugo Fano, an Italian physicist experimentally observed a new kind of asymmetric line shape of a resonance in the absorption spectra of noble gases in 1935 [45]. The nature of the asymmetry is then theoretically explained by him in a quantum mechanical study of the autoionizing states of atoms in 1961 that now bears his name (Fano) [46]. Fano theory hence explained that the sharp asymmetric line profile arises due to the overlapping of a discrete state with a continuum state, where destructive and constructive interference phenomena take place at close energy positions. In 1931, Ettore Majorana draw similar conclusion while working on the selection rules for

the non-radiative decay of two electronic excitations in atomic spectra, involving the configuration interaction between discrete and continuum channels [47]. His work presents a vital step for understanding the 1935 work of Ugo Fano on the asymmetric line shape of two electron excitations. The first asymmetric line shape was traced by Wood in 1902 that now connects to plasmonics field. While working on metallic grating, he was astonished to see that under special illumination conditions, the grating efficiency goes up and down. These hasty variations in the intensities were named Woods anomalies. However, no satisfying description was found at that time. So the first understanding of the profile was provided by Fano by suggesting that anomalies could be associated with the excitation of a surface waves along the grating. This phenomenon has been studied extensively for quantum systems and in the classical system of coupling oscillators [23]. Nowadays, Fano resonances have been observed in various systems including quantum dots , nanowires and tunnel junctions, bilayer graphene structures , plasmon scattering in Josephson-junction networks [48] and matter-wave scattering in ultra-cold atom systems [49] plus in numerous optical systems such as strong coupling between Mie and Bragg scattering in photonic crystals and metamaterials [50, 51]. In all these systems, the most emerging technology is the field of plasmonics that squeezes electromagnetic waves into nanoscale structures and this technology proved to be a keen platform in the generation of Fano resonances.

The direct optical excitation of surface plasmons on metallic nanostructures offers several techniques to control and manipulate light at nanoscale dimensions such as varying the geometry or composition of nanoparticles etc. Localized surface plasmon resonances (LSPR) are charge density oscillations on the closed surfaces of the noble metal nanoparticles such as gold and silver. They have potential applications in chemical and bimolecular sensing because the LSPR can be tuned from visible to near infrared region by changing the shape, size and local dielectric environment of the plasmonic nanoparticles [52, 53]. LSPR have the capability to

effectively scatter, absorb and squash light, creating large enhancement of electromagnetic field amplitudes due to which it can be used for Raman scattering or infrared absorption spectroscopy applications.

Plasmonic systems are a perfect option to produce Fano resonances with sharp dispersion, which make them promising for sensing applications. In such systems, the Fano resonances are accomplished through the interference of a plasmon resonance, which acts as a continuum state, with a discrete state. For example, in the interference of two different excitation path ways, if in one path the continuum state is excited and in the other path a discrete state then Fano resonances will take place [54]. The Fano line shape is quite different from the symmetric Lorentzian line shape and is analogous to the electromagnetic induced transparency (EIT) in atomic system. In a three-level atomic system, EIT usually emerges due to a quantum destructive interference between two pathways provoked by another field that can build an absorptive medium transparent to the probe field. So in metallic nanostructures, Fano resonance is similar to EIT by rising a phenomenon known as Plasmon Induced Transparency (PIT) [55, 56]. Recently, several plasmonic nanostructures have been investigated widely both theoretically and experimentally to study the effect of higher order dark multipolar modes and Fano resonances. These nanostructures include nanodisks , nanorods, nanorice, nanoshells, ring/disk nanocavities, nanocross, dolmen structures, dimers, trimers, quadrumers, pentamers, heptamers and nanoparticle chains [45]. These nanostructures are among the most important future optical materials for new devices, containing sensors, logic circuits, slow light components and metamaterials. The Fano resonances in these nanostructures can be achieved either by the interaction of (anti parallel) dipolar modes or by the interactions of the dipolar mode with higher order modes, like the quadrupole and the octupole modes. When the size of the nanostructure is very small compared to the wavelength of incident light (Rayleigh limit ($\lambda \gg d$)) then only dipolar modes are excited by the incident light. The higher order dark modes can be excited either by increases the size of

the nanoparticle or by symmetry breaking.

Surface plasmons are the combined oscillations of conduction and bound electrons in metallic nanoparticles driven by an external electromagnetic field at optical frequencies, which is accountable for the considerable enhancement of the electric field in the vicinity of metallic nanoparticles and for the rich and complex features of the scattered light. A number of applications, such as chemical and bimolecular sensing, photo thermal cancer therapy, metamaterials and surface-enhanced Raman spectroscopy (SERS), are based on surface plasmons. Several plasmonic nanostructures has been proposed to achieve Fano resonances in their optical spectra. They have received much attention due to hasty progress in the fabrication and characterization techniques [57, 58, 59, 60].

Single nanoparticle can support different plasmon modes with distinct line widths. Broad dipolar plasmon modes possess finite dipole moments and can couple well to incident light. They are usually named as bright modes. The resonance peak of the bright plasmon modes is spectrally broadened by reason of radiative damping. On the other hand, narrow plasmon modes acquire zero or almost zero dipole moments. They do not couple efficiently to the external electromagnetic field, therefore not radiatively broadened. They are usually named as dark modes [61]. The existence of both the bright and dark modes in a nanostructure results in Fano resonances. For complex nanostructures of arbitrary shape, the plasmonic response can be understand using a powerful tool know as plasmon hybridization model [62, 63]. The splitting of the modal energies into bonding and antibonding modes is due to the coupling between individual plasmon modes. Several plasmonic nanostructures exhibiting Fano resonances in their optical responses are briefly explained below.

### 3.1.2 Manifestation of Fano resonance in different structures

Reported study showed that single nanoparticle usually exhibits a single bright dipole mode. However, Fang et al., have achieved Fano resonance in a single planar nanodisk nanoparticle by the symmetry breaking conception [64]. Symmetry is broken by removing a slice form the disk in wedge shape due to which the interactions between a hybridized dipolar plasmon mode of the disk and a narrower quadrupolar mode of the wedge-shaped slice occur, which results in a Fano resonance. Both the nanodisk size and wedge angle control the properties of the Fano resonance. They also demonstrated a semi-analytical method that provides a useful way to investigate coherent coupling and Fano line shapes in a single planar nanostructure. The reduced symmetry nanodisk was fabricated using electron-beam lithography in a positive resist on a silica substrate. The nanostructures were generated by electron beam evaporation followed by a lift-off process. Scanning electron microscopy was used to obtained the normal incidence images of the fabricated structures. They suggested that, this nanostructure can be used in metamaterials, slow light, electromagnetically induced transparency, and light bending and switching applications. Reed et al., have demonstrated theoretically the Fano line shapes resulting from silver nanorod, which is due to the coupling of an in plane quadrupole and a dipole mode in the nanostructure. They also observed a new Fano resonance, which occurs when the symmetry of the nanorod is broken and is a result of the asymmetric coupling between the two excited dipoles [65].

### 3.1.3 Fano resonances due to nanoparticles near dielectric substrate

For a nanoparticle in vacuum, there is no coupling and interference between the bright dipolar and dark multipolar modes. Nevertheless, Zhang et al., [66] reported that when the nanocube is deposited on a dielectric substrate, the image of a dipolar mode will have a substantial quadrupolar field component across the nanoparticle, which will introduce a coupling between the dipolar and quadrupolar plasmon modes resulting in a Fano resonance [67]. Their study presents an approach for optimizing the sensitivity of nanostructures, whether chemically synthesized or grown by deposition methods, as high performance localized surface plasmon resonance sensors. Chen et al., [68] have reported a theoretical and experimental study of gold nanorod on dielectric substrate. They showed that, substrates with large dielectric constants can efficiently mediate the hybridization between different plasmon modes in a gold nanorod especially the coupling between quadrupole and octupole modes in a large nanorod, which can produce a Fano resonance in the spectrum similar findings are also reported in ref. [69]. The Fano resonance achieved in a nanorod deposited on dielectric substrate can be tuned or switch on and off by changing the space between the nanoparticle and substrate. Recently, Fernando et al., [70] have suggested two different arrangements of nanoparticles i.e., a colloidal suspension of nanospheroids (nanorice) and a single nanowire with rectangular cross section (nanobelt) on top of a dielectric substrate. Their observation shows the Fano like interference of longitudinal plasmon resonances taking place at individual metallic nanoparticles that can be easily utilize in refractive index sensing. The study also includes numerical analysis of the performance of the two configurations in terms of their figures of merit, which were calculated under realistic conditions.

### 3.1.4 Fano resonances(FR) in coupled oscillators: Classical and Quantum analogy

Fano resonances have been analyzed in various nanostructures however the depth of theory illustrating Fano resonances is complex and difficult to understand in some structures. For this reason, the analogy of Fano resonances in classical resonances in the harmonic oscillator system offers an interesting explanation of the plasmon coupling and the corresponding optical response of the nanostructure [23, 31]. One shared factor among most of the addressed studies is that the dispersion of FR arises due to interference between broad and narrow spectral lines. It has been explained that the broad spectral line in nanostructures can be excited directly by incident light and permanently exists due to Rayleigh scattering. But the best method to create a narrow spectral line in the vicinity of this broad resonance is still a subject of debate due to its challenges. Although extensive research works on FR have been promised to create such narrow spectral lines by indirect excitation of dark modes in plasmonic nanostructures, we intend to present a simple proof by a classical harmonic oscillator system that even in the absence of dark modes, light is capable of exciting two different modes simultaneously equally and directly. It may lead to FR generation even with a high contrast. The analogy of FR in plasmonic systems to the classical resonances in the harmonic oscillator system has been established in various studies recently [71, 72, 73]. The basic feature of such systems has a manifestation as a coupled behavior of two effective oscillators associated with propagating and evanescent waves. The equations of motion of oscillators $|1\rangle$ and $|2\rangle$ can be solved in terms of displacements $x_1$ and $x_2$ from the equilibrium positions:

$$\ddot{x_1} + \gamma_1 \dot{x_1} + \omega_1^2 x_1 - \Omega^2 x_2 = f_1 e^{-i\omega t}, \tag{3.1.1}$$

$$\ddot{x_2} + \gamma_2 \dot{x_2} + \omega_2^2 x_2 - \Omega^2 x_1 = f_2 e^{-i\omega t}, \tag{3.1.2}$$

where $\omega_1$ and $\omega_2$ are oscillation frequencies, corresponding to the oscillators $|1\rangle$ and $|2\rangle$, respectively, and parameter $\Omega$ describes the coupling of the oscillators. $\gamma_1$

and $\gamma_2$ are the friction coefficients, which are used to account for the energy dissipation of $|1\rangle$ and $|2\rangle$, respectively. The $f_1$ and $f_2$ are harmonic force of oscillator $|1\rangle$ and $|2\rangle$, respectively. The steadystate solutions for the displacement of the oscillators are also harmonic: $x_1 = x_{10}e^{-i\omega t}$ , $x_2 = x_{20}e^{-i\omega t}$ , and corresponding amplitudes are given by

$$x_{10} = \frac{A_2\Omega^2 + f_1(\omega_2^2 - \omega^2 - i\gamma_2\omega)}{(\omega_1^2 - \omega^2 - i\gamma_1\omega)(\omega_2^2 - \omega^2 - i\gamma_2\omega) - \Omega^4}, \tag{3.1.3}$$

$$x_{20} = \frac{A_1\Omega^2 + f_2(\omega_1^2 - \omega^2 - i\gamma_1\omega)}{(\omega_1^2 - \omega^2 - i\gamma_1\omega)(\omega_2^2 - \omega^2 - i\gamma_2\omega) - \Omega^4}. \tag{3.1.4}$$

The paradigm of the classical analog of FR is that light excites only the broad mode (bright mode), e.g. $x_1$, while the narrow resonance mode $x_2$ (dark mode) is excited just due to the coupling. In this sense, only one oscillator is taken to be driven by a harmonic force where $f_2 = 0$. An example of this understanding can be seen in Fig. 3.1. But it can be examined simply that both modes can be excited directly, i. e. light equally excites both broad and narrow modes. In this case, the Fano line shape appears even when one has not any dark mode. The plots in Fig. 3.1 b indicate that when both oscillators are driven by harmonic forces, the resonance sharpness can be even higher. One of the simplest examples is a harmonic oscillator

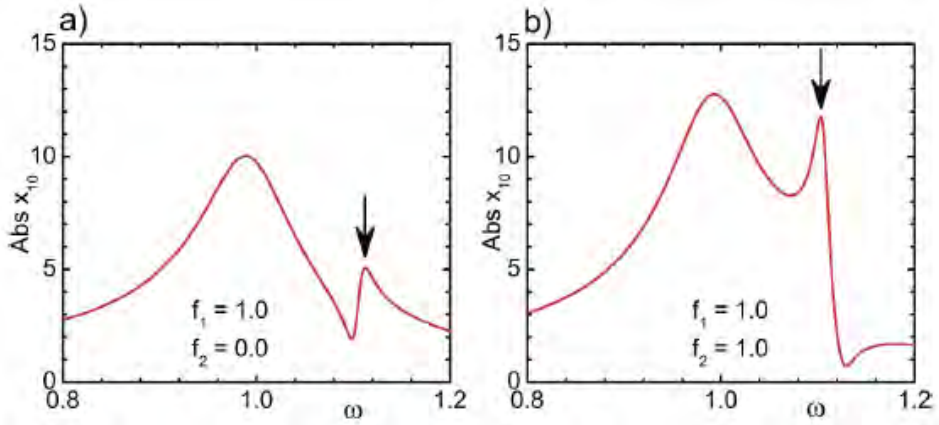


**Figure 3.1:** Amplitudes of resonances of coupling oscillators with $\omega_1 = 1$; $\omega_2 = 1.1$; $\Omega = 0.25$; $\gamma_1 = 0.1$; $\gamma_2 = 0.01$; $f_1 = 1$. The only difference is $f_2 = 0$ in case (a) and $f_2 = 1$ in case (b) [31].

.

with periodic forcing. When the frequency of the driving force is close to the eigenfrequency of the oscillator, the amplitude of the latter is growing towards

its maximal value. Often many physical systems may also exhibit the opposite phenomenon, when their response is suppressed if some resonance condition is met (which lead even to the term anti-resonance). This can be illustrated by using two weakly coupled underdapmed harmonic oscillators, where one of them is driven by a periodic force [see Fig. 3.2]. In such a system, in general, there are two resonances located close to eigen-frequencies $\omega_1$ and $\omega_2$ of the oscillators (Joe et al., 2006, [23]). One of the resonances of the forced oscillator demonstrates the standard enhancement of the amplitude near its eigenfrequency $\omega_1$, while the other resonance exhibits an unusual sharp suppression of the amplitude near the eigenfrequency of the second oscillator $\omega_2$ [see Fig. 3.2, (b) and (c)]. The first resonance is characterized by a symmetric profile, described by Lorentzian function, and known as a Breit-Wigner resonance (Breit and Wigner, 1936). The second resonance is characterized by an asymmetric profile. The second resonance was described for the first time by Fano (1935, 1961), when being attracted by unusual sharp peaks in the absorption spectra of noble gases observed by Beutler (1935) [45]. The nature of the asymmetry was established with the theory of configuration by Fano (1961) [74, 75]. The photoionization of an atom can go along various ways in terms of quantum analogy. The firs case is, the excitation of the inner-shell electron above the ionization threshold $A + \hbar\nu \longrightarrow A^+ + e$. Another possibility is to excite the atom into some quasi-discrete level, which can spontaneously ionize by ejecting an electron into the continuum $A + \hbar\nu \longrightarrow A^* \longrightarrow A^+ + e$. Such levels were named autoionizing, the autoionized state is a bound state of an atom with the energy above the first ionizing threshold. Autoionization is one of the most fundamental electron-electron correlation phenomena, and it is forbidden in the noninteracting particle approximation [46]. One of the possible autoionized states is the excitation of two electrons by one photon, when the excitation energies of each electron are of the same order of magnitude, and the total excitation energy exceeds the atom ionization threshold. The interaction between electrons leads to the decay of this state when one electron transfers into a

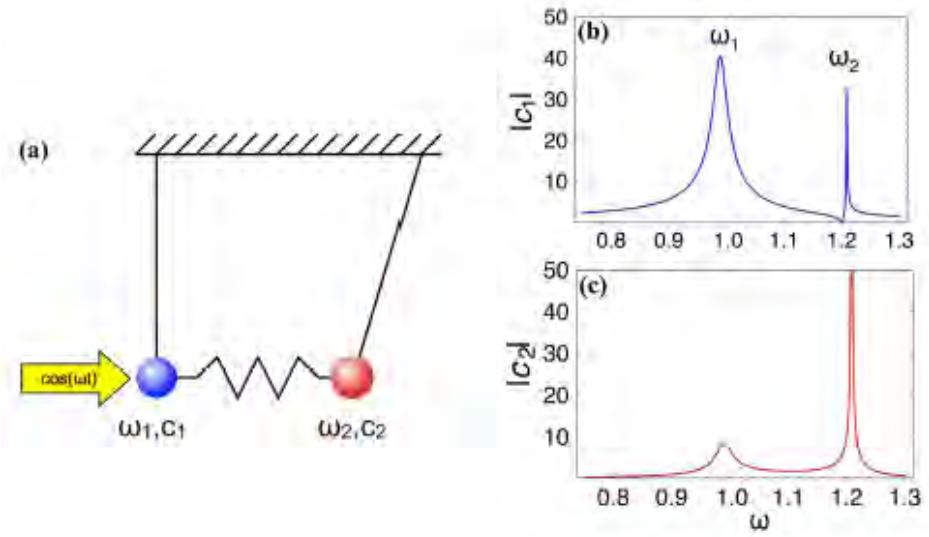


**Figure 3.2:** Resonances of parametrically driven coupled oscillators. (a) Schematic view of two coupled damped oscillators with a driving force applied to one of them; (b) the resonant dependence of the amplitude of the forced oscillator $|c_1|$, and (c) the coupled one $|c_2|$. There are two resonances in the system. The forced oscillator exhibits resonances with symmetric and asymmetric profiles near the eigenfrequencies $\omega_1 = 1$ and $\omega_2 = 1.2$ (b), respectively. The second coupled oscillator responds only with symmetric resonant profiles (c). Adapted from Joe et al. (2006) [23, 45].

.

lower state, and the second electron is ejected into the continuum, using the energy of the relaxed electron which is known as the Auger effect. This process is shown in Fig. 3.3. In general, autoionization can be considered as a mechanism which couples bound states of one channel with continuum states of another. Due to the superposition principle of quantum mechanics, whenever two states are coupled by different paths, interference may occur, it is such interference which we call Fano resonance. Fano used a perturbation approach to explain the appearance of asymmetric resonances. He considered a so-called prediagonalised state by putting the coupling between a discrete bound state, which is degenerate in energy with a continuum of states, to zero(see Fig. 3.4). Such a prediagonalized state may or may not have a clear physical analogy, but serves in any case as a convenient mathematical construction, which allows to solve the problem. As a result Fano

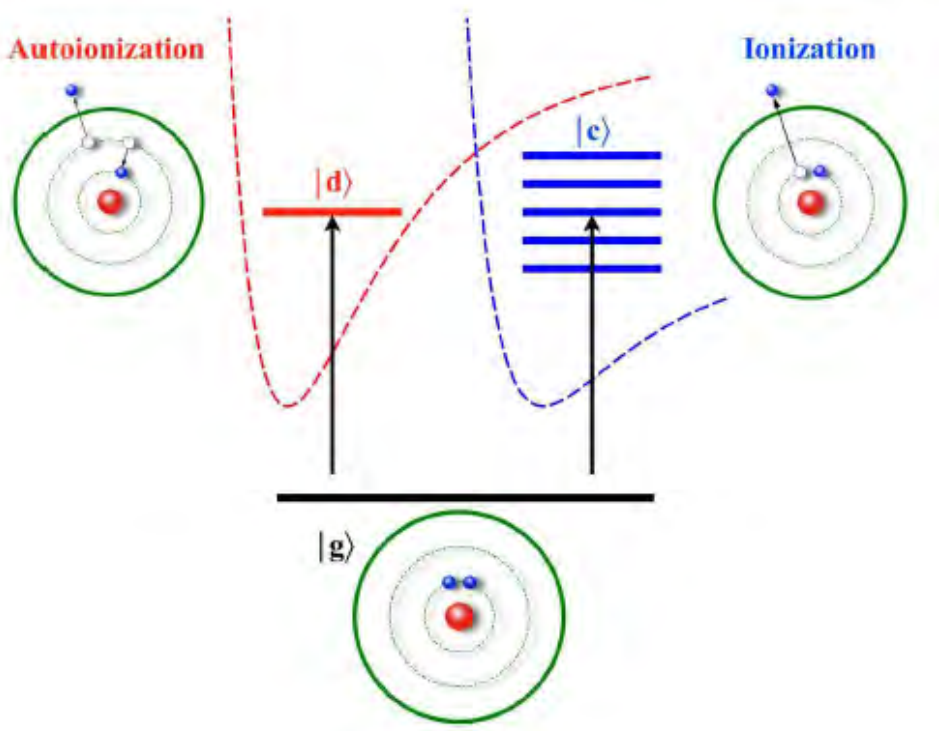


**Figure 3.3:** Fano resonance as a quantum interference of two processes direct ionization of a deep inner-shell electron and autoionization of two excited electrons followed by the Auger effect. This process can be represented as a transition from the ground state of an atom $|g\rangle$ either to a discrete excited autoionizing state $|d\rangle$ or to a continuum $|c\rangle$. Dashed lines indicate double excitations and ionization potentials. Adapted from Miroshnichenko et al. [45].

.

obtained the formula for the shape of the resonance profile of a scattering cross-section [45]:

$$\sigma = \frac{(\epsilon + q)^2}{\epsilon^2 + 1} \tag{3.1.5}$$

using the asymmetric parameter $q$ and a reduced energy defined by $\epsilon = \frac{2(E-E_F)}{\Gamma}$ $E_F$ is a resonant energy, and $\Gamma$ is the width of the auto-ionized state. From Eq. 3.1.5 there are exactly one maximum and one minimum in the Fano profile which is given by: $\sigma_{min} = 0$, at $\epsilon = -q$, $\sigma_{max} = 1 + q^2$, at $\epsilon = \frac{1}{q}$.

In his original paper Fano (1961) [74] has introduced the asymmetry parameter q as a ratio of transition probabilities to the mixed state and to the continuum. In the limit $|q| \longrightarrow \infty$ the transition to the continuum is very weak, and the lineshape is entirely determined by the transition through the discrete state only with the standard Lorentzian profile of a Breit-Wigner resonance. When the asymmetry

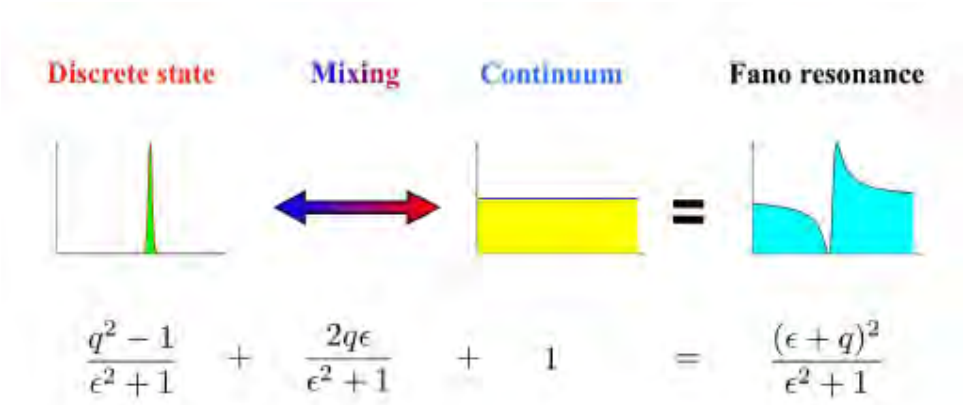


**Figure 3.4:** Illustration of the Fano formula as a superposition of the Lorentzian lineshape of the discrete level with a flat continuous background.

.

parameter q is order of unity both the continuum and discrete transition are of the same strength resulting is the asymmetric profile shown in Eq. 3.1.5, with the maximum value at $E_{max} = E_F + \frac{\Gamma}{2q}$ and minimum value at $E_{min} = E_F - \frac{\Gamma q}{2}$. The case of zero asymmetry parameter $q = 0$ is very unique to the Fano resonance and describes a symmetrical dip, sometimes called an anti-resonance as shown in Fig. 3.5. Generally, the main feature of the Fano resonance is the possibility of destructive interference, leading to asymmetric line shapes. As it can be depicted from Fig. 3.5, the actual resonant frequency of the discrete level $E_F$ may lie somewhere between the maximum and the minimum of the asymmetric profile, and the parameter q defines the relative deviation. In the situation $|q| \longrightarrow \infty$ the resonant frequency coincides to the maximum of the profile, while in the case $q = 0$ the resonant frequency coincides to the minimum where as for $q = 1$ it is located exactly at half distance between the minimum and maximum.

In this thesis, we studied the Fano-like resonance which can be realized in composites having dielectric-core metal-shell. We have derived an analytical expression for the polarization of individual metal shell spherical and cylindrical inclusions embedded in active host medium. Under Rayleigh frame work, it is demonstrated that modeling the dielectric function of the dispersive core for both

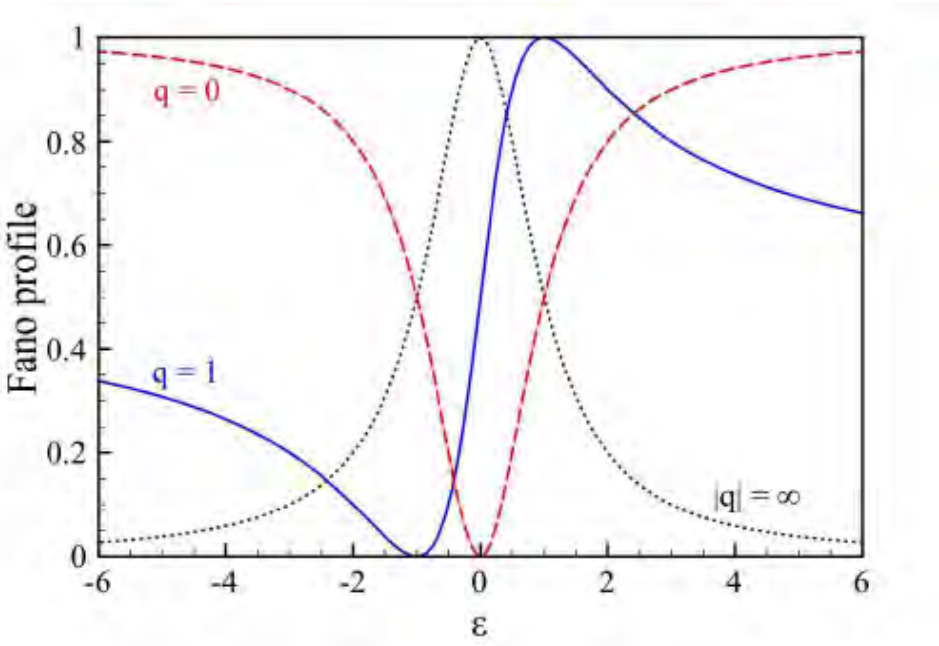


**Figure 3.5:** Normalized Fano profiles with the prefactor $\frac{1}{(1+q^2)}$ for various values of the asymmetry parameter q.

.

frequency dependent (the scattering cross-section) and frequency independent dielectric function of the core, pronounced Fano resonance can be achieved. The idea is introducing active host matrices having negative value of dielectric permitivity and assuming the electromagnetic responses of the composites can be regarded as electric dipoles only. In addition, Fano resonance can be tuned using variables like volume fraction (p), filling fraction (f), permitivity of host medium $\varepsilon_h$ and geometrical shape of the composite under the study, in our study cylindrical and spherical inclusions are considered separately. There are various assumptions on the origin of Fano-resonance from such composites. For instance, plasmonic hybridization model [76, 77] indicates, such symmetric core-shell structure can support an anti-bonding mode with a weak intensity, which can strongly couple to the broadband dipole mode of the metallic shell. To achieve Fano resonances at multiple frequencies, multiple dark modes are usually required, which can simultaneously interfere with a broadband bright mode. One strategy is to use multi-layer core-shell structure, where a number of dark modes are introduced by the hybridization between different layers though it is difficult for fabrication. However, here we propose to

use single layer of core-shell structure for the generation of Fano resonances as the higher-order modes are the result of the geometrical symmetry breaking, we confine ourself to dipolar approximation to predict the origin of Fano resonance in the proposed structure.

# Chapter 4

# Fabrication and Characterization Techniques of ZnO nanostructures

## 4.1 Growth Mechanism of ZnO Nanostructures

Zinc oxide (ZnO), a wide band gap (3.4 eV) II-VI compound semiconductor, has a stable wurtzite structure with lattice spacing a = 0.325 nm and c = 0.521 nm. It has attracted intensive research effort for its unique properties and versatile applications in transparent electronics, ultraviolet (UV) light emitters, piezoelectric devices, chemical sensors and spintronics. It is well documented that the shape and size of the material strongly affect the properties and the applications of the materials. Hence much effort is dedicated on controlling the size and shape of the particles by varying different growth parameters such as time, temperature, concentration, precursors, capping molecule, solvents, and others [78, 79, 80, 81]. Growth temperature and precursors are the key to control the morphology, optical, magnetic and electrical properties of ZnO nanostructures. Several techniques have been reported for the fabrication of ZnO, which can be broadly classified as gas-phase and aqueous solution-based methods. Gas-phase methods include vapour-phase transport, pulsed laser deposition (PLD), metal-organic chemical vapour deposition (MOCVD) and molecular beam epitaxy (MBE). The methods are very effective; however, they involve complex processes and require sophisticated equipment and high temperatures. In comparison, an aqueous solution-based method

like chemical bath deposition (CBD), hydrothermal growth and sol-gel methods are preferable as they requires no catalyst and economical. Among the aqueous solution-based methods, CBD is commercially feasible for large-scale production with good uniformity and can be carried out at significantly lower temperatures. Significant efforts in the last few years have been aimed at controlling the growth of one dimensional (1D) ZnO nanostructures using this method. However, in order to fully realize 1D ZnO-based devices, optimized growth methods and material processing techniques must be developed [82, 83, 84]. Growth conditions for ZnO nanostructures on Si substrate that have already been reported by other workers [85, 86, 87] were further optimized and studied in detail. The morphological, structural, optical and magnetic properties of nanostructures grown with various source-precursors have been studied. Among the 1D nanostructure, ZnO nanorod is one of the most important nano-materials for nanotechnology today [88, 89, 90, 91, 92, 93]. The ZnO samples used in the present study are synthesized using sol-gel and CBD method.

### 4.1.1 Sol-Gel Method

The sol-gel technique [94] is a wet chemical technique used in the fabrication of metal oxides from a chemical solution, and this acts as a precursor for an integrated network (gel) of discrete particles. The precursor solution can be either deposited on the substrate to form a film, cast into a suitable container with the desired shape, or used to synthesize powders. ZnO nanopowders produced by the sol-gel method is the subject of much interest, in view of the simplicity, low cost, reliability, repeatability and relatively mild conditions of synthesis, which are such as to enable the surface modification of zinc oxide with selected organic compounds. The prepared ZnO sample has a hexagonal wurtzite structure with the particles of a spherically shaped. A surface area obtained by the BET method of the calcined ZnO powder is equal to 10 $m^2/g$, characteristic of a material with low prosity, or a crystallized material. A solution of tetramethylammonium

hydroxide (TMAH) was added to a solution of zinc 2-ethylhexanoate (ZEH) in propan-2-ol. The resulting colloidal suspension was left for 30 min (alternatively for 24 h), and was then washed with ethanol and water.

### 4.1.2 Chemical bath deposition (CBD)

CBD is a technique that produces a solid film on a substrate during a single immersion through the control of the kinetics of formation of the solid [95]. It is the aqueous analogue of chemical vapour deposition (CVD), since both processes involve the mass transport of reactants, chemical reaction, nucleation, desorption, and growth. CBD is particularly suitable since it does not require high-pressure containers and is also entirely recyclable, safe and environmentally friendly, because only water or alcohols is used as a solvent. The safety hazards of organic solvents and their eventual evaporation and potential toxicity are avoided using this method. In addition, because no organic solvents or surfactants are present, the purity of the materials is substantially improved. Nanostructures produced using this method is self-assembled without any external manipulation. The by-products (residual salts) are easily washed out by water due to their high solubility. Despite the experimental simplicity, it is a complicated task to understand the mechanisms involved in the deposition process. The overall approach involves several steps, beginning with dissociation in solution and thermal treatment for the desired crystal growth [96]. During each step, a variety of parameters must be controlled. These include the concentrations of the precursors, the molar ratio of the metal to the base precursors, pH of the solution, growth time, growth temperature and the like. In principle, CBD can be used to deposit any compound that satisfies the following two basic requirements: Firstly, the source of cations (metal) and anions (hydroxide) must dissolve preferably in water (or alcohol) and must form a crystal; and secondly, the formed crystal must be insoluble and chemically stable in the solvent used. The crystal formed can grow either by homogeneous nucleation in solution and/or by hetero-nucleation on a substrate. Homogeneous

nucleation can occur due to local fluctuations in the solution concentration, temperature, or other variables. The first stage of the growth is collision between individual ions or molecules to form embryos. These embryos grow by collecting individual species that collide with them. In this type of growth, adsorption of ions on the embryo is expected to be the most probable growth mechanism. If the concentration of embryos in the solution is large, collisions between embryos can also play an important role. Heterogeneous nucleation may take place as a result of two distinct mechanisms. The first one is a growth mechanism involving the reaction of atomic species at the surface of stable nuclei pre-coated onto the substrate or impurities on it [90]. The second deposition mechanism is associated with the oriented attachment (for polar crystals) of particles formed by homogeneous nucleation on the wetting/seed layer pre-coated onto the substrate [97, 98]. It can be considered a cluster-by-cluster growth. Whatever mechanism dominates, the general steps in such solution growth are expected to be: generation of growth species, diffusion from the bulk to the growth surface, adsorption and surface growth.

In order to maintain low supersaturation levels during the growth process, the nutrient supply has to be finely controlled [99]. In most cases, no additional heat or chemical treatment is necessary, which represents a significant improvement compared with surfactant, template, or membrane based synthesis methods. This method is thus an increasingly important complement to other solution-based techniques in the fabrication of nanostructures. The formation of larger nuclei, which leads to precipitation, when the objective is to grow on pre-seeded substrates, is a waste of reagents. One common technique is the use of seeding layers to facilitate heterogeneous nucleation. Moreover, seeding of the substrate with nanoparticles lowers the thermodynamic barrier by providing nucleation sites, and hence improves the aspect ratios and optical properties, and ensures uniformity in the growth of ZnO nanostructures [100, 101]. This implies that any factor that

will improve the seed layer will improve the as-synthesized nanostructures. In addition to supersaturation, the other main parameters that affect these nucleation processes are pH and temperature. Temperature in particular is an important thermodynamic factor and plays a key role in controlling crystal growth rate. Higher temperatures enhance the kinetic energy of the precursors and this favours homogeneous nucleation in the solution.

## 4.2 Characterization techniques

Different characterization techniques were used to investigate on the structural, optical and magnetic properties of the sample under the study. Scanning Electron Microscopy, Energy Dispersive X-ray spectroscopy, powder X-ray Diffractometer, Photoluminescence Spectroscopy, Electron Paramagnetic Resonance, Raman Spectroscopy, UV-Visible Spectroscopy, and Fourier Transform Infrared Spectroscopy were used for analyzing the dopants, defects and overall underlying mechanism. A brief introduction was given for each characterization techniques used in the following sections.

### 4.2.1 X-ray Diffraction (XRD)

XRD is a versatile, non-destructive technique used for qualitative and quantitative analysis of a crystalline materials. In particular, XRD analysis can provide the crystalline quality and dominant crystallographic planes of the given material. In addition, the diffraction spectrum also provides information regarding the types of phases present in the material and can be used to calculate the approximate average grain size using Scherrers equation [105]. X-rays are short-wavelength, high energy electromagnetic radiation, having the properties of both waves and particles. They are produced whenever high energy electrons strike with metal target. Tubes in x-rays contain two electrodes an anode (the metal target) usually maintained, at ground potential, and a cathode maintained, at negative potential,

normally of order of 30KV to 50KV for the diffraction work. Interaction that occur between the beam (i.e. electrons) and target will result in a loss of energy. A continuous spectrum is formed when the high energy electrons are slowed down rapidly by multiple collisions with the anode material, which give rise to white radiation, or Bremsstrahlung. But not every electron decelerates in the same way, some stop in one impact and release all their energy at once, while others deflect this way and that way when they encounter atoms of the target, successively losing fractions of their total kinetic energy until is all spent. Those electrons which are stopped in one impact produce photons of maximum energy (wavelength) equal to the energy loss.

The atoms in crystals interact with X-rays in such a way as to produce interference. The interaction can be thought of as if the atoms in a crystal structure reflect the waves. But, because a crystal structure consists of an orderly arrangement of atoms, the reflections occur from the atomic planes. Let us consider a beam of monochromatic X-rays entering a crystal with one of its planes oriented at an angle of $\theta$ to the incoming beam to describe the phenomenon. Fig. 4.1 shows two such X-rays, where the spacing between the atomic planes occurs over the distance, d. Ray A reflects off of the upper atomic plane at an angle $\theta$ equal

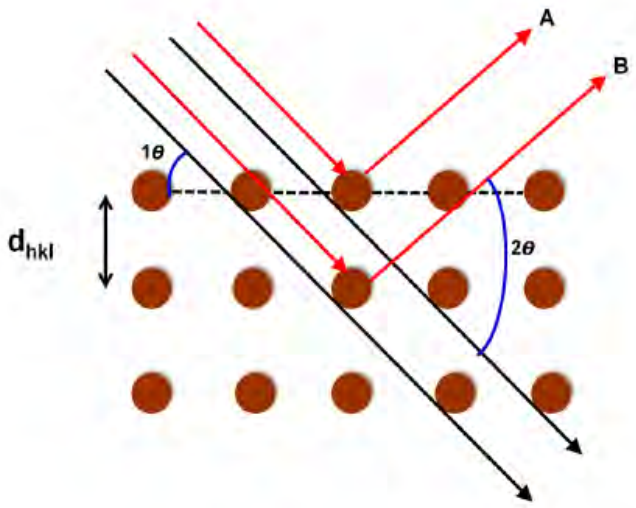


**Figure 4.1:** Monochromatic X-rays entering a crystal

to its angle of incidence. Similarly, Ray B reflects off the lower atomic plane at

the same angle $\theta$. While Ray B is in the crystal, however, it travels a distance of $2a$ farther than Ray A. If this distance $2a$ is equal to an integral number of wavelengths ($n\lambda$), then Rays A and B will be in phase on their exit from the crystal and constructive interference will occur. If the distance $2a$ is not an integral number of wavelengths, then destructive interference will occur and the waves will not be as strong as when they entered the crystal. Thus, the condition for constructive interference to occur is $(n\lambda) = 2a$. But, from trigonometry, one can figure out the distance $2a$ is in terms of the spacing, d, between the atomic planes, $a = d\sin\theta$ thus $2a$ reads, $2a = 2d\sin\theta$. From the relation, one can reach on the formulation of Bragg's Law for X-ray diffraction, which is the basic working principle of X-ray diffraction. It is indicative of knowing the wavelength of the X-rays going in to the crystal, one can measure the angle $\theta$ of the diffracted X-rays coming out of the crystal, then we know the spacing (referred to as d-spacing) between the atomic planes. A Philips PW 1840 powder and Bruker D8 (Bruker Corporation of Germany) diffraction system with a $CuK\alpha$ x-ray beam ($\lambda = 0.15405$) nm was used in the present study.

### 4.2.2 Scanning Electron Microscopy (SEM) and Energy Dispersive X-ray Spectroscopy (EDX)

Scanning electron microscopy is useful for the exploration of a diversity of specimens in various fields such as materials science, semiconductor research and microelectronics [106]. In the present study SEM has primarily been used for surface visualization of the ZnO samples. The surface morphology and elemental composition of the ZnO powders were investigated using a Shimadzu Superscan SSX-550 electron microscope equiped with an energy dispersive x-ray spectroscope (EDX). Like XRD, it is a non-destructive technique commonly used for surface analysis. It is capable of producing high resolution images, both planar and in cross-sectional views.

Electron microscopy takes advantage of the wave nature of rapidly moving electrons. In the microscope, a beam of electrons is generated in a vacuum. The beam is collimated by electromagnetic condenser lenses, focused by an objective lens, and then scanned across the surface of the sample by electromagnetic deflection coils. The primary imaging method is by collecting secondary electrons that are released by the sample. The electrons are detected by a scintillation material that produces flashes of light from the electrons. The light flashes are then detected and amplified by a photomultiplier tube. By correlating the sample scan position with the resulting signal, an image can be formed that is strikingly similar to what would be seen through an optical microscope. Beside the emitted electrons, x-rays are also produced by the interaction of electrons with the sample. These x-rays are characteristic of the elements present in the sample and can be detected in a scanning electron microscope coupled with an x-ray analyzer such as the energy dispersive x-ray spectrometer (EDX) [115]. The typical SEM equipment coupled with EDX: SHIMADZU Superscan model SSX-550 used in the study is shown in Fig. 4.2

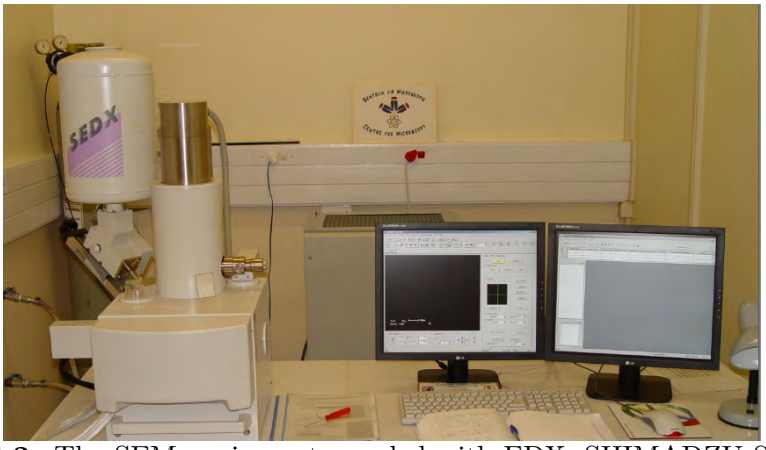


**Figure 4.2:** The SEM equipment coupled with EDX: SHIMADZU Superscan model SSX-550.

### 4.2.3 Photoluminescence Spectroscopy (PL)

PL is a process in which a substance absorbs photons and then re-radiates photons. PL is a non-destructive technique requiring no or little preparation of a sample.

Different types of samples (powder, liquid or bulk semiconducting material) can be characterized. PL measurements are usually performed using two different excitation conditions. Firstly, when excitation is with a continuous beam, the material can reach a steady state. The PL measured under these conditions, called continuous wave (CW) or steady state PL, provides information mainly on the position of the electronic levels participating in the radiative recombination processes. Secondly, when PL is excited using light pulses of suitable duration, time-resolved PL (TRPL) is obtained and the excited state lifetime, which provides information on carrier dynamics and recombination kinetics, can be extracted.

For CW-PL, the sample is excited by a laser with energy greater than its band gap and the luminescence intensity is measured as a function of wavelength or energy. The heart of this optical measurement system is a monochromator, which is used to differentiate between emissions at different photon energies, resulting in a plot of light intensity as a function of energy. Optical measurements provide information both about the host semiconductor, through intrinsic optical processes, and about the wide variety of impurities or defects which are endemic in all real semiconductor materials, through extrinsic optical processes. It is particularly suited for the detection of shallow-level impurities, but can also be applied to certain deep-level impurities/defects, provided that their recombination is radiative [107]. Fig. 4.3 depicts an experimental set-up for CW-PL measurements using photomultiplier tubes or semiconductor photodiodes. The luminescence is spectrally analyzed using a grating monochromator and, depending on the emitted photon energy, detected using either a photomultiplier tube or a photodiode. In this study, a PC controlled monochromator was used for wavelength tuning. The laser radiation was chopped by a mechanical chopper to allow signal amplification with a lock-in amplifier; alternatively, photon counting techniques may be used.

In this study, the PL characterization system employed were; a SPEX 18700.5 m spectrometer system, equipped with a He-Cd laser lamp as the excitation source

and a Cary Eclipse fluorescence spectrophotometer (Model: LS 55). Low temperature PL is used to obtain specific information about the centers which promote impurity related recombination, the donors and acceptors, and this can only be obtained when the carriers are frozen-out in these centres. There is also a dramatic reduction in the spectral broadening caused by the coupling of carriers with phonons, called vibronic processes, at low temperatures.

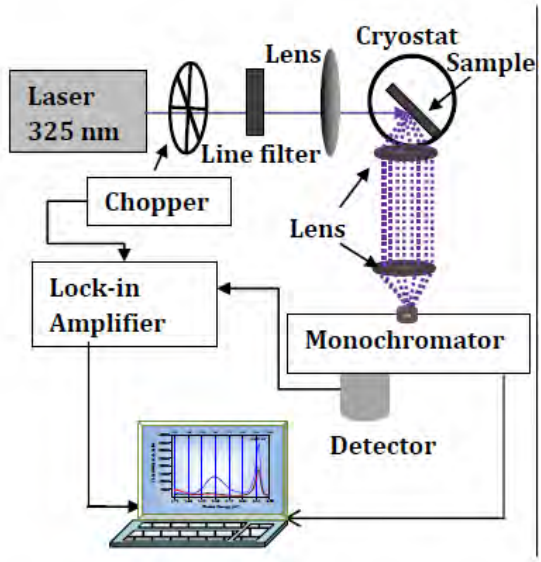


**Figure 4.3:** Schematic diagrams of typical experimental set-ups for CW-PL measurements using photomultiplier tubes or semiconductor photodiodes.

### 4.2.4 Electron Paramagnetic Resonance Spectroscopy (EPR)

ESR or electron spin resonance (ESR) spectroscopy is a method for studying materials with unpaired electrons. EPR is an effective tool to investigate the origin and nature of un-paired electrons in an atom [108, 109]. These un-paired electrons which are $10,000$ times lighter than atoms have their intrinsic spin contributing to some sort of magnetism. An isolated electron, all alone in space without any outside forces, still has an intrinsic angular momentum called spin. Because an electron is charged, the angular motion of this charged particle generates a magnetic field. In other words, the electron due to its charge and angular momentum, acts like a little bar magnet, or magnetic dipole, with a magnetic moment. The

energy differences studied in EPR spectroscopy are predominately due to the interaction of unpaired electrons in the sample with a magnetic field produced by a magnet in the laboratory. This effect is called the Zeeman Effect. The magnetic field, $B_0$, produces two energy levels for the magnetic moment, $\overline{\mu}$, of the electron. The unpaired electron will have a state of lowest energy when the moment of the electron is aligned with the magnetic field and a stage of highest energy when is aligned against the magnetic field. Firstly, the two spin states have the same energy in the absence of a magnetic field. Secondly, the energies of the spin states diverge linearly as the magnetic field increases. These two facts have important consequences for spectroscopy:

1) Without a magnetic field, there is no energy difference to measure.

2) The measured energy difference depends linearly on the magnetic field.

By using the above mechanism changing the energy differences between the two spin states by varying the magnetic field strength, we will have an alternative means to obtain spectra. We could apply a constant magnetic field and scan the frequency of the electromagnetic radiation as in conventional spectroscopy. Alternatively, we could keep the electromagnetic radiation frequency constant and scan the magnetic field. A peak in the absorption will occur when the magnetic field tunes to the two spin states so that their energy difference matches the energy of the radiation. This field is called the field of resonance. A radiation source for radar waves produces only a very limited spectral region. In EPR such a source is called a klystron. A so-called X-band klystron has a spectral band width of about $8.8 - 9.6$ GHz. This makes it impossible to continuously vary the wavelength similarly to optical spectroscopy. It is therefore necessary to vary the magnetic field, until the quantum of the radar waves fits between the field-induced energy levels. Once the sample is placed in a large uniform magnetic field which is shown in Fig. 4.4, splits the energy levels of the ground state by an amount where, $\Delta E = g\beta B_0 = h\nu$. Since $\beta$ is a constant, Bohr magneton, and the magnitude of $B_0$ can be measured, all we have to do is to calculate the spectroscopic g-factor, g, is

by determine the value of $\Delta E$, the energy between the two spin levels. This is done by irradiating the sample with microwaves with a set frequency and sweeping the magnetic field. In the present study, the microwave absorption measurements were

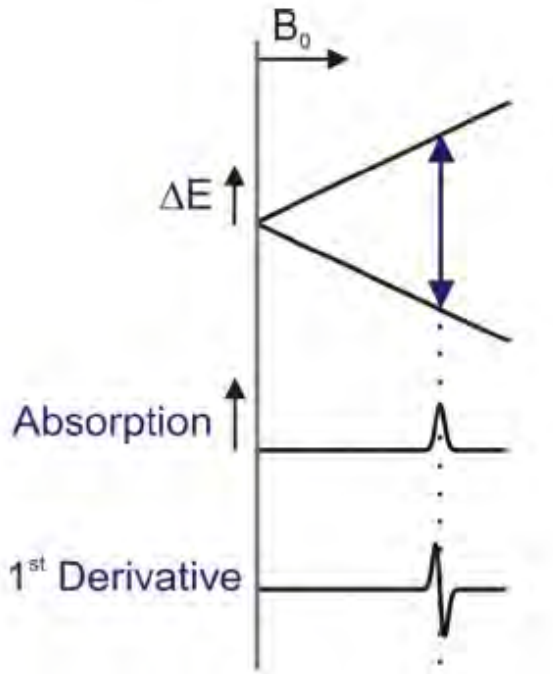


**Figure 4.4:** The schematic model of EPR experiment technique

carried out using a JEOL electron paramagnetic resonance (EPR) spectrometer operating at 9.4 GHz (x-band) at room temperature ($298K$).

### 4.2.5 Raman Spectroscopy

Raman scattering is an inelastic light scattering which allows the access mainly to the phonon modes at the $\Gamma$ point of materials and in some cases to the dispersion. Raman scattering is a versatile non-destructive technique for detecting the incorporation of dopant, the resulted defects and lattice dynamics of the host lattice [110]. It is the manifestation of the interaction between the electromagnetic radiation and vibrational or rotational motions in a material. It provides information about the symmetry and composition, the lattice dynamics, structural transitions, strain and electronic states. In Raman spectroscopy, sample is illuminated with monochromatic laser beam interacts with the molecules of sample and originates scattered light. Raman spectra arises due to inelastic collision between incident

monochromatic radiation and molecules of the samples. When monochromatic radiation strikes at sample, it scatters in all directions after its interaction with sample molecules. A change in polarizability during molecular vibration is an essential requirement to obtain Raman spectrum of sample. When the frequency of incident radiation is higher than frequency of the scattered radiation, Stokes line appear in Raman spectrum. But when the frequency of the incident radiation is lower than the scattered radiation anti-Stokes lines appear in Raman spectrum. Stokes shifted Raman bands involve the transition from lower to higher energy vibrational levels and therefore, Stokes bands are more intense than anti-Stokes bands and hence measured in conventional Raman spectroscopy. Room temperature Raman measurements were recorded to study the vibration modes in the un-doped and Al doped ZnO. In the present work, Raman spectroscopic measurements were collected using a Horiba Jobin-Yvon HR800 Raman microscope equipped with an Olympus BX-41 microscope attachment. An $Ar^+$ laser (514.5 nm) with energy setting 1.2 mW from a Coherent Innova Model 308 was used as an excitation source.

### 4.2.6 UV-Visible Spectroscopy (UV-Vis)

An instrument used in the ultraviolet-visible spectroscopy is called UV-Vis spectrophotometer. The wavelength of UV is shorter than the visible light. It ranges from 100 to 400 nm. In a standard UV-Vis spectrophotometer, a beam of light splits into two, one half of the beam (the sample beam) is directed through a transparent cell containing a solution of the compound being analysed, and the other half (the reference beam) is directed through an identical cell that does not contain the compound but contains the solvent. The instrument is designed so that it can make a comparison of the intensities of the two beams as it scans over the desired region of the wavelengths. If the compound absorbs light at a particular wavelength, the intensity of the sample beam (IS) will be less than that

of the reference beam. Absorption of radiation by a sample is measured at various wavelengths and plotted by a recorder to give the spectrum which is a plot of the wavelength of the entire region versus the absorption (A) of light at each wavelength, to calculate the band gap of the samples. The Varian Cary 100 Conc. UV-Vis spectrophotometer was used in this study.

### 4.2.7 Fourier Transform Infrared Spectroscopy (FTIR)

The energy of most molecular vibrations corresponds to the infrared region of the electromagnetic spectrum. The detection of these vibrations is mainly measured in an infrared (IR), which typically covers a wavelength range of $2 - 16\ \mu m$ (commonly expressed as $400 - 5000\ cm^{-1}$). The IR spectrometer system consists of an IR source emitting throughout the whole frequency range. While the source is emitting throughout, the beam is split, with one beam passing through the sample (transmission) or reflected (for studies of surfaces) while the other beam is employed as a reference beam. The prepared ZnO sample was then loaded into FTIR which normally works by allowing transmitted (or reflected) beam to recombine with the reference beam after a path difference has been introduced. The interference pattern generated is Fourier transformed to produce the spectrum of material being analyzed as a function of wavelength or wavenumber of the incident radiation. Lastly, if the molecular vibration is excited in the sample, the molecule absorbs energy of the particular frequency and this is detected as absorption relative to the reference beam. Furthermore, different functional groups have characteristic vibration frequency arising due to stretching, bending, rocking and twisting of bonds which allows the particular functional group to be identified.

# Chapter 5

# Fano-Like Resonances in Dielectric/Metal Core/Shell Nanostructures

## 5.1 Introduction

The study of light scattering by different systems gives important information about their structure [3, 53]. Interaction of light with nanocomposites reveals novel optical phenomena indicating unrivalled optical properties of these materials [56, 57]. It is quite natural to consider metal coating as a potential possibility, since metal is known to be the best in terms of confining electromagnetic waves, especially near the surface-plasmon polariton (SPP) resonance [58]. One of the new possibilities to be explored is the use of dielectric nano particles with strong electric field response for a new type of resonant interactions at the nanoscale. One type of such interactions is associated with Fano resonances, widely studied in many branches of physics including nanophotonics [45, 46]. In particular, Fano resonances were successfully observed experimentally in many plasmonic nanostructures. An attractive generality of the physics of Fano resonances comes from its interference origin observed in many wave scattering processes. One of the necessary conditions for the Fano resonance to occur is the coexistence of at least two scattering channels, one of them being a resonant one [50]. Nowadays, nanocomposites attract attention as media with predefined optical properties required for different applications. The design and study of optical properties of

nanocomposites is an important problem of contemporary material science. Due to the practical necessities, nanocomposites are often made as thin films and have optical properties which are different from the properties of bulk objects made from the same material. The main reason for these differences consists in the presence of a strongly inhomogeneous local field at the interfaces and the inclusions made in the composites [21]. These interface effects, for example, are the reason for depolarization phenomena and other optical responses [24]. There are numerous works where the optical properties of small particles or systems of small particles were studied [59]. Being originated in the pioneer paper by Fano [74], the Fano resonances have become one of the most appealing phenomena in the wave scattering.

Former literatures predict Fano-like resonances due to light scattering by small spatially homogeneous particles as interference of two dipole modes: the off-resonant Rayleigh effects and the resonant which is excited at a large value of the particles' dielectric permittivity [111]. The properties of a composite material are related to the properties and fractions of the constituents. Therefore, the electromagnetic properties of composites can be tailored by varying the properties and fractions of the constituents (inclusions) as presented in ref. [112]. We assume that the inclusions are not too densely packed; according to the Clausius-Mossotti approximation, only dipolar interaction between the inclusions should be taken into account.

The model and formulation of the problem presented in this Chapter aims to investigate and have a solid understanding of the unusual optical properties of dielectric/metal coreshell composites and presents different approach to study Fano-like resonant effect which is not discussed in the literatures, so far. It is well known that the plasmon resonance of metal nanoparticles is strongly sensitive to the nanoparticle size, shape, and the dielectric properties of the surrounding medium [19, 29]. For the study of the optical properties of a composite system

with an inhomogeneity scale much smaller than the wavelength of interest, electrodynamic quantities of each constituent particles is overshadowed by the average response of the whole system. Therefore, the method employed in the study is one of the qualitative effective medium theory approach embedding the inclusions in active host medium [61]. The result could be useful for potential applications in terms of exploring the intriguing interplay between Fano resonances and the generation of mixed composites with nanostructures, and in designing new materials for selective solar cell absorbers.

## 5.2 Theoretical Model

Consider individual metal spherical or cylindrical inclusion with a dielectric core embedded in a dielectric host matrix (see Fig. 5.1). Let $r_1$ and $r_2$ be the radii of the dielectric core and the metal cover, respectively, for both spherical and cylindrical geometries with $r_1 < r_2$. The dielectric functions (DFs) of the core, metal cover, and host matrix are denoted as $\varepsilon_1$, $\varepsilon_2$, and $\varepsilon_h$, respectively. In the electrostatic approximation, i.e., when the wavelength of the incident electromagnetic wave is much greater than the typical size of the inclusion, the distribution of the electric potential in an external constant electric field in the system is described by the following expressions:

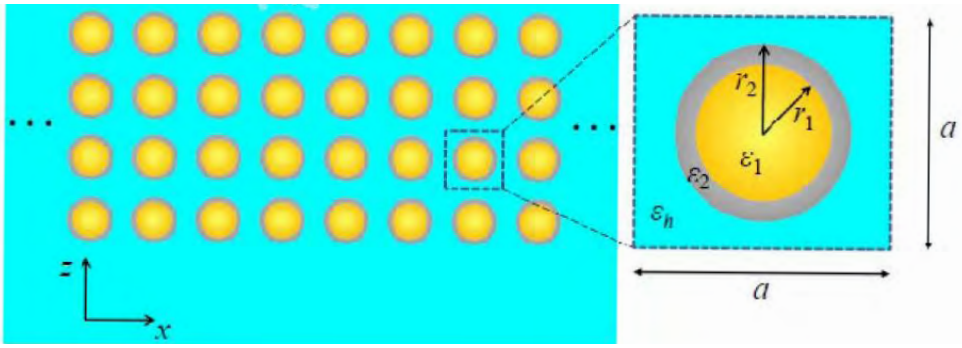


**Figure 5.1:** Model of nanocomposite core-shell consisting of a matrix in which coated spherical particles are embedded in active host matrices.

.

$$\phi_1 = -E_h A r \cos\theta, \qquad r \leq r_1 \tag{5.2.1}$$

$$\phi_2 = -E_h\Big(Br - \frac{C}{r^2}\Big)\cos\theta, \qquad r_1 \le r \le r_2 \tag{5.2.2}$$

$$\phi_h = -E_h\Big(r - \frac{D}{r^2}\Big)\cos\theta, \qquad r \ge r_2 \tag{5.2.3}$$

where $\phi_1$, $\phi_2$, and $\phi_h$ are potentials in the dielectric core, metal, and the host matrix, respectively, $E_h$ is the magnitude of the applied electric field, $r$ and $\theta$ are the spherical coordinates of the observation point with the $z$-axis chosen to be along the vector $\vec{E}_h$). The parameters $A$, $B$, $C$ and $D$ are unknown coefficients, which can be obtained from the continuity conditions of the potential and the displacement vector at the boundaries of the dielectric core-metal and metal-host matrix. Further, only coefficients $D_n \equiv D$ and $A_n \equiv A$ that enter into the potential of the local field in the inclusion core and the induced dipole moment of the inclusion are needed. Let us write electric potential for host medium for spherical or cylindrical inclusions as

$$\phi_h = -E_h\Big(r - \frac{D_n}{r^{n-1}}\Big)\cos\theta, \qquad r \ge r_2. \tag{5.2.4}$$

where $E_h$ is the magnitude of the applied field (for the cylinder it is perpendicular to its axis) and $n$ is the dimension of the problem, i.e., $n = 3$ for the spherical inclusion and $n = 2$ for the cylindrical inclusion, respectively. It is worth noting that the local field in these inclusions can be considerably enhanced if the frequency of the incident radiation is close to the surface plasmon frequency. The magnitude of the enhanced local field $\vec{E}$ in the dielectric core of the inclusion can be obtained with the help of the relation

$$E = AE_h,$$

where $A$ is an enhancement factor given by:

$$A = \frac{Q\varepsilon_2\varepsilon_h}{p\Delta},$$

with

$$Q = \frac{n^2}{n-1},$$

and $p$ is the volume fraction of the metal coated. The value of the metal fraction for spherical inclusions is given by

$$p = 1 - \Big(\frac{r_1}{r_2}\Big)^3,$$

whereas for cylindrical inclusions it takes the form:

$$p = 1 - \Big(\frac{r_1}{r_2}\Big)^2.$$

Moreover, the effective polarizability of the coated sphere or cylinder can be written as:

$$D_n = \Big\{1 - \frac{n}{n-1}\frac{\varepsilon_h[(n-p)\varepsilon_2 + p\varepsilon_1]}{p\Delta}\Big\} r_2^n, \tag{5.2.5}$$

where

$$\Delta = \varepsilon_2^2 + q\varepsilon_2 + \epsilon_1\varepsilon_h \tag{5.2.6}$$

with the parameter $q$ given by

$$q = \Big(\frac{3}{2p} - 1\Big)\varepsilon_1 + \Big(\frac{3}{p} - 1\Big)\varepsilon_h \tag{5.2.7}$$

for spherical inclusions and

$$q = \Big(\frac{2}{p} - 1\Big)\varepsilon_1 + \Big(\frac{2}{p} - 1\Big)\varepsilon_h \tag{5.2.8}$$

for cylindrical inclusions. In general, the dielectric permittivity of the host medium and the metal coated for sphere or (cylindrical) are complex quantities given by

$$\varepsilon_h = \varepsilon'_h + i\varepsilon''_h \tag{5.2.9}$$

$$\varepsilon_2 = \varepsilon'_2 + i\varepsilon''_2. \tag{5.2.10}$$

In addition, the real and imaginary parts of the dielectric permittivity of the metal cover have the Drude form. That is,

$$\varepsilon'_2 = \varepsilon_\infty - \frac{1}{z^2 + \gamma^2}, \tag{5.2.11}$$

and

$$\varepsilon''_2 = \frac{\gamma}{z(z^2 + \gamma^2)}, \tag{5.2.12}$$

where we introduced the notations $z = \omega/\omega_p$ and $\gamma = \nu/\omega_p$, $\omega$ is the frequency of the incident radiation, $\omega_p$ is the plasma frequency of the inclusion metal part, and $\nu$ is the electron collision frequency. Here, we would like to note that the polarizability of a two-layer spherical inclusion may be presented in the Ref. [121, 122] as:

$$\alpha = 4\pi r_2^3 \frac{\overline{\epsilon} - \varepsilon_h}{\overline{\epsilon} + 2\varepsilon_h}, \tag{5.2.13}$$

where $\alpha = \alpha' + i\alpha''$ is a complex quantity and $\overline{\epsilon}$ is the effective dielectric function of the individual two-layer inclusion in the dipole approximation and given by the relation [123]:

$$\overline{\epsilon} = \varepsilon_2 \frac{\varepsilon_1(\frac{3}{p} - 2) + 2\varepsilon_2}{\varepsilon_1 + \varepsilon_2(\frac{3}{p} - 1)}. \tag{5.2.14}$$

Combining Eq. 5.2.13 and Eq. 5.2.14, one may easily show that the enhancement factor ($A$) and the polarizability coefficient in Eq. 5.2.6 have the same denominator $\Delta$ in Eq. 5.2.7. This means that $\alpha$ increases considerably when the frequency $\omega$ approaches one of the eigen frequencies. At the same time, the absorption of radiation by a particle increases due to an increase in the polarization. To illustrate this, we calculated the real $\eta_1$ and imaginary part $\eta_2$ of the refractive index of composite $R = \eta_1 + i\eta_2$ of the spherical coated inclusions with different metal fraction, $p$. For small density numbers, $N$, of the inclusions it is possible to use the relation with no account of the Lorentz field [24-27]. Thus,

$$R^2 = \varepsilon_h + 4\pi N D. \tag{5.2.15}$$

The numerical calculations have been performed using the volume fraction ($f$) of inclusions in the composites which is defined by $f = (4\pi/3)Nr_2^3$ for different values of $f$. Here, we relate the resonant frequencies with the metal part of the inclusion and the two interfaces, i.e., the dielectric core-metal and the metal-host matrix interfaces. To observe the appearance of Fano-like resonances, the analytical and numerical results of the imaginary part of the polarization for spherical inclusions needs to be checked. However, in our analysis, the appearance of Fano resonances in composite with active media are demonstrated by considering the

active host matrices under imaginary part of the polarizability; for both spherical and cylindrical inclusions.

## 5.3 Numerical Results

### 5.3.1 Fano-like resonance in spherical inclusions

The equation that specifies the local field in the inclusion with account of the nonlinear part of the dielectric function of the core ($\varepsilon_1$) and their polarization can be obtained with the help of Clausius-Mossotti approximation. Following [124], the magnitude of the average Lorentz local field ($\vec{E}$) in the dielectric core of the inclusion is given by the following relation:

$$\vec{E} = \vec{E}_h + \frac{4\pi}{3}\vec{P}, \tag{5.3.1}$$

where the polarization of the system is given by $\vec{P} = ND\vec{E}$ and $N$ is a density number of the inclusions. The polarizability of the inclusion coincides with the coefficient $D$ given by Eq. 5.2.6. Therefore, we may use $D$ as the effective polarizability of the system to show Fano-like resonance in the composite for both cylindrical and spherical inclusions. Maxwell Garnett mixing formula for the composite for our case can be written as:

$$\varepsilon_{eff} = \varepsilon_h\Big(1 + \frac{2f\alpha}{1 - f\alpha}\Big),$$

where $\alpha$ is the polarizability of the spherical or cylindrical inclusion introduced in the next section. For nonmagnetic medium, i.e., $\mu = \mu_0$, the index of refraction $R$ can be expressed in terms of the effective dielectric constant as $R^2 = \varepsilon_{eff}$. Therefore, it is possible to determine the refractive index of the composite from the above expression as

$$R^2 = \varepsilon_h\Big(1 + \frac{2f\alpha}{1 - f\alpha}\Big).$$

The effective polarizability of an individual metal covered spherical nanoinclusion with a dielectric core embedded in a dielectric host matrix can be written as

follows:

$$D = \alpha r_2^3, \tag{5.3.2}$$

where

$$\alpha = 1 - \frac{3}{2}\frac{\delta}{\Delta}, \tag{5.3.3}$$

with $\Delta$ given by Eq. 5.2.6 and

$$\delta = \varepsilon_h\Big[\Big(\frac{3}{p} - 1\Big)\varepsilon_2 + \varepsilon_1\Big]. \tag{5.3.4}$$

Here $D$ is the effective polarizability of the inclusion, $p = 1 - (r_1/r_2)^3$ is the metal fraction in the inclusion. But $\varepsilon_1$ which is dielectric function of the core is independent of frequency and is a real constant value $\varepsilon_1 = 9$, for the current analysis. Moreover, all numerical calculations are carried out using the following parameters: $\varepsilon_h' = 2.25$, $\varepsilon_\infty = 4.5$, $\omega_p = 1.46 \times 10^{16}$ (silver plasma frequency), $\gamma = 1.15 \times 10^{-2}$, $\nu = 1.68 \times 10^{14}$, and this values are adapted from Ref. [125], whereas $\varepsilon_h''$ varies as shown on the graphs. From Eq. 5.2.13 $\alpha'$ and $\alpha''$, can be written as:

$$\alpha' = 1 - \frac{3}{2}\frac{\delta'\Delta' + \delta''\Delta''}{\Delta'^2 + \Delta''^2}, \tag{5.3.5}$$

and

$$\alpha'' = \frac{3}{2}\frac{\delta'\Delta'' - \delta''\Delta'}{\Delta'^2 + \Delta''^2}, \tag{5.3.6}$$

where

$$\delta' = \Big(\frac{3}{p} - 1\Big)[\varepsilon_2'\varepsilon_h' - \varepsilon_2''\varepsilon_h''] + \varepsilon_1\varepsilon_h', \tag{5.3.7}$$

$$\delta'' = \Big(\frac{3}{p} - 1\Big)[\varepsilon_2'\varepsilon_h'' + \varepsilon_2''\varepsilon_h'] + \varepsilon_1\varepsilon_h'', \tag{5.3.8}$$

$$\Delta' = {\varepsilon_2'}^2 + q'\varepsilon_2' + \varepsilon_1\varepsilon_h' - \varepsilon_2''^2 - q''\varepsilon_2'', \tag{5.3.9}$$

$$\Delta'' = (q' + 2\varepsilon_2')\varepsilon_2'' + \varepsilon_1\varepsilon_h'' + q''\varepsilon_1', \tag{5.3.10}$$

$$q' = \Big(\frac{3}{2p} - 1\Big)\varepsilon_1 + (\frac{3}{p} - 1)\varepsilon_h', \tag{5.3.11}$$

$$q'' = \Big(\frac{3}{p} - 1\Big)\varepsilon_h''. \tag{5.3.12}$$

It was demonstrated that the imaginary part of polarization shows Fano-like resonance at frequency $z = 0.4\omega_p$ (see Fig. 5.2) for $p = 0.85$. Comparison of the values

of $\varepsilon_h''$ at $-0.145$, $-0.15$, and $-0.16$, the numerical results show that $\varepsilon_h'' = -0.145$ and $\varepsilon_h'' = -0.15$ which manifest itself in a very narrow Fano-dip. However, at $\varepsilon_h'' = -0.16$, the effect disappears showing ordinary Lorentzian profile. We demon-

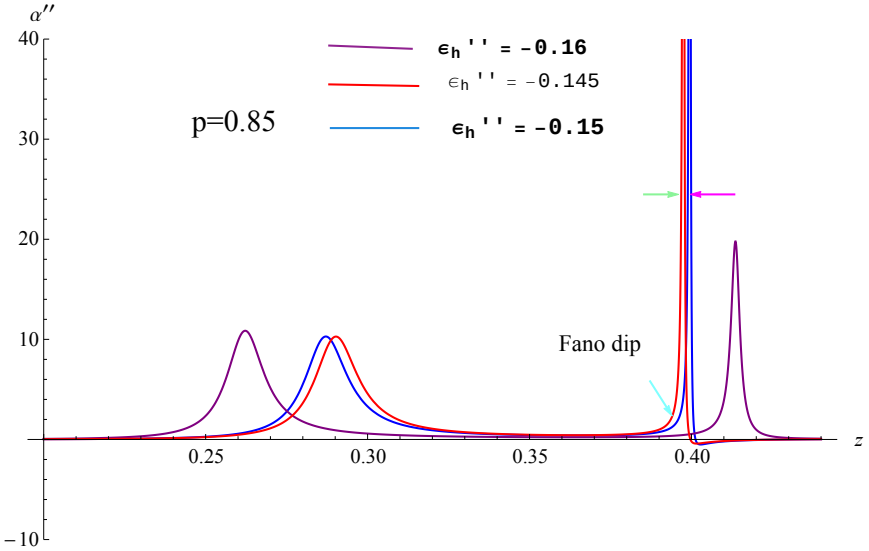


**Figure 5.2:** Imaginary part of polarization of spherical nanoinclusion obtained for different values of $\varepsilon_h''$ fixing the value of $p = 0.85$ and $\varepsilon_1 = 9$ where Fano-like resonance is observed at $z = 0.4\omega_p$ for $\varepsilon_h''$ values of 0.145 and 0.15 however for $\varepsilon_h'' = -0.16$ the second resonance shows symmetric profile.

strate that the real part of refractive index ($R^2$) has great impact on Fano-like region as shown in Fig. 5.3 for different values of $p$ at the particular values $\varepsilon_1 = 9$, $\varepsilon_h = -0.1386$, and $f = 0.0001$. We observed that the two has been Fano-like for all values of $p$ approximately around $z = 0.21\omega_p$ and $z = 0.43\omega_p$ which is confirmed by the analysis of the plot. A typical wavelength corresponding to the resonant frequency ($z_r$) $0.35\omega_p$ for inclusions with $p = 0.9$ is about 369.6 $nm$. Taking inclusions of having a radius of 20 $nm$ and using the relation $r_1 = r_2(1-p)^{1/n}$ that connect the radii of core and inclusion, we get that at $p = 0.9$, $r_1 = 2$ $nm$ and $r_2 = 0.06$ $nm$ for the spherical and cylindrical inclusion, respectively. In other words, the core can be treated as a quantum dot and in addition we can use the model to find the most suitable absorption region. For example, we can tune the value of $p$ to find the wavelength at infrared region for medical application [126]. It is known that quantum dots can be satisfactory described by the macroscopic dielectric permittivity.

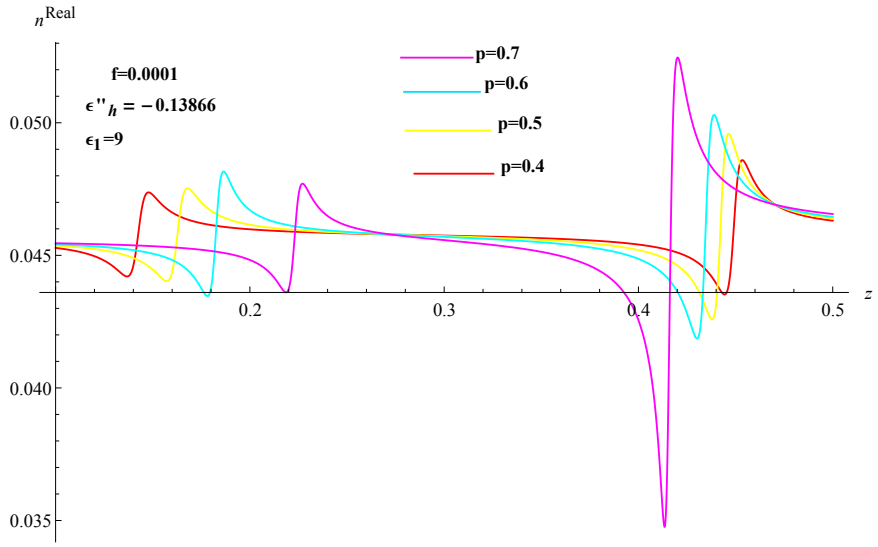


**Figure 5.3:** The real part of refractive index for different values of $p$ at particular value $\varepsilon_1 = 9$, $\varepsilon_h = -0.1386$ and $f = 0.0001$ we observe the two resonance to be Fano-like for all values of $p$ approximately around $z = 0.21\omega_p$ and $z = 0.43\omega_p$.

### 5.3.2 Fano-like resonance in cylindrical nanoinclusions

Let us consider an infinite circular cylinder of dielectric core of radius ($r_1$) coated with metal shell of radius ($r_2$). The core-shell system has optical material parameters $\varepsilon_1$ and $\varepsilon_2$, respectively, and it is embedded in the host matrices with electric permittivity $\varepsilon_h$, and the scatterer which is irradiated by plane wave. To show the appearance of Fano-like resonance in the system we employ the assumptions that the inclusions have radii much much less than the wavelength of light, the inclusions are homogeneous and nonmagnetic, and the external radius of cylindrical inclusions is much smaller than its length. For cylindrical inclusion we focus only on frequency independent dielectric function in the expression of imaginary part of polarization and the real part of refractive index; as shown in Fig. 5.4 and Fig. 5.5 (real value, $\varepsilon_1 = 9$) while keeping all other parameters the same as that of the spherical inclusions. The effective polarizability of an individual metal covered dielectric cylindrical nanoinclusion embedded in a dielectric host matrix can be presented by:

$$D = \alpha r_2^2, \tag{5.3.13}$$

where

$$\alpha = 1 - 2\frac{\delta}{\Delta}, \tag{5.3.14}$$

with $\Delta$ given by Eq. 5.2.7 and

$$\delta = \varepsilon_h\Big[\Big(\frac{2}{p} - 1\Big)\varepsilon_2 + \varepsilon_1\Big]. \tag{5.3.15}$$

Eq. 5.3.14 can be written separately as:

$$\alpha' = 1 - 2\frac{\delta'\Delta' + \delta''\Delta''}{\Delta'^2 + \Delta''^2}, \tag{5.3.16}$$

and

$$\alpha'' = 2\frac{\delta'\Delta'' - \delta''\Delta'}{\Delta'^2 + \Delta''^2}, \tag{5.3.17}$$

where

$$\delta' = \Big(\frac{2}{p} - 1\Big)[\varepsilon_2'\varepsilon_h' - \varepsilon_2''\varepsilon_h''] + \varepsilon_1\varepsilon_h', \tag{5.3.18}$$

$$\delta'' = \Big(\frac{2}{p} - 1\Big)[\varepsilon_2'\varepsilon_h'' + \varepsilon_2''\varepsilon_h'] + \varepsilon_1\varepsilon_h'', \tag{5.3.19}$$

$$\Delta' = \varepsilon_2'^{\,2} + q'\varepsilon_2' + \varepsilon_1\varepsilon_h' - \varepsilon_2''^2 - q''\varepsilon_2'', \tag{5.3.20}$$

$$\Delta'' = (q' + 2\varepsilon_2')\varepsilon_2'' + \varepsilon_1\varepsilon_h'' + q''\varepsilon_2', \tag{5.3.21}$$

$$q' = \Big(\frac{2}{p} - 1\Big)\varepsilon_1 + \Big(\frac{2}{p} - 1\Big)\varepsilon_h', \tag{5.3.22}$$

$$q'' = \Big(\frac{2}{p} - 1\Big)\varepsilon_h''. \tag{5.3.23}$$

To achieve Fano-like region for cylindrical inclusion numerical result has been carried out for the imaginary part of the polarization for absorbing host medium. The plots in Fig. 5.4 and Fig. 5.5, particularly shows Fano-like resonance for cylindrical inclusions. However, the plots in Fig. 5.4 reveals that for the values of $p = 0.4$ and $p = 0.45$, and $\varepsilon_h'' = -0.569417$ the first asymmetric Fano-like peak which is less pronounced and narrow has been observed.

The plot in Fig. 5.3 also reveals the existence of Fano-like effect in terms of real value of refractive index for non absorbing host medium from the right and to the left of frequency $z = 0.3\omega_p$, showing dual Fano-like resonance observed, the case that is discussed in Ref. [45].

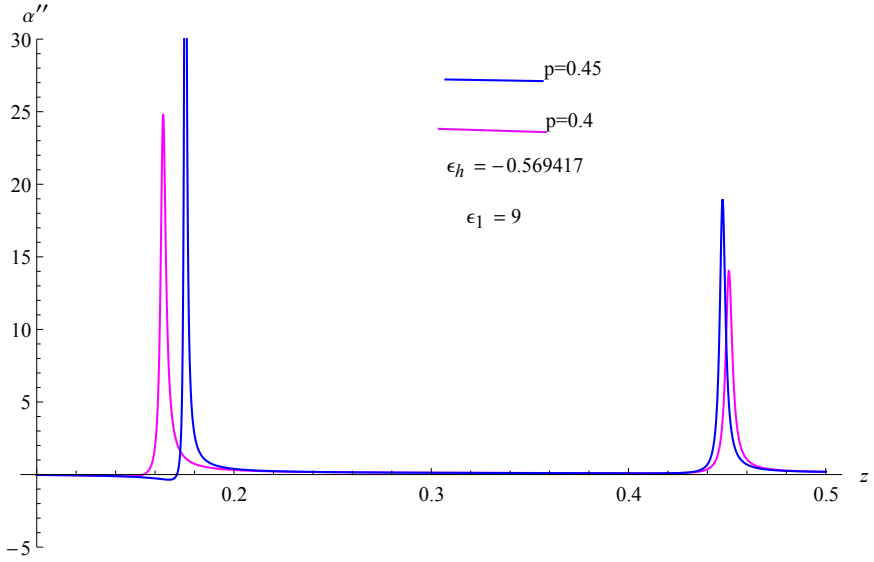


**Figure 5.4:** The imaginary part of polarization for given frequency shows Fano-like resonance upon introduction of negative value of $\varepsilon_h'' = -0.56947$ for $p = 0.4$ and $p = 0.45$ assuming $\varepsilon_1 = 9$.

### 5.3.3 Scattering Cross-Section for Polarizability of Spherical Inclusion

The expression for the total scattering cross-section is given by [2] as:

$$\sigma = \frac{1}{6\pi}\frac{\omega^4}{c^4}|\alpha(\omega)|^2, \tag{5.3.24}$$

where $\alpha(\omega) = \alpha'(\omega) + i\alpha''(\omega)$ given by Eq. 5.3.16. Therefore,

$$\sigma \sim KZ^4|\alpha'(\omega) + i\alpha''(\omega)|^2,$$

where $K$ is normalization constant. The frequency dependence of the scattering cross-section predicted by this equation is illustrated by Fig. 5.6. This result is a consequence of our assumption that it is only the core which is dispersive; the scattering particle is small compared to an optical wavelength and hence that the scattering is due solely to electric dipole and not to higher-order multipole processes. Following an expression for the total scattering cross-section as [122]:

$$\sigma = KZ^4|\alpha'(\omega) + i\alpha''(\omega)|^2,$$

where the dimensionless frequency $z$ and the electron collision frequency $\gamma$ are measured in the units of the metal plasma frequency $\omega_p$. We take into account

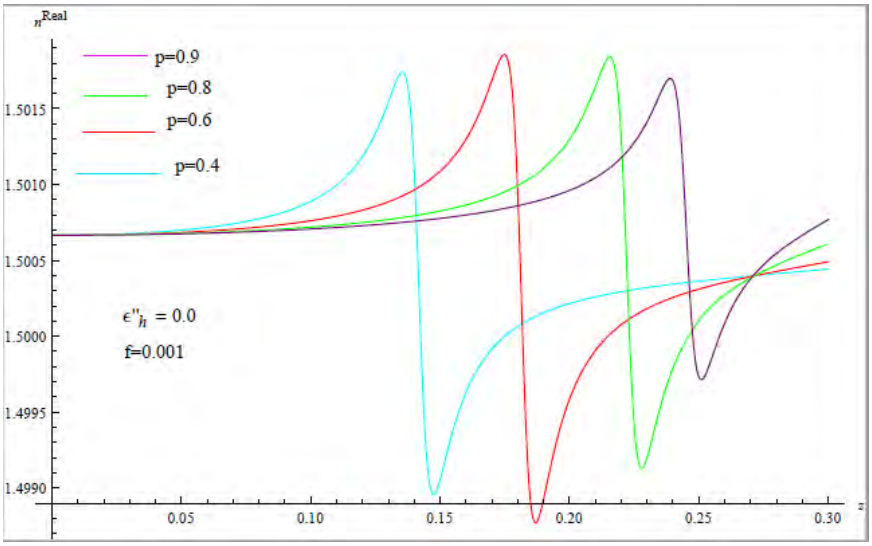


**Figure 5.5:** Real part of refractive index versus frequency for different values of $p$ considering non-absorbing host medium $\varepsilon_h'' = 0.0$ at fixed $f = 0.001$ and $\varepsilon_1 = 9$ exhibits Fano-like effect for frequency ($z$) range of 0.05 to 0.28.

the dispersion of the dielectric core and write it as:

$$\varepsilon_1 = C\Big[1 + \frac{\alpha^2}{z_g^2 - z^2}\Big], \tag{5.3.25}$$

where $C$ is an arbitrary constant. Here, $\alpha = \omega_{dp}/\omega_p$, $z_g = \omega_g/\omega_p$ with $\omega_{dp} = \sqrt{4\pi ne^2/m^*}$ is the plasma frequency of semiconductor, $m^*$ is the electron effective mass, $\omega_g$ is its gap frequency. The scattering cross-section versus frequency where the plot is employed for different values of $p$ upon introducing Eq. 5.3.25 in the expression of $\sigma$ above the appearance of Fano-like resonance is realized (see Fig. 5.6 in our model, where $\gamma_1$ is the width of the line corresponding to the eigen frequency $\omega_0$. It is important that this condition $\gamma_1 << \gamma << 1$ and $\alpha \approx \gamma_1$ must be satisfied. It means that Eq. 5.3.25 basically depends on the frequency $z$ in a very narrow frequency range $z = z_0 + \Delta z$, $\Delta z \approx \gamma_1$. In the frequency band $z_0 < z < z_0 + \Delta$, we have

$$\varepsilon_1 = \varepsilon(1 + \beta), \tag{5.3.26}$$

where $\beta$ is some constant that will be specified in the model for numerical analysis. Taking into account that only the core is dispersive ($\varepsilon_1 = \varepsilon_1(\omega)$) in our spherical

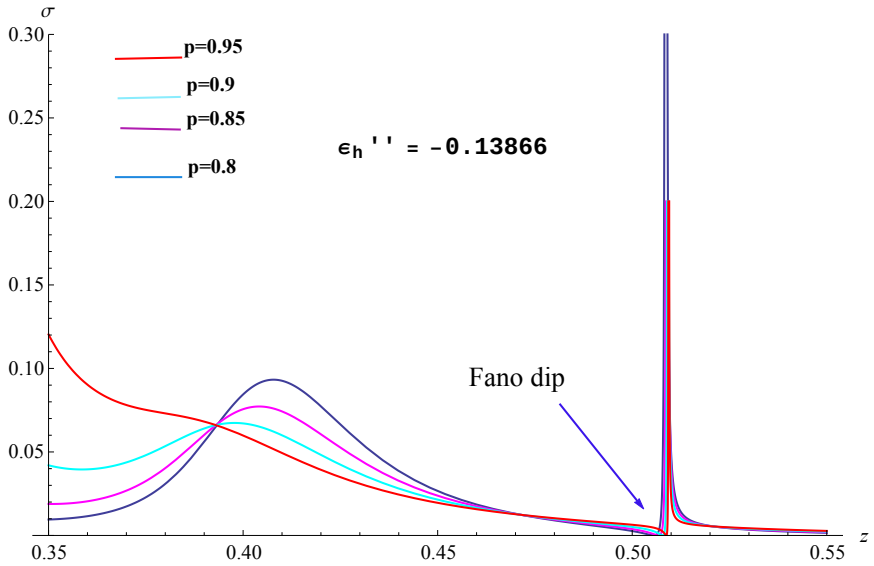


**Figure 5.6:** Scattering cross-section versus frequency for different volume fraction $p$ and keeping the value of $\varepsilon_h'' = -0.13866$ upon introducing frequency dependent dielectric function of the core $\varepsilon_1$ in $Eq.5.3.25$ one can easily tune and shift Fano regions from first resonance to the second resonance as shown on the plot where in this case $z = 0.51\omega_p$ we observe clear conventional Fano resonance in the composite.

geometry, and assuming that the media are weakly absorbing ($\varepsilon_h'' \ll \varepsilon_h'$), we obtain

$$|D_n(\omega)|^2 \approx \left[\frac{\varepsilon_1(\omega) - \varepsilon_1}{\varepsilon_1(\omega) - C\varepsilon_1}\right]^2, \tag{5.3.27}$$

where $C$ is the constant value of resonant frequency measured in $\omega_p$. In this situation $|D_n|^2$ as a function of $\varepsilon_1(\omega)$ is a Fano-like resonance characterized by the following (normalized) line shape [46, 116]:

$$G_n(\alpha'') = \frac{1}{1+K^2}\frac{(\alpha''+K)^2}{\alpha''^2+1}, \tag{5.3.28}$$

where $K(\varepsilon_1(\omega))$ is the asymmetry parameter. Analytical analysis of $\alpha'(z)$ and $\alpha''(z)$ can be done in the model of a very weak damping of plasma vibrations in the metal part of the inclusion when $\gamma$ is practically negligible while keeping the inequality $\gamma_1 << \gamma$. In this case $\varepsilon_2'' \sim \gamma$ is very small. For simplicity, we only considered the case $\varepsilon_h'' < 0$.

## 5.4 Summary and Conclusions

Metallic nanoshell will exhibit two resonant peaks in scattering spectrum when illuminated by an incident plane wave, due to the hybridization of the cavity and sphere modes of the nanoshell which are related to the surface plasmon resonances at the inner and outer interfaces. The plasmon modes of a metallic nanoshell, composed of a dielectric core embedded in active host medium, can be considered as arising from the interaction between the dipolar mode of the metallic sphere (S) and the dipolar mode of the dielectric core (C). The hybridization of the sphere mode and cavity plasmons created two new plasmon modes, that is, the higher energy mode and the lower mode, corresponding to the antisymmetric and symmetric interactions between the (S) and (C) modes, respectively. The interference between these two mode is the main reason for the appearance of Fano-like effect in our model. For composite metal-dielectric core-shell, in the Rayleigh limit, it was demonstrated that the origin of Fano-like resonance is due to interference of two dipole modes within the metal/dielectric core-shell composites, the spherical metal shell mode which is the low-energy mode giving rise to a continuous background and from the dielectric core the high-energy mode offers the discrete one. Therefore, the superposition between these two modes gives rise to Fano-like effect in the composite. We can clearly see that the resonant frequencies are related with the plasma vibrations of the metal part of the inclusion and the two interfaces, i.e., dielectric core-metal and metal-host matrix exhibit Fano-like resonance if the negative value of active host matrices ($\varepsilon_h'' < 0$) is introduced in composites with tuned inclusion. To find the value of $\alpha''$, we have used long wave approximation and effective medium theory approach. Before we used the approach we have checked the validity by taking the highest frequency associated with our problem which is approximately equal to $0.45\omega_p$ that gives $\lambda \simeq 287\ nm$. It means that the composites with inclusions of a typical size $20 - 30\ nm$ can be described within the frames of the long wave approximation.

However, these Fano-like resonances are expected to exist either in homogeneous spherical core-shells with large dielectric permittivity, beyond Rayleigh approximation or in particles with spatial dispersion. In the former literatures, Arruda et al. also reported such resonances may occur due to self interference of two dipole modes [113]. Finally, in this Chapter interference of local electric field mode and dipolar resonances within the composites were discussed which manifest itself in the Raman scattering of the composite of these inclusions.

# Chapter 6

# Effects of Precursor and Doping Concentration on Growth Mechanism and Ferromagnetic Properties of ZnO Nanostructures

## 6.1 Introduction

To realize any type of device technology, it is important to have control over the concentration of intentionally introduced impurities, called dopants, which are responsible for the electrical properties of ZnO [127, 128]. The dopants determine whether the current is carried by electrons or holes. The dopants are also called shallow level impurities because they introduce energy levels close to one of the allowed energy bands in the material and are easily ionized as a result. There may also be unintentional impurities introduced during the growth of ZnO that have a deleterious effect on the properties of the material. These are called deep level defects or impurities and may be either elemental impurities arising from contamination of the growth environment or structural defects in the ZnO crystal lattice. These structural defects can be vacancies in the crystal structure or interstitials, i.e., atoms sitting in the open regions around lattice sites [129, 130]. In both cases, they may introduce energy levels deep within the forbidden band gap of ZnO and act as traps for carriers in the material. These uncontrolled defects make it very difficult to obtain reproducible device performance and reliability.

Doped ZnO nanocrystals, which can be easily processed at temperatures much lower than those for bulk ZnO crystals, are of particular interest because of their potential for use in light-emitting devices [131].

Doping semiconductor with foreign elements to manipulate their electrical and magnetic properties is an important aspect for the realization of various types of advanced nanodevices [132]. The group III elements (Al, Ga and In) are expected to form shallow donors in single crystals of ZnO by replacing Zn atoms [133]. Al is among the dopants that can be used to enhance phonon scattering, improve the electrical conductivity and can replace traditional tin-doped indium oxide (ITO) transparent conducting oxide (TCO) films, which are essential components for a large variety of optoelectronic devices, acting as transparent electrical contacts or electrodes [134, 135]. Al-doped ZnO based heterojunctions were successfully assembled into various kinds of optoelectronic devices, and also be applied as attachments of gold nanoparticles in nonlinear optical nanocomposite materials [136, 137]. After the theoretical prediction of room temperature ferromagnetism (RTFM) in Mn-doped ZnO by Dietl et al. [138], ZnO doped with magnetic transition metal (TM) ions was intensively studied due to its potential applications in future spintronic devices, magneto-optics and magnetoelectronics. Sergei et al. [139] reported the identification of Li and Na as interstitial shallow donors in ZnO nanocrystals, however, the device application is not practical because of the challenge in controlling the concentration of donor impurities. Reviews by Klingshirn et al., [17, 18] on ZnO proposed the substitution of $Zn^{2+}$ ions by $Al^{3+}$ ions that may induce more point defects for the different ionic radii of $Al^{3+}$ and $Zn^{2+}$ ions [140, 141]. Indeed, the assertion was proved by Gao et al. [142] on their ferromagnetic study of ZnO nanoparticles doped with nonmagnetic element, Al. If this is the case, according to the $d^0$ ferromagnetism it is expected that the room temperature ferromagnetism (RTFM) can be achieved in Al-doped ZnO without Al metal clusters or the interfaces of Zn and Al. Recent studies also suggests the induced RTFM in the Al/ZnO film is due to the interaction of metal clusters and

the ZnO matrix [143, 144]. Based on the above observation, we investigate on room temperature ferromagnetism in Al doped ZnO and undoped ZnO produced by sol-gel technique.

ZnO nanostructures has been shown to produce a rich family of different nanostructures; as a wurtzite structure having a total of 13 different facet growth directions together with a pair of polar surfaces (0001) [130]. These diverse group of nanostructures includes: nanorods, nanobelts, nanocombs, nanosprings, nanorings, nanobows, nanojunction arrays, and nanopropeller arrays, which are formed largely due to the highly ionic character of the polar surfaces [131]. Therefore, compared with bulk materials, low-dimensional ZnO nanostructures such as nanorods, nanoflowers and their core-shell structures exhibit novel properties because of their larger surface areas and possible quantum confinement effects [132, 133]. ZnO nanostructures, especially nanorods or nanowires, possess a relatively large surface area to volume ratio, enabling them to release stress and strain due to lattice mismatch with other materials.

Successful synthesis of ZnO nanostructures with different morphologies can be realized by involving the right precursor and reaction temperature. Recently, investigations on alternative doping and precursor schemes in the synthesis and modification of nanosized ZnO have attracted tremendous attentions because of various technological applications. Various synthesis methods have been developed, including sol-gel, spray pyrolysis, thermal decomposition of organic precursor, precipitation and chemical bath deposition (CBD) are mentioned [134]. Among these techniques, CBD is appealing because of many advantages over other techniques. It is a low temperature phenomena to produce small sized crystal which gives better homogeneity [135]. Moreover, it is efficient for compositional modification and minimum variables to control the growth of sample with excellent control on stoichiometry and morphologies [136]. In light of the above observations, we studied the changes in the optical and structural properties of ZnO nanostructures with different geometries which are produced by varying the precursor concentration

and reaction temperature.

## 6.2 Sample Preparation

### 6.2.1 Preparation of Al doped ZnO nanoparticles samples $((Zn)_{1-x}OAl_x)$

ZnO and aluminum doped ZnO (AZO) nanoparticles were synthesized by sol-gel method. The precursor used to prepare the sol are Zinc acetate dehydrate $[Zn(CH_3COO)_2{,}2H_2O]$ which was dissolved into 2-methoxyethanol $[C_3H_8O_2]$ as a solvent and monoethanolamine are used to stabilize the solution. To prepare $((Zn)_{1-x}OAl_x)$, AZO aluminum nitrate nonahydrate $Al(NO_3)_3, 9H_2O$ were used as aluminium source for the prepared samples. In the process of preparation $(Zn)_{1-x}OAl_x$, the doped concentration of $Al/Zn = 0.05,\ 0.10,\ 0.15,\ 0.20$ represented by x, were prepared. The structure of the samples were characterized by x-ray diffractometry (XRD) with $Cu\ K_\alpha$ ($\lambda = 0.15418\ nm$) radiation and the surface morphology of the nanoparticles are investigated by scanning electronic microscopy (SEM) ZU SSX-550. The ferromagnetic properties was studied using JEOL $x$-band electron paramagnetic resonance (EPR) which operates at frequency of 9.4 $GHz$. The samples were set to be placed at the center of the cavity where magnetic field of the microwave is maximum. However, the power was kept at 5 $mW$ and the $H_{DC}$ field was slowly varied in between 0 and 500 $mT$. Finally, the response was measured as a derivative of microwave absorption signal. Perkin Elmer UV/Vis and (PL) (He-Cd) laser system 5.0 with an excitation 248.6 $nm$ are used to measure the luminescence of the samples.

### 6.2.2 Preparation of ZnO nanoparticles samples with various precursor

A simple versatile CBD has been adopted to prepare ZnO nanostructures with different morphology. All the chemicals used were purchased from Sigma Aldrich and used without further purification. Three types of nanostructure are prepared: (a) ZnO nanorod, (b) ZnO/ZnS core-shell nanorod, and (c) flower-like ZnO nanostructure. The detail of the preparations are given below:

- ZnO nanorods:

  In this typical method, ZnO nanorods were grown on pre-treated Si substrate from an aqueous solution of zinc nitrate hexahydrate $Zn(NO_3)_26H_2O$ (54 $mM$ in 25 $ml$ de-ionized water (DW)) was mixed with 15 $mg$ of polyvinylpyrrolidone (PVP) in 20 $ml$ DW under vigorous stirring to produce the nanorods.

- ZnO/ZnS core-shell nanorods:

  The as-grown ZnO nanorods was immersed in a 150 $mmol$ $Na_2S$ solution for 80 $min$ at 65 °C followed by sulphidation. Upon removing the sample it was rinsed in Milli-Q water and dried in $N_2$ to form ZnO/ZnS core-shell structures.

- Flower-like ZnO nanostructures:

  In a typical flower-like ZnO structures, 0.44 $M$ of zinc acetate ($Zn(CH_3COO)_2$,$2H_2O$), 0.16 $M$ Thiourea $(NH_2)_2CS$ and 20 $mL$ Ammonia (25% $NH_3$) were dissolved in 80 $mL$ of deionized water to prepare ZnO precursor. The solution was stirred to form homogeneous mixture and keep uniform distribution of reagents. Finally the obtained ZnO nanoparticles were washed with acetone, ethanol and deionized water to be dried at ambient conditions for 48 $hrs$. The samples was characterized using similar techniques mentioned above except EPR.

## 6.3 Ferromagnetism in Al Doped ZnO

The phases and structures of the samples are identified using XRD spectra. Fig. 6.1 A, shows XRD patterns of undoped ZnO and Al doped ZnO which were indexed as a polycrystalline hexagonal wurtzite structure of ZnO. The crystallographic direction are labeled according to (JCPDS card No. $36-1451$). The spectra shows there are no formation of secondary phase observed in the samples. The strong peak along (101) from the spectra suggest the preferred crystal orientation. The calculated lattice parameter and the shift in peak towards the larger angle are displayed in Table 6.1. Fig. 6.1 B shows $\omega_{scan}$ (rocking curve) for the samples indicating the shifts towards the higher angles which is indicative of a compressive stress incorporated in the ZnO lattice. It was noted that from rocking curve (Fig. 6.1, B) the shift towards the lower angle indicates the $Al^{+3}$ ions incorporated in $Zn^{+2}$ sites successfully.

**Table 6.1:** The calculated lattice constants of Al doped and undoped ZnO, $(Zn)_{1-x}OAl_x$

| Al concen.(x) | $2\theta$ | Lattice constants, a ($\mathring{A}$) | Lattice constants, c ($\mathring{A}$) |
|---|---|---|---|
| 0.00 | 31.76 | 3.248 | 5.299 |
| 0.05 | 31.54 | 3.247 | 5.302 |
| 0.10 | 31.47 | 3.245 | 5.305 |
| 0.15 | 31.41 | 3.243 | 5.307 |
| 0.20 | 31.37 | 3.241 | 5.307 |

Figure 6.2 shows the morphology and the elemental composition of the samples taken using scanning electron microscopy (SEM). Fig. $2A$, $2B$ and $2C$ shows the SEM micrograph of undoped ZnO and Al doped ZnO, $(Zn)_{1-x}OAl_x$ at $x = 0.0$, $x = 0.15$, and $x = 0.20$, respectively. The micrographs are indicative of the formation of the samples without secondary phase and elements. The EDX pattern shown in Fig. $2D$, $2E$ and $2F$ indicates the elemental composition of samples with $x = 0.0$, $x = 0.15$, and $x = 0.20$, respectively. The spectra confirms the

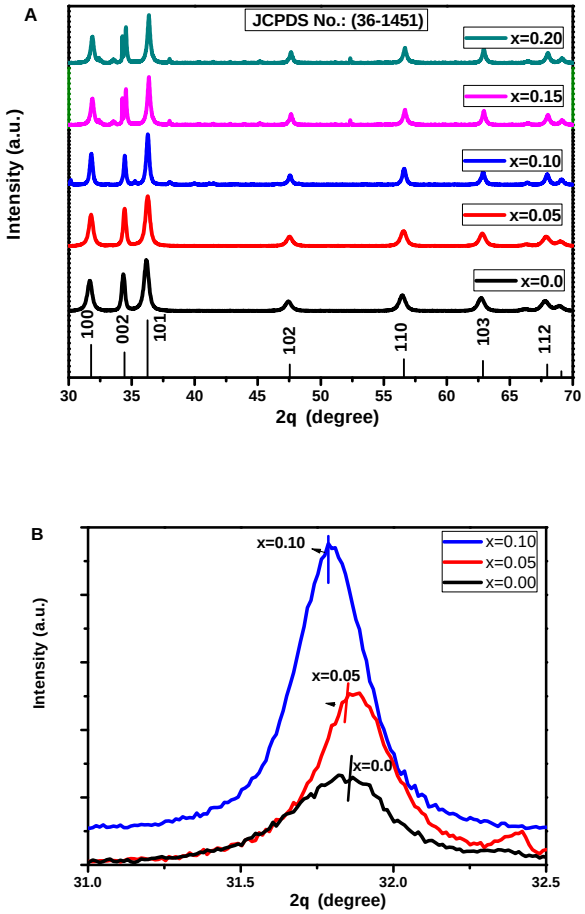


**Figure 6.1:** (A). XRD patterns of undoped and Al doped ZnO nanocrystalline powders for different Al concentrations (B). $\omega_{scan}$ (rocking curve) for samples having Al concentration at $x = 0.0$, $x = 0.15$, and $x = 0.20$.

.

assertion with existence of all expected elemental compositions (Zn, O and Al) in the samples.

To characterize the paramagnetic defects or centers in the samples EPR spectroscopy were used. The techniques are effective in identifying unpaired electrons so that surface defects, radicals, cations or clusters are easily detected through EPR signals. Therefore, EPR measurements (see Fig. 6.3) are taken with microwaves having power with 5 $mW$ by fixing the frequency at 9.4 $GHz$. By increasing DC field from 1 $mT$ to 6 $mT$ at 100 $kHz$, the difference in energy between the two states is widened until it matches the energy of the microwaves. Fig. 6.3 A shows the microwave response as a function of magnetic flux density

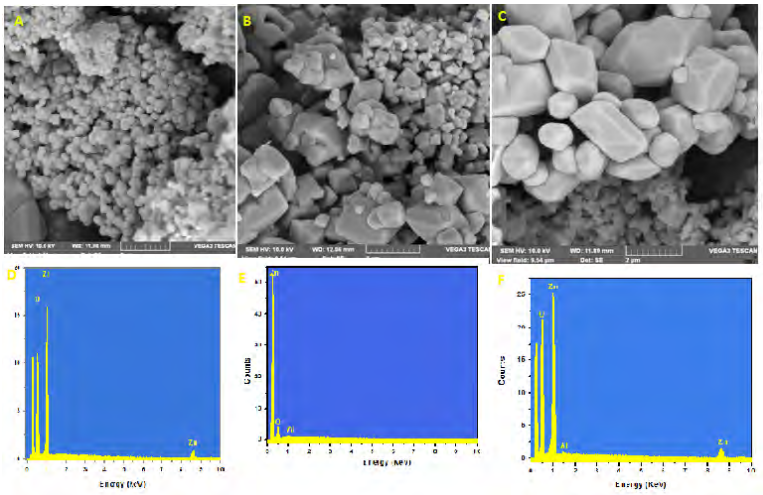

**Figure 6.2:** SEM micrograph and EDX spectrum of ZnO nanoparticles at: (A) undoped ZnO, (B) $x = 0.15$, (C) $x = 0.20$, and $D$, $E$ and $F$ are the corresponding EDX spectra.

(DC field) for undoped ZnO and Al doped ZnO samples at room temperature. As indicated there are two absorption peaks at 150 and 300 $mT$ which are ascribed to paramagnetism and ferromagnetism resonant field, respectively. The former will be due to magnetic clusters situated near the surface which are emanated from electron spin trapped in the defects. As indicated in Fig. 6.3 B around 300 $mT$ and 350 $mT$ field there are hyperfine line coupling which become broader with increase in Al concentration due to exchange interaction of dopant ions. Although the exact mechanism of intrinsic FM in undoped oxides is still under debate, defects have greatly been suggested to play an important role in the FM origin in the undoped ZnO system [145, 146]. However, in the present work we suggest that the origin of FM in undoped ZnO comes from the intrinsic exchange interaction of magnetic moments in the sample. The PL analysis, which predicts the existence of single oxygen vacancies carrying a net magnetic moment underscore the assertion to the origin of FM are defect induced. However, the role of defects in mediating the FM in undoped ZnO still needs further theoretical and experimental studies.

Fig. 6.4 shows room temperature PL spectrum with various Al concentration. Here, in the spectra, three emission peaks at around 3.3, 2.4 $eV$ and 2.6 $eV$ are observed. The emission at around 3.3 $eV$ is assigned to near band edge emission, whereas the peak at around 2.6 $eV$ were ascribed to electronic transitions from Zn

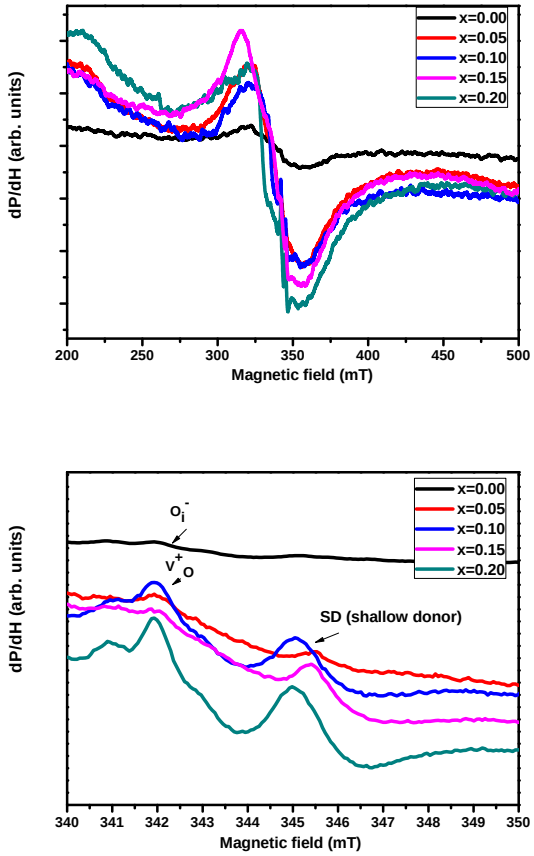


**Figure 6.3:** A. EPR measurements for the undoped and Al doped ZnO. B. Shows the enlarged EPR measurements

interstitial levels ($Z_{ni}$) to valence band and singly ionized oxygen vacancies ($V_o^+$) as similar conclusions are drawn by Gao et al. [147]. The emission at 2.4 $eV$ is likely due to the doubly ionized oxygen vacancy ($V_o^{++}$). Moreover, in the present work these defects are suggested as the origin of room temperature FM observed in undoped ZnO structures.

Fig. 6.5 shows the optical band gap ($E_g$) of the Al doped and undoped ZnO which are estimated using Tauc's equation as $(\alpha h\nu)^2$ versus $(h\nu)$. The estimated band gap energies are reduced from 3.30 $eV$ down to 3.20 $eV$ because of the the energy shift [148, 149].

Figure 6.6 shows the FTIR spectra of the undoped ZnO and Al doped ZnO structure recorded in the region of $500 - 2500$ $cm^{-1}$. All the absorption bands

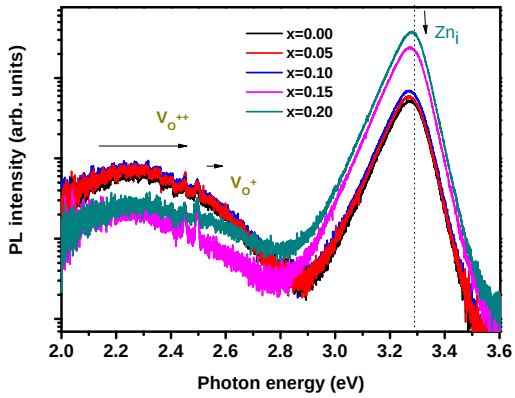


**Figure 6.4:** PL emission of ZnO nanoparticles synthesized for various concentration of Al.

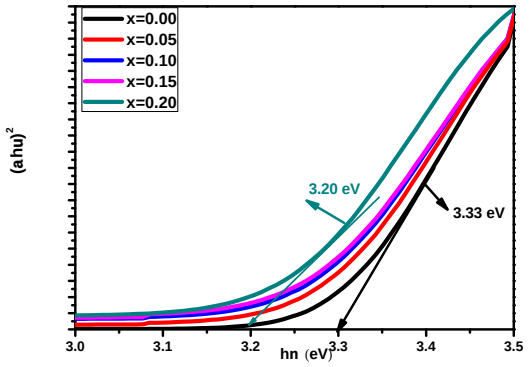


**Figure 6.5:** The optical absorption energy band gap estimated using Tauc's plot relation for ZnO nanoparticles synthesized at different annealing temperatures.

.

of ZnO samples which were recorded in the transmittance mode were clearly observed. The modes located at around 1580 $cm^{-1}$ and 1410 $cm^{-1}$ corresponds to the vibrations of a carboxyl group (CO) coordinated to the metal ions [150, 151]. From the spectra it is clearly seen that Zn-O-Zn modes were observed at 512 $cm^{-1}$ [152]. The bands observed around 850 $cm^{-1}$ and 1000 $cm^{-1}$ corresponds to C-OH, however; the spectra at 1078 $cm^{-1}$ are indicative of the formation of AZO in the prepared samples [153, 154].

Raman scattering measurements were recorded to study the vibration modes in the un-doped ZnO and Al doped ZnO structures, as shown in Fig. 6.7. The

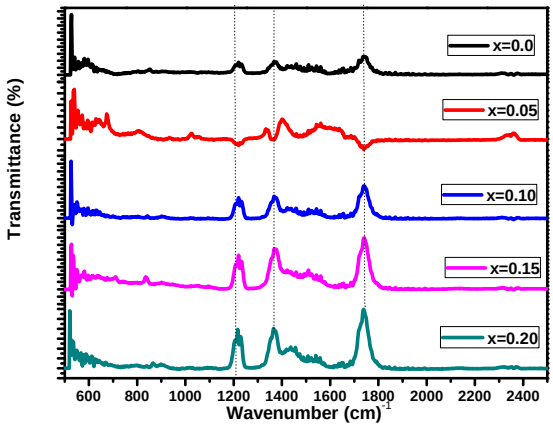


**Figure 6.6:** FTIR spectra of undoped ZnO and Al doped ZnO in the transmittance mode.

.

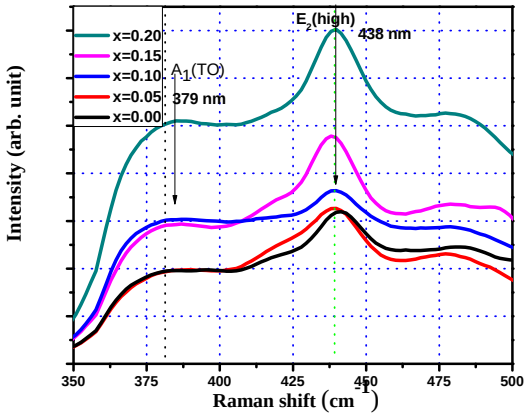


**Figure 6.7:** Raman spectra of undoped ZnO and Al doped Zinc Oxide for different concentration.

.

Raman spectrum of the undoped ZnO nanostructures shows the conventional vibration modes of $A_1(TO)$ and $E_{2H}$ at around, 380 $cm^{-1}$ and 438 $cm^{-1}$, which have correlation with oxygen vacancies [155]. The increase in intensity of Raman peaks with increase in Al concentration might be related with band shift and distortion of FM ordering, the shift towards the lower vibrational mode indicates the possibility of oxygen related scattering.

## 6.4 The Effect of Precursors on ZnO Nanostructures: Structural and Optical studies

Figure 6.8 shows XRD patterns of the ZnO nanostructure with flower-like samples. It shows series of broad diffraction peaks at $(2\theta) = 31.63^0$, $34.50^0$, $36.25^0$, $47.50^0$, $56.60^0$, $62.80^0$, and $67.92^0$; which could correspondingly be indexed reflected planes of (100), (002), (101), (102), (110), (103) and (112). The standard JCPDS card No. $36 - 1451$ indicates hexagonal wurtzite structure of ZnO. It can be clearly seen that by increasing the growth temperature from 300 °C to 500 °C the flower-like ZnO peaks became more prominent and prevailed. In addition, there is no formation of secondary phase in the prepared samples. Therefore, the broadening of the XRD peaks (i.e., Scherer broadening) gave a clear indication of the formation of nanosized ZnO, and the wurtzite phase was not disturbed by the addition of precursor and the environment.

The crystallite size of the ZnO with different structures were estimated using the Debye-Scherer equation given by [137]:

$$D = \frac{0.9\lambda}{\beta \cos\theta}, \tag{6.4.1}$$

where $D$ is the crystallite size, $\lambda$ is the wavelength of radiation used, $\theta$ is the Bragg diffraction angle and $\beta$ is the full width at half maximum. The calculated crystallite sizes are displayed in Table. 6.2. For the ZnO/ZnS core-shell structure of the nanorods it is observed that the peaks were broader and shifted to the lower angle and this might be because of the charge separation mechanism of type-II band alignment that holes transfer from the core to shell, which would quench the UV emission.

The preferred crystallite orientation was obtained using the relation [96]:

$$I = \frac{I_{002}}{I_{101}} \sim 0.53,$$

which is higher than the corresponding standard value of 0.44 of the bulk hexagonal wurtzite ZnO [132] suggesting the prepared flower-like ZnO samples preferred

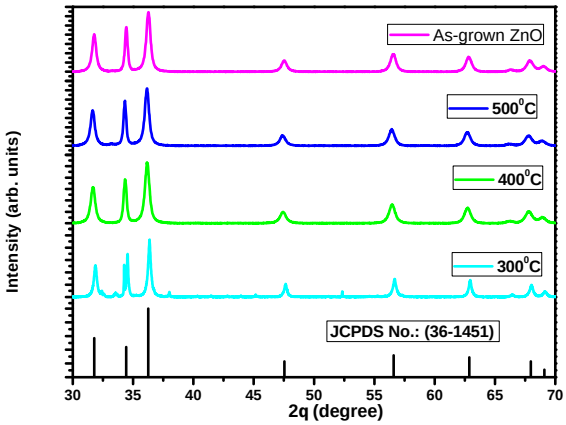


**Figure 6.8:** XRD pattern of flower-like ZnO nanoparticles synthesized at various temperatures for 3 $hr$.

.

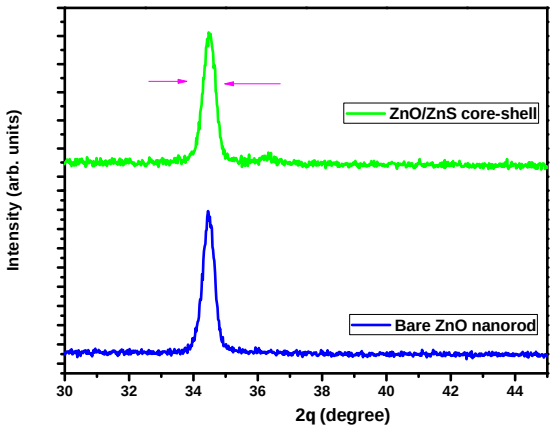


**Figure 6.9:** XRD patterns of the ZnO/ZnS core-shell nanorods and bare ZnO nanorods.

.

the (002) orientation. Fig. 6.9 shows the XRD spectra of the as-grown ZnO nanorods and ZnO/ZnS core-shell structure indicating the intensity increases and the prominent peak (002) shifts to the lower angles. The diffraction peaks are indexed to those of hexagonal wurtzite ZnO and no diffraction peaks of any other phases were observed. The narrow (002) diffraction peaks indicate that the materials are of good crystallinity. Fig. 6.10 shows the SEM images of nanorods and flower-like ZnO samples. Fig. 6.10 (A, B and C ) depicts the SEM profiles of the

**Table 6.2:** Nanorods Morphological analysis and crystallite size.

| Temp. °C | Average diameter ($nm$) | Time ($hr$) | Average length ($\mu m$) |
|---|---|---|---|
| 200 | 50 | 3 | 1.2 |
| 300 | 80 | 3 | 0.8 |
| 400 | 100 | 3 | 0.5 |

nanorods prepared at 300 °C, 400 °C and 500 °C, respectively. It is clearly observed that as the annealing temperature increases, the diameter and the length of the rods increases. Moreover the randomly oriented nanorods become more visible having defined regular morphology. Fig. 6.10 D, E and F shows the flower-like ZnO morphologies prepared at annealing temperature of 300 °C, 400 °C and 500 °C, respectively. It was found that the shape of the flower changes with temperature keeping the precursor concentration the same for the three samples as similar studies are done in ref. [138]. Fig. 6.10 G and H indicates the EDX pattern of all the expected elemental compositions (Zn, O and S) in the core-shell nanorods (Fig. 6.10 G) and flower-like ZnO structure (Fig. 6.10 H) produced at 400 $^0C$.

Figure 6.11 depicts the absorbance spectra of the flower-like ZnO structure at different annealing temperature. An absorption edge around 360 $nm$ exhibits red shift with significant enhancement of light absorption. The observed peaks conform to the well-known intrinsic band gap absorption of the ZnO where the rise in absorption might be because of the decrease in crystallinity [140].

Figure 6.12 shows the optical band gap ($E_g$) of the flower-like ZnO which are estimated using Tauc's equation as $(\alpha h\nu)^2$ versus $(h\nu)$. The estimated band gap energies are 3.24, 3.25, 3.26 and 3.27 $eV$ for samples prepared at the temperature of 25 °C, 300 °C, 400 °C and 500 °C, respectively. The increase in band gap might be because of oscillator strength or quantum size effect [139].

Figure 6.13 shows room temperature PL spectrum of the nanorods, indicating emissions at two distinct energy windows. The two emissions observed at around 3.26 $eV$ and 2.28 $eV$ are associated with free-exciton recombination and zinc

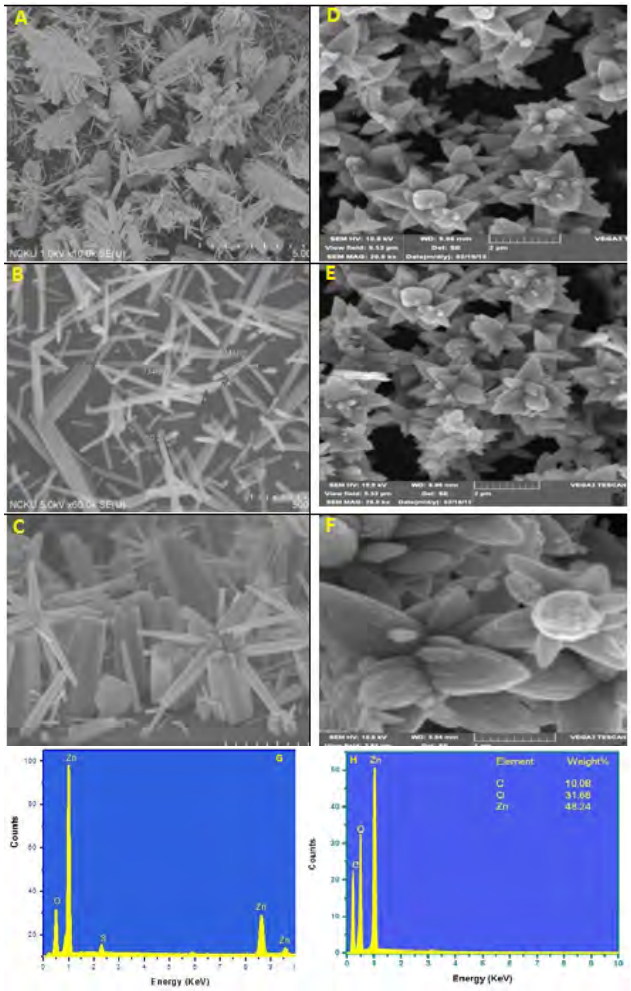


**Figure 6.10:** SEM micrograph and EDX spectrum of ZnO: (I). A. ZnO nanorods at 300 °C, B. ZnO nanorods produced at 400 °C, C. ZnO/ZnS core-shell nanorods produced at 500 °C, (II). D, E and F are flower-like ZnO structures synthesized at 300 °C, 400 °C and 500 °C, respectively. (III). G shows EDX spectra for the core-shell structure and H depicts flower-like ZnO for the sample synthesized at 400 °C.

.

vacancy ($V_{Zn}$) respectively [102]. The broad peak emission observed at around 2.96 $eV$ for the case of ZnO/ZnS core-shell might be either as a result of transitions involving sulphur vacancy states or surface band-gap narrowing as suggested by Lahiri and Batzill [141]. In addition Denzler et. al [147] suggested the possibility of sulphur being incorporated interstitially during sulphidation, which could be applicable to our observations.

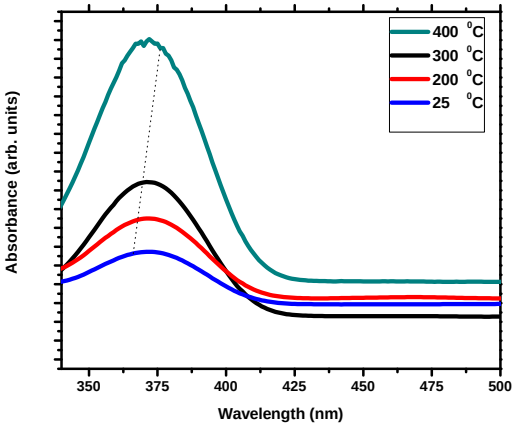


**Figure 6.11:** UV-Vis absorbance spectra of flower-like ZnO synthesized at different annealing temperatures.

.

Figure 6.14 shows the PL spectrum of the flower-like structures at various annealing temperatures. There are four emission bands, including band edge emission observed at around 398.3 $nm$ (3.11 $eV$), 402.8 $nm$ (3.07 $eV$), 406.9 $nm$ (3.04 $eV$) and 409.6 $nm$ (3.02 $eV$) for ZnO samples prepared at a temperature of 500 °C, 400 °C, 300 °C and 25 °C, respectively. Band edge emission centered at around 398.3 nm should be attributed to the recombination of excitons and $V_{Zn}$ [102, 148]. However the origin of violet emissions centered at 3.07 $eV$ (402.79 $nm$), 406.9 $nm$ (3.04 $eV$) and 409.6 $nm$ (3.02 $eV$) are ascribed to an electron transition from a shallow donor level of neutral $Zn_i$ to the top level of the valence band on theoretical grounds [149]. The broad deep level emission that started from UV to the visible region $360 - 450$ $nm$ with the maximum peak at 425 $nm$ for the sample prepared at 300 °C was observed. The quenching mechanism of luminescent observed are more profound on PL spectra, this might be because higher temperature promotes greater kinetics causing better interaction [150].

Temperature dependent PL was conducted for ZnO nanorods sample prepared at 400 °C as depicted in Fig. 6.15. The temperature dependent PL spectrum of synthesized ZnO nanoparticles prepared at 400 °C were studied at a temperature of 300 $K$, 273 $K$, 223 $K$, 173 $K$, 123 $K$ and 84 $K$. The transition line at 3.30 $eV$ were attributed to native defect ($V_{zn}$) and the near-band-edge (NBE) emission

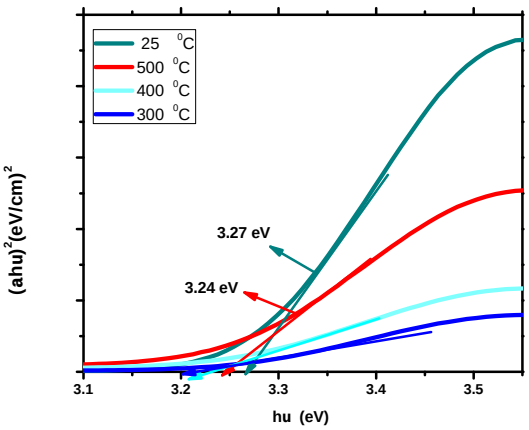


**Figure 6.12:** The optical band gap estimated using Tauc's plot relation for flower-like ZnO structure synthesized at various annealing temperatures.

.

peak at 3.37 $eV$ were assigned to DAP. The peak labeled in 3.37 eV gains strength with decreasing temperature, in contrast, peak labeled 3.30 $eV$ is strong at low temperature because carriers trapped at these sites do not have enough thermal energy to escape the trap level. With increasing temperature, the DAP emission energy was shifted to the low energy side because carriers on donor-acceptor-pairs (DAP) with small donor-acceptor distance are released into the band [149]. The transition at 3.33 $eV$ is ascribed to excitons bound to structural defects. This transition line at 3.33 $eV$ was previously observed in various ZnO samples and tentatively ascribed to donor bound excitons (DX), acceptor bound excitons, transitions of intrinsic point defects and excitons bound to extended structural defect, respectively. The most detail study of this transition was reported by Yalishev et al.[151] and Wagner et al. [110]. In their work, the 3.33 $eV$ emission line was attributed to recombination of excitons bound to extended structural donor defect complexes which disappear at temperature of 10 $K$.

Figure 6.16 shows the FTIR spectra of the bare ZnO nanorods and ZnO/ZnS core-shell structure recorded in the region of $500 - 3500\ cm^{-1}$. A series of absorption peaks from 1000 to 3500 $cm^{-1}$ are observed corresponding to the vibration

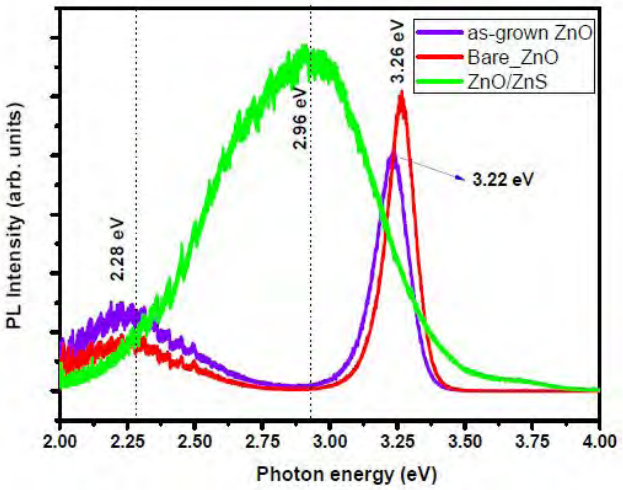


**Figure 6.13:** PL spectra of ZnO/ZnS core-shell nanorods and bare ZnO nanorods.

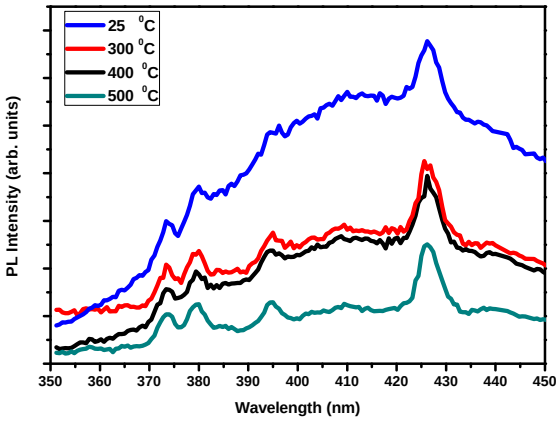


**Figure 6.14:** PL emission of flower-like ZnO structure synthesized at various temperatures.

modes of impurities. The vibration mode around the region $1600-1500\ cm^{-1}$ corresponds to the vibrations of a carboxyl group (CO). From the spectra it is clearly seen that Zn-O-Zn modes were observed at 512 $cm^{-1}$ [100]. The absorption bands observed around 850 $cm^{-1}$ and 1000 $cm^{-1}$ corresponds to C-OH. The characteristic wurtzite lattice vibrations (Zn-O) and (Zn-S) correspond to the broadband in the range $400-600\ cm^{-1}$ [131]. Thus, the analysis indicates that ZnO/ZnS core-shell plays a major role in tuning the broadness of emission of the ZnO.

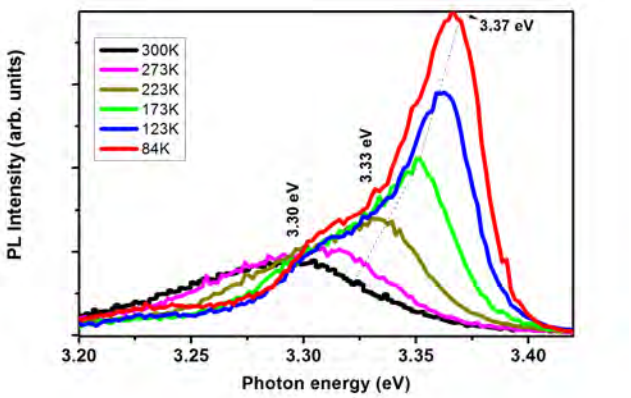


**Figure 6.15:** Temperature dependent PL emission of ZnO nanorods prepared at 400 °C.

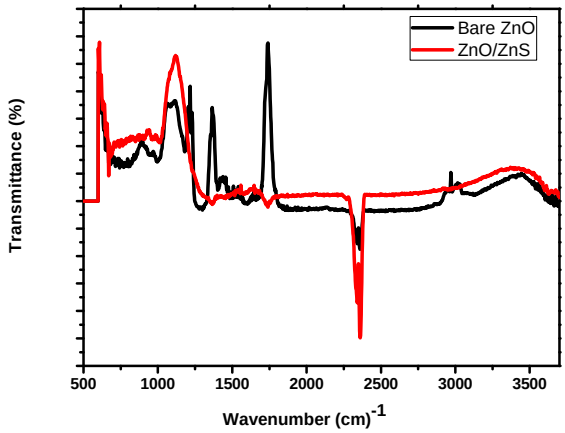


**Figure 6.16:** FTIR spectra of ZnO/ZnS core-shell nanorods and bare ZnO nanorods.

.

## 6.5 Summary and Conclusions

We have successfully synthesized undoped ZnO and Al doped ZnO nanostructures by facile sol-gel approach. The effects of Al concentration on the magnetic, optical and structural morphology are investigated. EPR clearly indicates the hyperfine splitting in the samples, and in addition it confirms defects, in particular, zinc interstitials and singly ionized oxygen vacancies, are the origin of ferromagnetism in undoped ZnO nanostructure. However, in the Al-doped ZnO nanostructure, the suppression of FM ordering might be ascribed to the formation of Al short range

orders. The structural analysis performed by SEM images, XRD, and EDX spectra reveals that the prepared samples possess hexagonal wurzite polycrystalline structures. In addition, the PL spectra indicates the presence of defects in the synthesized samples and also successfully incorporation of $Al^{3+}$ into the ZnO lattice. The analysis of Raman spectra also confirms this assertions.

Moreover, the flower-like, nanorods and core-shell ZnO nanostructures are synthesized by CBD method are studied. The effects of annealing temperatures on optical and structural morphology are investigated. XRD and FTIR spectroscopy confirms the formation of wurtzite structure of ZnO nanoparticles. The SEM images and EDX spectra reveals the presence of flower-like, nanorods and core-shell structure of ZnO without any impurities. The average diameter of the nanorods increases and the length of the nanorods decreases with increasing reaction temperature. The PL spectra shows strong UV emission of the flower-like ZnO samples. The temperature dependent PL spectra of ZnO nanorods prepared at 400 °C shows three transition lines at 3.30 $eV$, 3.37 $eV$ and 3.33 $eV$ which are ascribed to zinc vacancy ($V_{zn}$), donor-acceptor pairs and excitons bound to structural defect, respectively.

# Chapter 7

# Conclusions and future work

## 7.1 Conclusions

The work presented in the thesis provides a deeper understanding of the interactions between plane electromagnetic wave with spherical or cylindrical core-shell nano-inclusions which are embedded in active host medium. We started our study assuming the size of the particles within the frame work of long wave approximation. The theoretical models, such as effective medium approximation were used to calculate the electric potentials inside and outside the composites. The analytical calculations related with effective polarizablity and scattering cross section of the system under study were systematically related to demonstrate the appearance of Fano-like resonances in the composites. It is believed that such calculations will help for tuning Fano resonances related spectral regions in composites using variables such as volume fraction, filling fraction, electric permittivity of the host medium and the geometrical shape of the inclusions. Though, Fano resonance is a widely studied phenomenon in various systems, the present study gave intuitive explanation for the existence of Fano resonances in composites having metal/dielectric core-shell structure. Moreover, such studies are very important not only in the elucidation of the fundamental physics but also for possible devices application such as narrow band optical filters, polarization selectors, modulators, switches and highly sensitive biochemical sensors.

However; there have been a few attempts to produce Fano resonance in classical optics, but structures to achieve this are necessarily complicated because it is difficult to achieve narrow surface plasmon resonance peaks in classical optics.

In weakly dissipating plasmonic materials, Fano resonance can arise due to the interference between a broad Mie resonance and a narrow surface plasmon resonance. Localized plasmons excited by the incident light are equivalent to the quasi-discrete levels in the Fano approach, while the radiative decay of the excitation plays the same role as tunneling from quasi-discrete levels. Thus, the local maximum and minimum in scattering spectra correspond to constructive and destructive interference between different eigen modes, respectively.

There are various suggestions for the origin of Fano resonances in such a system including plasmon hybridization. We also suggest the origin of Fano resonances in the composite as the interaction between the dipolar mode of the metallic shell (S) and the dipolar mode of the dielectric core (C). The assertion can be supported by previous models stating the hybridization of the sphere mode and cavity plasmons created two new plasmon modes, that is, the higher energy mode and the lower mode, corresponding to the antisymmetric and symmetric interactions between the (S) and (C) modes, respectively. The interference between these two mode are likely the main reason for the appearance Fano-like resonance in the composites.

The experimental part of the study includes growth mechanism of ZnO nanostructures. The interest in ZnO is growing rapidily because of its technological relevances. Nowadays, the interest in ZnO by the scientific community is fuelled by availability of high quality substrates, reports of p-type conductivity, and ferromagnetic behavior when doped with transitions metals. Indeed, the studies include both theoretical predictions and perhaps experimental confirmations. However, cheap crystal growth of ZnO, which can be simple and produced at low temperature needs further studies. In our study we synthesized ZnO nanostructures with different geometries using simple and effective method. Moreover, the effect of dopant on the ferromagnetic properties of ZnO nanostructures are studied using different techniques. The salient results are summarized as follows:

1. The role of precursor and reaction temperature on the growth of ZnO nanostructures with various geometry has been developed. ZnO has been shown

to be able to produce a rich family of different nanostructures, as a wurtzite structure, which are formed largely due to the highly ionic character of the polar surfaces. Flower-like, spherical ZnO particles are synthesized by chemical bath deposition, the structural and optical properties are studied. ZnO nanorods were grown on pre-coated Si substrate from an aqueous solution of zinc nitrate hexahydrate followed by sulphidation process to form ZnO/ZnS core-shell.

2. ZnO doped with magnetic transition metal (TM) ions was intensively studied due to its potential applications in future spintronic devices, magneto-optics and magnetoelectronics. In this thesis, the origin of ferromagnetism in undoped ZnO and non-magnetic metal (Al), doped with ZnO at various concentration has been investigated. The effect of Al concentration on ferromagnetic ordering are also studied using electron paramagnetic resonance. Although the exact mechanism of intrinsic FM in undoped oxides is still under debate, defects have greatly been suggested to play an important role in the FM origin in the undoped ZnO system. As it supported by our PL and EPR analysis section such vacancies may very likely carry a net moment for the origin of ferromagnetism in our observation.

## 7.2 Future work

Fano interference is a universal phenomenon in the sense that the manifestation of configuration interference does not depend on matter. Fano interference may potentially be used for the design of new types of quantum electronic or spintronic devices such as Fano-transistors, spin transistors and Fano-filters for polarized electrons. In addition, Fano phenomena can also be used for lasing without population inversion. From the educational point of view, there are wave phenomena such as Youngs interference in optics or AB interference in quantum mechanics which are milestones in modern physics. Nowadays, the findings related with Fano resonace in plasmonics, photonics and metamaterials attracts the overwhelming

interest of scientific community because of novel technological advances. Therefore, in the future the author needs to expand the study further for other system not included in the thesis. On the other hand, a number of questions regarding ZnO nanomaterials from the point of view of its synthesis and its characterization have been addressed in this thesis. However, several topics remain unsolved and further investigations need to be completed in order to produce device quality material. Therefore, general future work should include:

- The origin of Fano resonance in multiple core-shell layers of structures of various materials.
- The correlation between photoluminescence and Fano resonance in ZnO related materials and it's application in heterostructures
- Growth control of the thickness, quality and optimization of the ZnO/ZnS core-shell nanorods.
- Detailed understanding of the underlying mechanism to control the observed morphology and the electrical properties of ZnO.
- The study related with p-type conduction and ferromagnetic behavior of ZnO with other non-magnetic metals not covered under the present study has been among the list of future works.

# List of Publications and Conferences

- ***Leta Jule**, Vadim Malnev, Belayneh Mesfin, Teshome Senbeta, Francis Dejene, and Kittessa Roro, Fano-like resonance and scattering in dielectric(core)metal(shell) composites embedded in active host matrices, Phys. Status Solidi B 252, No. 12, 2707-2713 (2015).*

- ***Leta Jule**, Belayineh Mesfin, Teshome Senbeta, Sisay Shewamare, The role of precursor and reaction temperature to produce ZnO nanostructures with different geometry, International Journal of Photonics and Optical Technology Vol. 2, Iss. 4, pp: 38-42, Dec. (2016).*

- ***Leta Tesfaye**, Belayneh Mesfin, Teshome Senbeta, On the origin of ferromagnetism in Al doped ZnO, under review, March, (2017).*

- Rapid synthesis of blue emitting ZnO nanoparticles for fluorescent applications, *Presented at Cairo national research center, 2016, Cairo, Egypt*

- Fano-like scattering in nanocomposite, SAIP (2015), South Africa. *Presentation at South African institute of Physics, (2015).*

# Bibliography


[1] Kerker Milton, Academic Press, New York, (1969).

[2] Mie Gustav, Ann Phys **25**, 377-445 (1908).

[3] C. F. Bohren and D. R. Huffman, John Wiley and Sons, New York, (1983).

[4] Xiaofeng Fan, Weitao Zheng and David J Singh, Light: Science and Applications **3**, e179 (2014).

[5] Shaunak Mukherjee, Heidar Sobhani, J. Britt Lassiter, Rizia Bardhan, Peter Nordlander ,and Naomi J. Halas, Nano Lett. **10**, 2694-2701 (2010).

[6] H. C. Van de Hulst, John Wiley and Sons, New York (1957).

[7] Michael I. Tribelsky, Sergej Flach, Andrey E. Miroshnichenko, Andrey V. Gorbach, and Yuri S. Kivshar, Phys. rev. lett. **100 (4)**, 043903, (2008).

[8] Mikhail V. Rybin, Kirill B. Samusev, Ivan S. Sinev, George Semouchkin, Elena Semouchkina, Yuri S. Kivshar, and Mikhail F. Limonov, Opt. Express **21**, 30107-30112, (2013).

[9] M. Born, and E.Wolf, $7^{th}$ Ed., Cambridge: Cambridge University Press (1999).

[10] G. Grzela, R. Paniagua-Domnguez, T. Barten, Y. Fontana, J. A. Snchez-Gil, and J. G. Rivas, Nano Lett. **12**, 5481 (2012).

[11] A. Tuniz, B. T. Kuhlmey, P. Y. Chen, and S. C. Fleming, Opt. Express **18**, 18095 (2010).

[12] Pavan Kumar Kasanaboina, Estiak Ahmad, Jia Li, C. Lewis Reynolds Jr., Yang Liu, Shanthi Iyer, Appl. Phys. Lett. **107**, 103111 (2015)

[13] A. Mirzaei, I. V. Shadrivov, A. E. Miroshnichenko, and Y. S. Kivshar, Opt. Express **21**, 10454 (2013).

[14] Ron Gurwitz, Rotem Cohen, Ilan Shalisha, J. Appl. Phys. **115**, 033701 (2014)

[15] X. Wang, K. L. Pey, C. H. Yip, E. A. Fitzgerald, D. A. Antoniadis, J. Appl. Phys. **108**, 124303 (2010).

[16] Ozgur, Alivov, Ya.I.; Liu, C.; Teke, A.; Reshchikov, M.A.; Dogan, S.; Avrutin, A.; Cho, SJ.; Morko, H., J. Appl. Phys. **98**, 041301103 (2005).

[17] Klingshirn, C, physica status solidi (b) **244**, 3027-3073 (2007).

[18] Klingshirn, C.; Mollwo, Zeitschrift fur Physik A , **254**, 437446 (1972).

[19] Zhong Lin Wang, J. Phys.: Condens. Matter **16**, R829-R858 (2004).

[20] Junxi Zhang and Lide Zhang, Advances in Optics and Photonics Vol. **4**, Issue 2, pp. 157-321 (2012).

[21] Clemens Burda, Xiaobo Chen, Radha Narayanan, Mostafa A El-Sayed, Chemical reviews **105**, 1025-1102 (2005).

[22] Reed, Jennifer, Electronic Theses and Dissertations. Paper 2781 (2013).

[23] Yong S Joe, Arkady M Satanin, and Chang Sub Kim, Phys. Scr. **74**, 259266 (2006).

[24] M. Tyboroski, N. Anderson, and R. Camley, J. Appl. Phys., vol. **106**, 124314, (2014).

[25] D. R. Smith, S. Schultz, P. Marko, and C. M. Soukoulis, Phy. Rev. B, vol. **65**, 016608, (2004).

[26] Graham Hugh Cross, Opt. Express **38**, 3057-3060 (2013).

[27] Leta Jule, Vadim Malnev, Belayneh Mesfin, Teshome Senbeta, Francis Dejene, and Kittessa Roro, Phys. Status Solidi B **252**, 2707 (2015).

[28] Ohad Levy, David Stroud, Phys. Rev. B **56**, 8035-8046 (1997).

[29] J. C. M. Garnett, Philos. Trans. R. Soc. London, Ser. B **203**, 385 (1904).

[30] R. Landauer, edited by J. C. Garland and D. B. Tanner, AIP Conf. Proc. No. 40 AIP, New York, (1978).

[31] Mohsen Rahmani, Boris Lukyanchuk, and Minghui Hong, Laser Photonics Rev. **7(3)**, 329-349 (2013).

[32] Hao Zhang, Heyuan Zhu and Min Xu, Opt. Express **19**, 2928-2940 (2011).

[33] Tao Geng, Songlin Zhuang, Jie Gao, and Xiaodong Yang, Phys. Rev. B **91**, 245128 (2015).

[34] Maxim A.Yurkin, Alfons G. Hoekstra, J. Quant. Spect. and Rad. Trans. **112**, 2234-2247 (2011).

[35] Purcell EM, Pennypacker CR., Astrophys J **186**, 705-14 (1973).

[36] Draine BT, Flatau PJ., J Opt Soc Am A **11**, 1491-9 (1994).

[37] G.B. Arfken, H.J. Weber, Elsevir Science, (2001).

[38] J. D. Jackson, John Wiley, New York, (1999).

[39] Zaiping Zeng, Christos S. Garoufalis, Andreas F. Terzis, and Sotirios Baskoutas, J. Appl. Phys. **114**, 023510 (2013).

[40] Abdelilah Mejdoubi and Christian Brosseau, J. Appl. Phys. 103, 084115 (2008).

[41] A. Mejdoubi, M. Malki, M. Essone Mezeme, Z. Sekkat, M. Bousmina, and C. Brosseau, J. Appl. Phys. **110**, 103105 (2011).

[42] A. Vial T. Laroche M. Dridi L. Le Cunff, Appl Phys A **103**, 849-853 (2011).

[43] K. S. Yee, IEEE Trans. Antennas Propag. **14**, 302-307 (1966).

[44] A. Taflove and S. C. Hagness, Artech House, (2005).

[45] A. E. Miroshnichenko, S. Flach, and Y. S. Kivshar, Rev. Mod. Phys. **82**, 2257 (2010).

[46] B. Lukyanchuk, N. I. Zheludev, S. A. Maier, N. J. Halas, P. Nordlander, H. Giessen, and C. T. Chong, Nat. Mater. 9, 707715 (2010).

[47] Phys. Status Solidi B **247**, No. 9, 2244-2251 (2010).

[48] T. J. Arruda and A. S. Martinez, J. Opt. Soc. Am. A **27**, 992 (2010); 27, 1679 (2010).

[49] Shalaev, V.M., vol. **82**. Springer, Berlin (2002).

[50] M. I. Tribelsky, A. E. Miroshnichenko, and Y. S. Kivshar, Europhys. Lett. **97**, 44005 (2012).

[51] Adnan Daud Khan, Sultan Daud Khan, Rehan Ullah Khan, Naveed Ahmad, Amjad Ali, Akhtar Khalil, Farman Ali Khan, Plasmonics **9(5)**, 1091-1102 (2014).

[52] M. I. Tribelsky and B. S. Lukyanchuk, Phys. Rev. Lett. **97**, 263902 (2006).

[53] Boyd R.W., AP, NY (1992).

[54] Shi X., Dai Z. and Zeng Z., Phys. Rev. B **76**, 235412 (2007).

[55] Kreibig, U., Vollmer, M., vol. **25**. Springer, Berlin (1995).

[56] Adnan Daud Khan, Muhammad Amin, Muhammad Yasir Iqbal, Amjad Ali, Rehan Ullah Khan, Sultan Daud Khan, Plasmonics **10**:963-970 (2015).

[57] T. Pan, J. P. Huang, Z. Y. Li, Physica B **301**, 190-195 (2001).

[58] K.M.Lenng, Phys.Rev.A**33** (1986) 2461.

[59] D. S. bergman, O. Levy, D. Stroud, Phys.Rev.B **49** 129,(1994).

[60] Lie. Gao, X. P. Yu, Physics letters A **335**, 457-463 (2005).

[61] V.N. Mal'nev , Sisay Shewamare, Physica B **426**, 5257 (2013).

[62] W. Liu, A. E. Miroshnichenko, D. N. Neshev, and Y. S. Kivshar, Phys. Rev. B **86**, 081407 (2012).

[63] A.E.Neeves and M.H.Birnboim, J.Opt.Soc.Am.B, **6**, 787 (1989).

[64] Fang, Z., Nano letters, **11(10)**, p. 2694-2701 (2011).

[65] P. Reimers and W. Ruppel, Phys. Status Solidi **29**, K31 (1968).

[66] Zhang Y., Optics letters, **37(23)**: p. 4919-4921 (2012).

[67] Zhang S., Nano letters, **11(4)**: p. 1657-1663 (2011).

[68] Chen, H., Acs Nano, **5(8)**: p. 6754-6763 (2011).

[69] A. E. Miroshnichenko, Phys. Rev. A **81**, 053818 (2010).

[70] Lopez-Tejeira, F., R. Paniagua-Dominguez, and J.A. Sanchez-Gil, Acs Nano, **6(10)**: p. 8989-8996 (2012).

[71] Mukherjee, S., Nano letters, **10(7)**: p. 2694-2701 (2010).

[72] Liu, N., Nature materials, **8(9)**: p. 758-762 (2009).

[73] C. L. Garrido Alzar, M. A. G. Martinez, and P. Nussenzveig, Am. J. Phys. **70**, 37 (2002).

[74] U. Fano, Phys. Rev. **124**,1866 (1961).

[75] P. W. Anderson, Phys. Rev. **124**, 41 (1961).

[76] E. Prodan, C. Radloff, N. J. Halas, and P. Nordlander, Science **302(5644)**, 419-422 (2003).

[77] Jingjing Zhang, and Anatoly Zayats, Opt. Express **21(7)**, 8426-8436 (2013).

[78] D.C. Look, Mater. Sci. Eng., vol. **B80**, pp. 383-387, (2001).

[79] K. Talla, J.K.Dangbegnon, M.C.Wagener , J.Weber , J.R.Botha, J. Cryst. Growth, vol. **315**, pp. 297-300, (2011).

[80] L. Duan, X. Zhao, Y. Wang, H. Shen, W. Geng, F. Zhang, J. Alloys. Comp. **645**, 529-534 (2015).

[81] A. Kaushal, D. Pathak, R. Bedi, D. Kaur, Thin Solid Films **518 (5)**, 1394-1398 (2009).

[82] Willander, M.; Nur, O.; Zhao, Q.X.; Yang, L.L.; Lorenz, M.; Cao, B.Q.; Zuniga Perez, J.; Czekalla, C.; Zimmermann, G.; Grundmann, M.; Bakin, A.; Behrends, A.; Al-Suleiman, M.; Al Shaer, A.; Che Mofor, A., Postels, B. Waag, A.; Boukos, N.; Travlos, A.; Kwack, H.S.; Guinard, J.; Le Si Dang, D., Nanotechnology **20**, 332001 (2009).

[83] Ahn, H.A.; Kim, Y.Y.; Kim, D.C.; Mohanta, S.K.; Cho, H.K., J. Appl. Phys. **105**, 013502 (2009).

[84] Liu, W.; Gu, L.S.; Ye, D.L.; Zhu, S.M.; Liu, S.M.; Zhou, X.; Zhang, R.; Shi, Y.; Hang, Y.; Zhang, C.L., Appl. Phys Lett. **88**, 092101 (2006).

[85] Gao, P.X.; Ding, Y.; Wang, Z.L., Nano. Lett. **3**, 1315-1320 (2003).

[86] L. Vayssieres, K. Keis, S. E. Lindquist, A. Hagfeldt, J. Phys. Chem. B, vol. **105**, p. 3350, (2001).

[87] L. Vayssieres, Adv. Mater., vol. **15**, p. 464, (2003).

[88] Lander, J.J., J. Phys. Chem. **15**, 324-334 (1960).

[89] Zwingel, D., J. Lumin. **5**, 385-405 (1972).

[90] Look, D.C.; Claflin, B., Phys. Stat. Sol. B **241**, 624-630 (2004).

[91] Schirmer, O.F.; Zwingel, D. Sol. Stat. Commun. **8**, 1559-1563 (1970).

[92] Liu, M.; Kitai, A.H.; Mascher, P., J. Lumin. **54**, 35-42 (1992).

[93] Wu, X.L.; Siu, G.G.; Fu, C.L.; Ong, H.C., Appl. Phys. Lett. **78**, 2285-2287 (2001).

[94] M. Ohyama, H. Kozuka, T. Yoko, Thin Solid Films, vol. **306**, pp. 78- 85, (1997).

[95] B. Weintraub, Z. Zhou, Y. Li, Y. Deng, Nanoscale, vol. **2**, pp. 1573-1587 (2010).

[96] D.B Mitzi, Canada: WILEY, (2009).

[97] Gomi, M.; Oohira, N.; Ozaki, K.; Koyano, M., Jpn. J. Appl. Phys. **42**, 481-485 (2003).

[98] Djurisic, A.B.; Leung, Y.H.; Tam, K.H.; Hsu, Y.F.; Ding, L.; Ge, W.K.; Zhong, C.; Wong, K.S.; Chan, W.K.; Tam, H.L.; Cheah, K.W.; Kwok, W.M.; Phillips, D.L., Nanotechnology, **18**, 095702 (2007).

[99] L.L Yang, Linkoping University, PhD thesis Dissertation No.1327, (2010).

[100] B. K. Meyer, H. Alves, D. M. Hofmann, W. Kriegseis, D. Forster, F. Bertram, J. Christen, A. Hoffmann, M. Straburg, M. A. Dworzak, U. Haboeck, A. V. Rodina, phys. stat. sol. (b), vol. **241**, pp. 231-260, (2004).

[101] M. Mehrabian, R. Azimirad, K. Mirabbaszadeh, H. Afarideh, M. Davoudian, Physica E, vol. **43**, pp. 1141-1145, (2011).

[102] B. K. Meyer, J. Sann, D. M. Hofmann, C. Neumann, A. Zeuner, Semicond. Sci. Technol. , vol. **20**, pp. S62-S66, 2005.

[103] H. Morkoc, U. Ozgur, Zinc Oxide: ISBN: 978-3-527-40813-9, Ed. Germany: WILEY-VCH, (2009).

[104] Jayeeta Lahiri and Matthias Batzill, J. Phys. Chem. C **112**, 4304-4307 (2008).

[105] A. L. Patterson, J. Phys. Rev. B, vol. **56**, p. 978, (1939).

[106] J.S. Lee, K. Park, M. I. Kang, I. W. Park, S. W. Kim, W. K. Chom, H. S. Han, S. Kim, J. Cryst. Growth, vol. **254**, p. 423, (2003).

[107] A. R. Barron, Physical Methods in Chemistry and Nano Science, Rice University, CONNEXIONS, p. 295 (2012).

[108] F. Pan, C. Song, X.J. Liu, Y.C. Yang, F. Zeng, Materials Science and Engineering **R 62**, 135 (2008).

[109] L. S. Vlasenko, Appl Magn Reson **39**:103111 (2010).

[110] M. R. Wagner, G. Callsen, J. S. Reparaz, J. H. Schulze, R. Kirste, M. Cobet, I. A. Ostapenko, S. Rodt, C. Nenstiel, M. Kaiser, A. Hoffmann, A. V. Rodina, M. R. Phillips, S. Lautenschlager, S. Eisermann, and B. K. Meyer, Phys. Rev. B **84**, 035313 (2011).

[111] Chen J, Wang P, Chen C, Lu Y, Ming H, Zhan Q, Opt Express **19(7)**, 5970-5978 (2011).

[112] T. J. Arruda, F. A. Pinheiro, and A. S. Martinez, J. Opt. **14**, 065101 (2012).

[113] T. J. Arruda, F. A. Pinheiro, and A. S. Martinez, J. Opt. Soc. Am. A **30**, 1205 (2013); **31**, 1811 (2014); **32**, 943 (2015).

[114] A. Alu and N. Engheta, Phys. Rev. E **72**, 016623 (2005).

[115] A. Alu and N. Engheta, Phys. Rev. Lett. **100**, 113901 (2008).

[116] T. J. Arruda, A. S. Martinez, and F. A. Pinheiro, Phys. Rev. A **87**, 043841 (2013).

[117] Tiago J. Arruda, Alexandre S. Martinez, and Felipe A. Pinheiro, Phys. Rev. A **92**, 023835 (2015).

[118] S.A. Ramakrishna, J.B. Pendry, Phys. Rev. B **67**, 201101 (2003).

[119] A. K. Sarychev, G. Tartakovskii, Phys. Rev.B **75**, 085436 (2007).

[120] Clemens Burda, Xiaobo Chen, Radha Narayanan, and Mostafa A. El-Sayed, Chem. Rev., **105**, 1025-1102 (2005).

[121] L.D.Landau, E.M.Lifshits, L.P.Pitaevskii, Butter worth-Heinemann, Oxford, (1984).

[122] J.D. Jackson, John Wiley, New York, (1999).

[123] A.K. Sarychev, V.M. Shalaev, Physics Reports **335**, 275-371 (2000).

[124] V. Lozovski, S. Khihlovski, K. Grytsenko, V. Ksianzou, S. Schrader, and G. Strilchuk, Phys. Status Solidi B **247(9)**, 2244-2251 (2010).

[125] V. N. Malnev and S. Shewamare, Physica B **426**, 52-57 (2013).

[126] M. Pylak and R. Swirkowicz, Phys. Status Solidi B **247(1)**, 122-128 (2010).

[127] S. K. Kim, S. Y. Seong, C. R. Cho, Appl. Phys. Lett., vol. **82**, p. 562, (2003).

[128] C. Woll, Progress in Surface Science 82, vol. **82**, pp. 55-120, (2007).

[129] X. D. Gao, X. M. Li, W. D. Yu, J. Phys. Chem. B, vol. **109**, p. 1155, (2005).

[130] Z.L. Wang, Chinese Science Bulletin, vol. **54**, pp. 4021-4034, (2009).

[131] Agnieszka Koodziejczak-Radzimska and Teofil Jesionowski, Materials **7**, 2833-2881 (2014).

[132] Magnus Willander, Omer Nur, Jamil Rana Sadaf, Muhammad Israr Qadir, Saima Zaman, Ahmed Zainelabdin, Nargis Bano and Ijaz Hussain, Materials **3**, 2643-2667 (2010).

[133] Ching-Ting Lee, Materials **3**, 2218-2259 (2010).

[134] F. Bai, Pi. He, Z. Jia, X. Huang, Y. He, Materials Letters, vol. **59**, pp. 1687-1690 (2005).

[135] J. Lee, A.J. Easteal, U. Pal, D. Bhattacharyy, Curr. Appl. Phys., vol. **9**, pp. 792-796, (2009).

[136] Q. Li, J. Bian, J. Sun, J. Wang Y. Luo, K. Sun and D. Yu, Appl. Surf. Sci., vol. **256**, pp. 1698-1702 (2010).

[137] A. L. Patterson, J. Phys. Rev. B, vol. **56**, p. 978, (1939).

[138] T. Dietl, H. Ohno, F. Matsukura, J. Cibert, D. Ferrand, Science **287 (5455)**, 1019-1022 (2000).

[139] S. B. Orlinskii, J. Schmidt, P. G. Baranov, V. Lorrmann, I. Riedel, D. Rauh, V. Dyakonov, Phys. Rev. B 77, 115334 (2008).

[140] X. Yu, X. Yu, J. Zhang, H. Pan, Materials Letters **161**, 624-627 (2015).

[141] J. Lahiri and M. Batzill, J. Phys. Chem. C , vol. **112**, no. 11, pp. 4304-4307, (2008).

[142] D. Gao, J. Zhang, G. Yang, J. Zhang, Z. Shi, J. Qi, Z. Zhang, D. Xue, J. Phys. Chem. C **114 (32)**, 13477-13481 (2010).

[143] Z. Zhang, U. Schwingenschlogl, I. S. Roqan, RSC Adv. **4**, 50759-50764 (2014).

[144] Yung Kuan Tseng, Guo Jhan Gao, Shih Chun Chien, Thin Solid Films **518**, 6259-6263 (2010).

[145] T. Moe Borseth, B. G. Svensson, A. Yu. Kuznetsov, P. Klason, Q. X. Zhao and M. Willander, Appl. Phys. Lett. **89**, 262112 (2006).

[146] Jun-Ho Kima, Yoon Jong Moon, Sun Kyung Kim, Young ZoYoo, Tae Yeon-Seong, Ceram.Int. **41**, 3064-3068 (2015).

[147] D. Denzler, M. Olschewski and K. Sattler, J. Appl. Phys., vol. **84**, no. 5, pp. 2841-2845, (1998).

[148] N. Bano, I. Hussain, O. Nur, M. Willander, P. Klason, A. Henry, Semicond. Sci. Technol., vol. **24**, p. 125015, (2009).

[149] G. Nam, Bull. Korean Chem. Soc., vol. **34**, no. 15, pp. 95-98, (2013).

[150] X. Wang, T. Yang, G. Du, H. Liang, Y. Chang, W. Liu, Y. Xu, J. Cryst. Grow., vol. **285**, pp. 521-526, (2005).

[151] V. S. Yalishev, Y. S. Kim, X. L. Deng, B. H. Park, Sh. U. Yuldashev, J. Appl. Phys., vol. **112**, p. 013528, (2012).

[152] L. T. Jule, F. B. Dejene, A. G. Ali, K. T. Roro, A. Hegazy, N. K. Allam, E. E. Shenawy, J. Alloys. Comp. **687**, 920-926 (2016).

[153] C. d. M. D. J. S. Pavel G. Baranov, Sergei B. Orlinskii, Appl. Magn. Reson. **39 (10)**, 151-183 (2010).

[154] A. P. Thurber, G. L. B. II, G. A. Alanko, J. J. Anghel, M. S. Jones, L. M. Johnson, J. Zhang, C. B. Hanna, D. A. Tenne, A. Punnoose, Journal of Applied Physics **109 (7)**, 07C305 (2011).

[155] H. Fukushima, T. Kozu, H. Shima, H. Funakubo, H. Uchida, T. Katoda, K. Nishida, in: Joint IEEE Int. Symp., pp. 28-31 (2015).